

# Nanostructured ZnO and metal chalcogenide films for solar photocatalysis

TAHA AHMED



ACTA UNIVERSITATIS  
UPSALIENSIS  
2023

ISSN 1651-6214  
ISBN 978-91-513-1961-2  
urn:nbn:se:uu:diva-515258



UPPSALA  
UNIVERSITET

Dissertation presented at Uppsala University to be publicly examined in Polhemsalen, Lägerhyddsvägen 1, Uppsala, Monday, 18 December 2023 at 13:15 for the degree of Doctor of Philosophy. The examination will be conducted in English. Faculty examiner: Professor Mats Johnsson (Stockholms universitet, Institutionen för material- och miljökemi).

#### **Abstract**

Ahmed, T. 2023. Nanostructured ZnO and metal chalcogenide films for solar photocatalysis. *Digital Comprehensive Summaries of Uppsala Dissertations from the Faculty of Science and Technology* 2337. 129 pp. Uppsala: Acta Universitatis Upsaliensis. ISBN 978-91-513-1961-2.

The increasing demand for clean energy and safe water resources has driven the development of efficient and sustainable technologies. Among these technologies, photocatalysis using semiconducting materials has emerged as a promising solution for both solar hydrogen generation and water purification. Low-dimensional ZnO, including nanorods, nanoparticles, and quantum confined particles (so called quantum dots), has demonstrated excellent photocatalytic properties due to their large surface area, high electron mobility, and tunable band gap.

The work in this thesis aims to investigate the potential of low-dimensional ZnO alone and in combination with CdS and Fe<sub>2</sub>O<sub>3</sub> for solar hydrogen generation and photocatalytic water purification. The thesis includes a comprehensive analysis of the synthesis, characterization, and optimization of low-dimensional ZnO-based photocatalyst systems for solar hydrogen generation and photocatalytic water purification. Additionally, the thesis will evaluate the performance of the ZnO-based photocatalysts under different experimental conditions, either as photoelectrodes or as distributed particle systems for water purification. The work includes detailed size control of ZnO by itself in dimensions below 10 nm using a hydrothermal method, to provide an increased total surface area and introduce quantum confinement effects that increase the band gap to enable degradation of chemical bonds in a model pollutant in a distributed system for water purification. The work also includes a relatively detailed study of the phonon–phonon and electron–phonon coupling as a function of dimension from 10 nm to 150 nm for ZnO using non-resonant and resonant Raman spectroscopy. Ultimately, the thesis aims to provide insight into the potential of low-dimensional ZnO alone and in combination with other inorganic materials for solar hydrogen generation and photocatalytic water purification and pave the way for the development of efficient and sustainable technologies for clean energy and safe water resources.

**Keywords:** photocatalysis, zinc oxide, quantum dots, nanorods, quantum confinement, low-dimensional, cathodic electrodeposition, Raman spectroscopy

*Taha Ahmed, Department of Chemistry - Ångström, Structural Chemistry, Box 538, Uppsala University, SE-751 21 Uppsala, Sweden.*

© Taha Ahmed 2023

ISSN 1651-6214

ISBN 978-91-513-1961-2


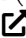
URN urn:nbn:se:uu:diva-515258 (<http://urn.kb.se/resolve?urn=urn:nbn:se:uu:diva-515258>)

*Till min mor och far*



# List of papers

This thesis is based on the following papers or manuscripts, which are referred to in the text by their Roman numerals.

- I Li, C.\*; **Ahmed, T.\***; Ma, M.; Edvinsson, T.; Zhu, J. A facile approach to ZnO/CdS nanoarrays and their photocatalytic and photoelectrochemical properties.  
*Applied Catalysis B: Environmental* 2013, 138–139, 175–183.  
DOI: 10.1016/j.apcatb.2013.02.042   
\* These authors shared first co-authorship.
- II **Ahmed, T.**; Fondell, M.; Younesi, R.; Donzel-Gargand O.; Boman, M.; Zhu, J. Preparation and characterisation of ZnO/Fe<sub>2</sub>O<sub>3</sub> core–shell nanorods.  
*In manuscript.*
- III **Ahmed, T.**; Edvinsson, T. Optical quantum confinement in ultrasmall ZnO and the effect of size on their photocatalytic activity.  
*J. Phys. Chem. C* 2020, 124 (11), 6395–6404. DOI: 10.1021/acs.jpcc.9b11229 
- IV **Ahmed, T.**; Thyrr, J.; Katea, S. N.; Westin, G.; Edvinsson, T. Phonon–phonon and electron–phonon coupling in nano-dimensional ZnO.  
*In manuscript.*

Reprints were made with permission from the publishers.



# Author's contributions


Author's contributions to the papers included in the thesis, here given based on the contributor roles taxonomy, CRediT.\*

**PAPER I** Supporting role in conceptualisation, data curation, formal analysis, and resources. Co-lead role in investigation, project administration, and visualisation. Supporting role in provision of study materials, reagents and instrumentation. Supporting role in writing the initial draft as well as in review and editing.

**PAPER II** Supporting role in conceptualisation and resources. Lead role in investigation, project administration, data curation, formal analysis, and visualisation. Supporting role in review and editing.

**PAPER III** Supporting role in conceptualisation. Lead role in investigation, project administration, data curation, formal analysis, visualisation and writing the initial draft. Supporting role in review and editing.

**PAPER IV** Lead role in investigation, project administration, data curation, formal analysis, visualisation, and writing the initial draft.

\*The CRediT taxonomy  describes 14 roles that represent the typical range of contributions to scientific outputs. It was originally developed [1] in 2014, was recently designated an ANSI standard Z39.104-2022, and has already been the subject of meta-studies [2, 3]. It is in use by more than 50 organisations collectively representing thousands of journals.





# List of other scholarly contributions

Other peer-reviewed publications or other scholarly contributions, including publicly shared scientific software or datasets. In the event they are referred to in the summary, they are shown as **CONTRIB. 4**.

- 1 Halvani Anaraki, E.; Kermanpur, A.; Mayer, M. T.; Steier, L.; **Ahmed, T.**; Turren-Cruz, S.-H.; Seo, J.; Luo, J.; Zakeeruddin, S. M.; Tress, W. R.; Edvinsson, T.; Grätzel, M.; Hagfeldt, A.; Correa-Baena, J.-P. Low-temperature Nb-doped SnO<sub>2</sub> electron-selective contact yields over 20 % efficiency in planar perovskite solar cells. *ACS Energy Lett.* 2018, 3 (4), 773–778. DOI: 10.1021/acsenergylett.8b00055 [↗](#)
- 2 El-Zohry, A. M.; Diez-Cabanes, V.; Pastore, M.; **Ahmed, T.**; Zietz, B. Highly emissive biological bilirubin molecules: shedding new light on the phototherapy scheme. *J. Phys. Chem. B* 2021, 125 (32), 9213–9222. DOI: 10.1021/acs.jpcc.1c05308 [↗](#)
- 3 **Ahmed, T.**; Edvinsson, T. Data and code to reproduce **PAPER III**, *Uppsala University* 2023. DOI: 10.57804/d33y-r007 [↗](#)
- 4 **Ahmed, T.** Band edge positions and band gaps for some semiconductors. R package, GitHub. DOI: 10.5281/zenodo.4099767 [↗](#)
- 5 **Ahmed, T.** Tauc fitting of band edges from UV-Vis spectra. R package, GitHub. DOI: 10.5281/zenodo.5814054 [↗](#)
- 6 **Ahmed, T.** Converting between common reference electrode scales. R package, GitHub. [github.com/solarchemist/refelectrodes](https://github.com/solarchemist/refelectrodes) [↗](#)
- 7 **Ahmed, T.** Combined dataset of elemental X-ray line properties. R package, GitHub. DOI: 10.5281/zenodo.7742628 [↗](#)
- 8 **Ahmed, T.** Solar spectra and constants for photoelectrochemistry. R package, GitHub. DOI: 10.5281/zenodo.8034780 [↗](#)
- 9 **Ahmed, T.** Oxygen solubility in water. R package, GitHub. DOI: 10.5281/zenodo.3636202 [↗](#)
- 10 **Ahmed, T.** Properties of the chemical elements. R package, GitHub. DOI: 10.5281/zenodo.5898567 [↗](#)



# Contents

<b>List of symbols</b>	<b>xiii</b>
<b>List of abbreviations</b>	<b>xvii</b>
<b>List of reactants</b>	<b>xxi</b>
<b>1 Introduction</b>	<b>23</b>
1.1 A plentiful source of exergy . . . . .	23
1.2 The energy transition and resource scarcity . . . . .	24
1.3 Photocatalysis with inorganic semiconductors . . . . .	26
1.4 The race to the bottom: benefits and risks . . . . .	29
1.5 Will chemistry come to the rescue? . . . . .	31
1.6 Scope of this thesis . . . . .	32
<b>2 Synthesis and preparation</b>	<b>35</b>
2.1 Electrodeposition of ZnO NR arrays . . . . .	36
2.2 Chemical bath deposition of CdS films . . . . .	39
2.3 Atomic layer deposition of iron oxide . . . . .	40
2.4 ZnO quantum dot synthesis . . . . .	42
<b>3 Characterization methods</b>	<b>45</b>
3.1 UV-Vis spectroscopy . . . . .	45
3.2 Photoluminescence spectroscopy . . . . .	46
3.3 Raman spectroscopy . . . . .	47
3.3.1 Resonant Raman scattering . . . . .	50
3.4 Photocatalysis . . . . .	50
3.4.1 The solar spectrum . . . . .	51
3.4.2 Photocatalysis rigs . . . . .	53
3.4.3 Dyes . . . . .	56
3.5 Electron microscopy . . . . .	58
3.5.1 Scanning electron microscopy . . . . .	58
3.5.2 Transmission electron microscopy . . . . .	60
3.6 X-ray methods . . . . .	60
3.6.1 Thin-film X-ray diffraction . . . . .	60
3.6.2 X-ray spectroscopy . . . . .	62
<b>4 Algorithms &amp; datasets</b>	<b>65</b>
4.1 Notes on spectral peak fitting . . . . .	67

4.2	Converting between reference electrode scales . . . . .	67
4.3	Tauc fit algorithm . . . . .	68
4.4	Dataset of band edges and gaps . . . . .	68
4.5	Dataset of X-ray transition lines . . . . .	70
4.6	Dataset of some properties of the elements . . . . .	71
<b>5</b>	<b>Optical quantum confinement in low-dimensional ZnO</b>	<b>73</b>
<b>6</b>	<b>Results</b>	<b>77</b>
6.1	PC properties of ZnO/CdS nanoarrays . . . . .	77
6.2	ZnO/Fe <sub>2</sub> O <sub>3</sub> core-shell nanorods . . . . .	82
6.3	Non-degradative processes in methylene blue dye . . . . .	87
6.4	Photocatalysis with quantum-confined ZnO . . . . .	88
6.5	Long-term tracking of growth of ZnO QDs . . . . .	90
6.6	Non-resonant Raman in nano-dimensional ZnO . . . . .	92
6.7	Resonant Raman in nano-dimensional ZnO . . . . .	93
<b>7</b>	<b>Summary and outlook</b>	<b>97</b>
<b>8</b>	<b>Populärvetenskaplig sammanfattning</b>	<b>99</b>
	<b>Acknowledgements</b>	<b>103</b>
	<b>References</b>	<b>105</b>
	<b>List of figures</b>	<b>125</b>
	<b>List of tables</b>	<b>126</b>
	<b>List of reactions</b>	<b>127</b>
	<b>Colophon</b>	<b>129</b>

# List of symbols

- $A$  *absorbance*, the decadic logarithm of the incident spectral radiant power divided by the transmitted spectral radiant power,  $A = \log \left( \frac{I_0}{I} \right)$ , assuming reflection or scattering is negligible [4–7] 45, 46
- $\alpha$  *absorption coefficient*, energy absorbed per unit time and unit volume divided by the incoming energy flux in a media [8]. It expresses the extent to which incident light is damped as it passes through a material 45, 46, 57, 68, 87, 88, *see A*
- $E_g$  /eV  
*band gap*, the energy separating the top of the valence band from the bottom of the conduction band. In semiconductors and insulators the band gap is an interval where electronic states are forbidden 26, 62, 68, 73–76, *see VB & CB*
- $E_B$  /eV  
*binding energy*, the difference between the total energy of the system before and after emission of a core-level electron 62, 63, *see PES & BE*
- $a_B$  /nm  
*exciton Bohr radius*, the radius of the exciton in a bulk semiconductor. Not to be confused with the Bohr radius,  $a_0 = 0.529 \text{ \AA}$ , which is the most probable distance between the nucleus and  $e^-$  in a H atom 74, 75
- $k$   $\equiv 1.380\,649 \times 10^{-23} \text{ J K}^{-1}$   
the *Boltzmann constant* is a proportionality factor that relates the average thermal energy of particles in a gas with the thermodynamic temperature of the gas 51
- $\epsilon_r$  *relative permittivity* (dielectric constant) of a material, ratio of the frequency-dependent permittivity of the material and the vacuum permittivity 74–76, *see  $\epsilon_0$*
- $m_e$   $= 9.109\,383\,701\,5(28) \times 10^{-31} \text{ kg}$   
*mass of a stationary electron*, also known as the invariant mass of the electron 75
- $q_e$   $\equiv 1.602\,176\,634 \times 10^{-19} \text{ C}$   
*elementary charge*, the negative electric charge carried by a single electron 75, 76
- $E_F$  /eV  
*Fermi level*, the energy at which all of the lower energy states of a material at 0 K are occupied while all of the higher states are unoccupied. At non-zero temperatures it is the energy level at which a state has 50 % chance of being occupied xvi, 63, 73

- $E_{\text{fb}}$  *flatband potential* of a semiconductor, potential where the Fermi level of the semiconductor must be equal to the redox Fermi level of the electrolyte 69, *see*  $E_{\text{F}}$
- $\nu$  /Hz  
*frequency* of electromagnetic radiation (the inverse of wavelength) 62, 68, *see*  $\lambda$
- $I$  *irradiance* or *intensity* is the radiation power per area that is received at a surface. This notation is commonly used in applications involving collimated beams of light, such as spectrometric analysis [5] 24
- $E_{\text{k}}$  /eV  
*kinetic energy*, the amount of momentum owned by an emitted electron in a PES experiment. Read [9] for details xvi, 62, *see*  $\phi$  & PES
- $M$  /g mol<sup>-1</sup>  
*molar mass*, formerly known as formula weight, is the mass of a sample of a compound divided by the amount of substance in that sample. It is different from the molecular mass, which is the mass of a given molecule xvii, xviii
- $\Phi$  /s<sup>-1</sup> m<sup>-2</sup>  
*photon flux*, the number of photons incident on a surface per unit time per unit area 24
- $h$   $\equiv 6.626\,070\,15 \times 10^{-34}$  J s  
*Planck constant*, a proportionality constant relating a photon's energy to its frequency, and foundational to the quantization of light and matter. The so called *reduced Planck constant* is  $\hbar = h/2\pi$  51, 62, 68, 75, 76
- $\Omega$  /cm<sup>-1</sup>  
*Raman shift* is a relative measure of the energy or frequency *difference* between the Rayleigh line and the observed Raman scattering 92, 94
- $R$  /%  
*specular reflectance*, usually in terms of an optically thin film. *See* section 3.1 45, 46
- $S$  *diffuse scattering*, usually in terms of an optically thin film. *See* section 3.1 45
- $K_{\text{sp}}$  *solubility product*, the equilibrium constant for a solid substance dissolving in an aqueous solution 40

$I_{(\lambda,T)}$	the <i>spectral radiance</i> , or the specific radiative intensity, of a black body in a cavity in thermodynamic equilibrium is isotropic, time-independent and spatially homogeneous 51
$c$	$\equiv 299\,792\,458\text{ m s}^{-1}$ <i>speed of light</i> , the speed limit of the universe. Photons can travel at this speed in vacuum. In some circumstances, even light in vacuum travels at <i>less than</i> $c$ [10]. In dry air, $c = 299\,709\,199\text{ m s}^{-1}$ due to its relative refractive index being $n = 1.000\,277\,8$ (at $15^\circ\text{C}$ , $101.325\text{ kPa}$ , and $\lambda = 550\text{ nm}$ ). In general, the speed of light in a medium is $c_n = c/n$ , where $n$ is the refractive index 51
$T$	/K <i>absolute temperature</i> on the Kelvin scale, where 0 is at absolute zero 48, 51, 68
$T_a$	/°C <i>annealing temperature</i> 92
$T$	/% <i>transmittance</i> , usually in terms of an optically thin film. See section 3.1 45, 46
$E_{\text{VAC}}$	/eV the local <i>vacuum level</i> , the energy level of an electron at rest within a few nanometres from the surface, i.e., with zero kinetic energy with respect to the surface [11]. This is not the same as the vacuum level at infinity, $E_{\text{VAC}(\infty)}$ xvi
$\epsilon_0$	$= 8.854\,187\,812\,8(13) \times 10^{-12}\text{ F m}^{-1}$ <i>vacuum permittivity</i> , or the absolute dielectric permittivity of classical vacuum, or the permittivity of free space 75
$\lambda$	/nm <i>wavelength</i> of electromagnetic radiation (the inverse of frequency) xvi, 47, 51, 60, 61, <i>see</i> $\nu$
$\phi$	<i>work function</i> , the minimum amount of energy needed to remove an electron from a solid to immediately outside its surface. It is the difference between the Fermi level, $E_F$ and the vacuum level, $E_{\text{VAC}}$ 62, <i>see</i> $E_F$ , PES & $E_{\text{VAC}}$





# List of abbreviations

- ALD** atomic layer deposition 32, 41, 42, 59, 83, 91, 97
- AM** air mass, see figure 3.3 51–53
- AM1.5G** air mass 1.5 global tilt, see figure 3.3 24, 50, 52, 54, 55, 97
- AOP** advanced oxidation processes 31
- AVS** absolute vacuum scale, the absolute electrochemical reference scale. Related to the SHE scale as 0 V vs. SHE = −4.44 V vs. AVS at 298.15 K in aqueous solution [12] 28, *see* RE
- BE** binding energy *see* PES &  $E_B$
- CB** conduction band 28, 74, 78, 81, 89, 98
- CBD** chemical bath deposition 39, 40, 47, 59, 77, 78, 97
- CBE** conduction band edge 29, 69, 90, *see* CB
- CE** counter electrode 36, 38, *see* RE & WE
- CFL** compact fluorescent light 53, 54
- DOS** density of states 73
- DSSC** dye-sensitised solar cell 57
- EBT** eriochrome black T, reactant **12**, an azo dye with  $M=461.38 \text{ g mol}^{-1}$  (c.f. scheme 1c) 56, 80, 97
- ECD** electrochemical deposition 59
- EDS** energy dispersive spectroscopy 63, 70, 78, 83
- ESCA** electron spectroscopy for chemical analysis xix, 63, *see* XPS
- exc** excitation, e.g., as in *wavelength of excitation* 47, *see*  $\lambda$
- FIB** focused ion beam 83, *see* SEM
- FTO** fluoride-doped tin oxide, an optically transparent and electrically conducting oxide 36, 78, 79, 82–84, *see* TCO
- FWHM** full-width half maximum 54, 61, 67, 96
- GHG** greenhouse gases, gases in the atmosphere that absorb energy within the infrared range, causing the greenhouse effect. The gases contributing most to infrared absorption are  $\text{CO}_2$  and  $\text{CH}_4$ . The former has a lifetime of around 300 year, whereas the latter has a much shorter lifetime of tens of years, making  $\text{CO}_2$  the most potent of the greenhouse gases 23, 25, 65
- GI-XRD** grazing incidence X-ray diffractometry 60, 83, 97
- HER** hydrogen evolution reaction 25, 28

**Hm** hematite ( $\alpha$ -Fe<sub>2</sub>O<sub>3</sub>), the thermodynamically stable polymorph of iron oxide at ambient conditions 40, 41, 49, 83, 86

**IR** infrared, a broad band in the electromagnetic spectrum comprising radiation above 2500 nm xviii, 24, 47, 49, 86, *see* Vis & UV

**KE** kinetic energy *see* PES &  $E_k$

**LED** light-emitting diode 35, 53–55, 80

**MB** *methylene blue*, reactant **10**, a cationic thiazin dye with  $M=319.85 \text{ g mol}^{-1}$  (c.f. scheme 1a) 33, 56–58, 87–90, 97

**MO** *methyl orange*, reactant **13**, an azo dye with  $M=327.33 \text{ g mol}^{-1}$  (c.f. scheme 1d) 56

**NIR** near infrared, the high-energy part of the infrared band, immediately above the visible band in terms of wavelength. Customarily defined to span 780 nm to 2500 nm 24, 57, *see* Vis & IR

**NP** nanoparticle 42, 74, 88

**NR** nanorod 32, 35, 36, 39–41, 47, 77, 79, 80, 82, 83, 86

**OER** oxygen evolution reaction 25, 28

**PC** photocatalysis 25–27, 29, 32, 33, 35, 46, 50, 53–56, 77, 80–82, 87, 90, 97, 98

**PDF** powder diffraction file 61, *see* PXRD & XRD

**PEC** photoelectrochemistry xix, 50, 79, 81, 97

**PES** photoelectron spectroscopy xv

**PL** photoluminescence spectroscopy 46, 78, 79

**PV** photovoltaic 25, 26, 29, 30, 35

**PXRD** powder X-ray diffractometry 77, 92

**PZZP** point of zero  $\zeta$  potential, the pH at which the potential drop across the Helmholtz layer is zero 69

**QD** quantum dot 33, 42–44, 74–77, 87–91, 97

**RB5** *reactive black 5*, reactant **11**, an azo dye with  $M=991.82 \text{ g mol}^{-1}$  (c.f. scheme 1b) 56, 57

**RE** reference electrode 36–38, *see* CE & WE

**ROS** reactive oxygen species 57, 90, *see* AOP

**RT** room temperature, this term is not exactly defined, but usually means 20 °C 35, 49, 77, *see* STP

**SEM** scanning electron microscopy 49, 58, 59, 78, 82, 83

**SHE** standard hydrogen electrode xvii, 28, *see* RE

**STP** standard temperature and pressure 25, 26, 41

**TCO** transparent conducting oxide 35, 38, 47, 59, 78, 79, 82, 97

**TEM** transmission electron microscopy 58–60, 78, 83

**UV** ultraviolet, band in the electromagnetic spectrum immediately below the visible band in terms of wavelength, usually demarcated at 380 nm. Sometimes divided into UV-A (315 nm to 400 nm), UV-B (280 nm to 315 nm), and UV-C (100 nm to 280 nm), but for photoelectrochemical (PEC) applications we limit the UV band to 250 nm to 380 nm, as lower wavelengths are non-existent in the terrestrial solar spectrum due to the atmosphere acting as a very effective bandstop filter 24, 32, 50, 53–55, 79, *see* Vis & IR

**UV-PL** ultraviolet photoluminescence spectroscopy *see* UV & PL

**UV-Vis** ultraviolet and visible bands of the electromagnetic spectrum, usually defined to span 280 nm to 780 nm 46, 54, 55, 68, 76, 78, 80, 88, 101, *see* Vis & IR

**UV-Vis-IR** ultraviolet, visible, and infrared bands of the electromagnetic spectrum, usually defined to span 280 nm to 2500 nm *see* UV, Vis & IR

**UV-Vis-NIR** ultraviolet, visible, and near infrared bands of the electromagnetic spectrum, usually defined to span 280 nm to 2500 nm 46, 56, 87, *see* UV, Vis & NIR

**VB** valence band 28, 74, 78

**VBE** valence band edge 29, 41, 69

**Vis** visible spectrum, usually defined to span 380 nm to 780 nm 24, 54, *see* UV & IR

**VLM** visible-light microscopy 58, *see* SEM & TEM

**WE** working electrode 36–38, *see* CE & RE

**XPS** X-ray photoelectron spectroscopy, also known as ESCA 62, 63, 85, *see* PES

**XRD** X-ray diffractometry 49, 60–62, 67, 77, 85

**XRF** X-ray fluorescence 62, 63, 67, 70



# List of reactants

- 1     $\text{ZnCl}_2$
- 2     $\text{KCl}$
- 3     $\text{CdSO}_4$
- 4     $\text{CdSO}_4 \cdot \frac{8}{3} \text{H}_2\text{O}$
- 5     $\text{CH}_4\text{N}_2\text{S}$
- 6     $\text{NH}_3$
- 7     $\text{Zn}(\text{OAc})_2 \cdot 2 \text{H}_2\text{O}$
- 8     $\text{LiOH} \cdot \text{H}_2\text{O}$
- 9     $\text{EtOH}$
- 10   3,7-bis(dimethylamino)-phenothiazin-5-ium chloride
- 11   2,7-naphthalenedisulfonic acid,  
4-amino-5-hydroxy-3,6-bis[[4-[[2-(sulfooxy)ethyl]sulfonyl]phenyl]azo]-,  
tetrasodium salt
- 12   sodium 4-[2-(1-hydroxynaphthalen-2-yl)hydrazin-1-ylidene]-7-nitro-3-oxo-3,4-di-  
hydronaphthalene-1-sulfonate
- 13   sodium 4-[4-(dimethylamino)phenyl]diazenylbenzene-1-sulfonate



# 1. Introduction

The Sun is the primary source of energy for all living organisms, and together with the cycle of day and night it is the motive force powering the planet [13]. Humans have always organized their lives and their settlements around the sun, to draw warmth from it or to seek shade from it, since the earliest civilizations [14]. The modern world has, over the last couple of centuries, slowly turned to fossil fuels for both domestic and industrial uses, and as we discovered more and more coal, gas, and oil we have allowed our industry, agriculture, transportation, and domiciles to become almost entirely dependent on them. The resultant soot and pollution were obvious to anyone, but the effect of CO<sub>2</sub> on the climate perhaps less so. Still, the first scientific reports warning about its heating effect on the atmosphere were published so long ago [15–17] that they predate the discovery of the electron [18]. By the end of the 1950s, anyone who read a mainstream newspaper would have been aware of the basic idea of climate change due to anthropogenic combustion of fossil fuels [19].

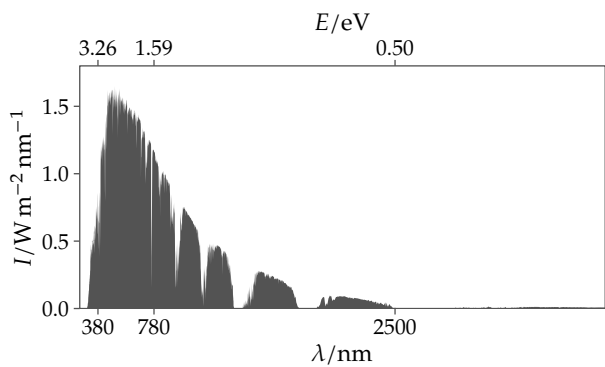
Fossil fuels are the remains of ancient flora and fauna, compressed deep inside the Earth for tens of millions of years. Importantly, these hydrocarbons have been removed from the biosphere for just as long. And we have been reintroducing them at a mind-boggling rate: in a single year, we burn 55 trillion tonnes (that's  $55 \times 10^{15}$  kg) of this ancient carbon, which is by mass a hundred times more than everything alive today (if we only count the carbon atoms). Perhaps even more worryingly, over half of all the anthropogenic greenhouse gas (GHG) deposited into the atmosphere has occurred since 1990, and all around the world we are still prospecting for new oil and gas fields.

Due to the urgency of transitioning the energy system to a renewable basis, scientific and technological advancements cannot solve it alone. To successfully transition the energy system and industry to the power of sunlight, economic incentives and policy must also align with this aim [20–22]. And our societies must realize the need for an energy diet that respects the physical limits of our biosphere [23, 24].

## 1.1 A plentiful source of exergy

The Sun is and always has been the main source of exergy in the solar system. From it light radiates in all directions (of the Sun's total radiance about two parts out of 100 000 impinges Earth). Light is nature's way of transferring energy through space.

1. Introduction



**Table 1.1.** *Relative spectral power density and flux*

	<i>I</i> /%	<i>Φ</i> /%
UV	3.2	1.3
Vis	53.4	36.1
NIR	42.6	59.3
IR	0.8	3.2

Figure 1.1. The AM1.5G reference solar spectrum.

The day-side of Earth continuously receives 343 754 TW of sunlight (just outside the atmosphere), which after correcting for Earth’s albedo and the fraction irradiance absorbed by the atmosphere (0.3 and 0.19, respectively) yields a solar power of 175 314 TW. This is instantaneous *power*, and summing over the number of hours in a year yields an annual solar energy input of 5 532 500 EJ, which is around 10 000 times greater than the world’s annual energy consumption,<sup>1</sup> or in other words: in one hour the planet receives more solar energy than humanity expends in a whole year. Next to solar power all other energy forms pale in comparison.

As far as we are concerned, sunlight is infinite, and only our imagination and technology limits what we can use it for. This is where modern chemistry and engineering comes into the fore.

In this thesis, I will make the case for a more widespread use of photocatalysis for production of solar fuels and for the proliferation of photocatalysts for the degradation of environmental pollutants by exploiting low-dimensional ZnO alone and in combination with CdS and Fe<sub>2</sub>O<sub>3</sub>.

1.2 The energy transition and resource scarcity

The idea of an energy system based on renewable power is not new at all. Exactly one hundred years ago, the evolutionary biologist J. B. S. Haldane laid out a practical vision for the future energy system of England, saying [26, 27] “the country will be covered with rows of metallic windmills” feeding electricity through the grid to power stations where “the surplus power will be used for the electrolytic decomposition of water into oxygen and hydrogen”, and that the initial costs would be very considerable, but “energy will be as cheap in one part of the country as another, so that industry will be greatly decentralized; and that no smoke or ash will be produced”. Of course, by that time the United

<sup>1</sup>Which was 178 899 TWh or 644 EJ in 2022 (equivalent to 280 million barrels of oil per day) [25].



Kingdom had been burning fossil fuels for almost 150 years already, and people were getting really worried about the visible smoke and smog engulfing their cities. But we should note that Haldane envisioned this pollution-free energy system to happen *four hundred years* into the future, which is quite pessimistic, although to be fair we have not managed to beat his prediction yet.

A known problem with the energy transition is that all development of renewable energy systems is currently, and for the foreseeable future, built on logistics fed with *non-renewable* power [28]. Thus, producing the materials needed to provide renewable power (photovoltaic (PV) panels, wind turbines, electrolyzers, etc.) necessarily equates to emission of GHG. If we expect to operate all other industry as usual, then the energy transition itself will necessarily produce even more emissions. The only reasonable way out of this conundrum is to realize that the energy transition, if managed responsibly, must lead to a sort of self-imposed energy scarcity (perhaps that is a “good thing”, considering how wasteful the modern mass-consumption economy has been).

Equally important is the question of how we will source the chemicals necessary to build the required renewable power generation infrastructure. Figure 1.2 considers the availability of the chemical elements commonly used in photocatalytic compounds.

Water is a critical resource for the energy transition. Worldwide, we use more than  $4 \times 10^{12} \text{ m}^3$  of freshwater each year.<sup>2</sup> Yet, three billion people are affected by water scarcity, and two billion of them lack access to safe drinking water [29]. By 2050, the demand for freshwater is projected to increase by more than 40 %.

A perhaps overlooked aspect of our fossil-based energy conversion system is that electrical power generation consumes a lot of freshwater. In fact, of the various electrical power generation methods at our disposal (coal/gas, nuclear, hydro, solar, wind, etc.) the renewable generators (except for hydropower) consume hundreds or even thousands of times *less* freshwater to generate the same amount of electricity [30].<sup>3</sup> In many countries, the electrical generation sector consumes *more* freshwater than their agricultural sector.

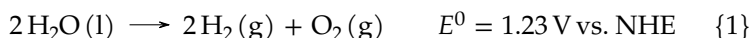
The electrolysis of water into  $\text{H}_2$  and  $\text{O}_2$  (reaction {1}), also called *water splitting*, requires around 9 kg of  $\text{H}_2\text{O}$  to produce 1 kg of  $\text{H}_2$  and is an “uphill” reaction with a large positive Gibbs free energy,  $\Delta G^* = 238 \text{ kJ mol}^{-1}$  or  $\Delta G^* = 1.23 \text{ eV}$ , comprising two half reactions, viz., the hydrogen evolution reaction (HER) and the oxygen evolution reaction (OER) (here shown under acidic conditions at standard temperature and pressure (STP)):

---

<sup>2</sup>Agriculture accounts for 70 %, industry 19 % and households 10 %.

<sup>3</sup>With that in mind, we can see that operating a desalination plant on non-renewable generated electricity would actually waste water, or in the best case simply represent a transfer of freshwater resources from the desalination plant to the power plant powering it. Desalination plants should be solar powered. Recent research have shown that it is even possible to simultaneously desalinate and produce electricity using a composite PV-membrane device [31].

## 1. Introduction



But in practice, an electrolyser splitting water may require up to ten times more water than stoichiometry demands.<sup>4</sup> Even when accounting for this, the water resources required for a renewably based energy system are significantly lower than for a fossil-based system.

Even if we accept the notion that *total* primary energy production must decrease to achieve the energy transition, the inherent distributed nature of renewable power generation [32] might actually mean that a larger number of people get access to more electrical power than today. There is no inherent benefit nor any technical reason to centralize solar power generation; its inherently distributed nature makes it a more resilient power generation system.

Photoelectrochemistry lies at the cross-roads between energy and water, two resources that will always be vital to society, but perhaps now more than ever. It is our responsibility as a field to advice on how to produce sustainably sourced photocatalysts for solar fuels production or for the photodegradation of pollutants. I believe our aim must be to convert this carbon society into a photon society.

### 1.3 Photocatalysis with inorganic semiconductors

Over 90 % of all chemicals and fuels are estimated to be produced with the aid of some catalyst [33], and catalysts contribute directly to around a third of the world's economy [34]. Most commercial catalytic processes are heterogeneous, and commonly employ disperse particles on high-surface area supports.

Photocatalysis (PC) is the acceleration of a photoreaction by the presence of a catalyst [35, 36].<sup>5</sup> A benefit of PC is that it may (and indeed often does) rely on atmospheric oxygen gas as the oxidant and that it can be carried out at STP [37]. Photocatalysis can be employed in quite varied settings, in this thesis we will primarily concern ourselves with the production of energy-rich chemicals (e.g., solar fuels such as  $\text{H}_2$ ) and the degradation of harmful organic compounds in water (water purification).

Photocatalysts are an important complement to PV cells in the renewable energy transition. Whereas PV generates electrons in an external circuit, PC

---

<sup>4</sup>Taking into account water treatment to meet the electrolyser's purity requirements, water for cooling the electrolyser, and water for cooling the produced  $\text{H}_2$ .

<sup>5</sup>Note that the light is *not* the catalyst, but rather a reactant. The source of the light can be anything, really, but most commonly natural sunlight. There is, as we have seen, a lot of it, and the price cannot be beat. It could also be simulated sunlight, or a lamp, as long as it emits photons with an energy above the band gap of the photocatalyst.

### 1.3 Photocatalysis with inorganic semiconductors



Figure 1.2. Photocatalytic compounds are often constituted of either  $d^0$  or  $d^{10}$  cations (highlighted) and nitrogen or chalcogenide anions (highlighted) [39, 40]. For a photocatalyst to be relevant at the scale required for the global energy transition, the constituent elements must also be readily available [41] (see colour legend).

utilizes locally photogenerated charge carriers that can induce a chemical redox reaction. Many cheap, non-toxic and commonly available semiconductor materials are also quite effective photocatalysts (c.f. figure 1.2).

Heterogeneous catalysis is when the catalyst and catalysed species are in different phases. In this context, heterogeneous photocatalysis is the process of inducing chemical reactions using an irradiated photocatalyst's surface, e.g., inorganic semiconductor surfaces [38], usually while immersed in aqueous solution. At the fundamental level an irradiated semiconductor nanoparticle can be considered an electrochemical cell performing work, whose anodic and cathodic photoreactions are in steady-state conditions. The photocurrent and the internal photovoltage give the electric power of the cell, and the particle/cell achieves an electrochemical potential that depends on the relative rate of its two half-cell reactions [38].

But despite  $\text{TiO}_2$  having the honour of practically defining the field of heterogeneous inorganic photocatalysis, the study of  $\text{ZnO}$  as a PC actually predates  $\text{TiO}_2$ . The earliest description of photocatalysis using  $\text{ZnO}$  dates back to 1911 in experiments by Alexander Eibner bleaching Prussian blue using illuminated  $\text{ZnO}$  [42], and its earliest use for the photolysis of water is from 1953 [43, 44]. In contrast to anatase  $\text{TiO}_2$  with its indirect band gap, wurtzite  $\text{ZnO}$  has a direct band gap and thus higher absorption coefficient, and similar positions of the conduction and valence band edges ( $-0.5$  V vs. NHE and  $2.8$  V vs. NHE at pH5), and have the advantage of a significantly higher charge carrier mobility [45, 46].

# 1. Introduction

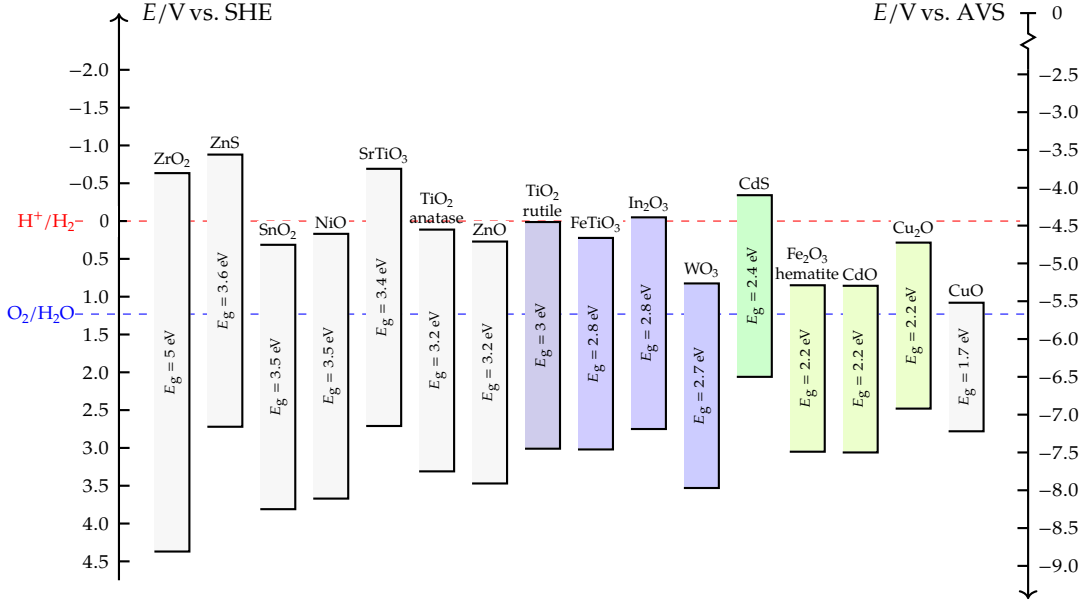


Figure 1.3. Valence band (VB) and conduction band (CB) edges for bulk semiconductor chalcogenides plotted at pH0 and 298 K compared with the reduction potential of hydrogen evolution (red) and oxygen evolution (blue) from H<sub>2</sub>O vs. both the standard hydrogen electrode (SHE) and absolute vacuum scale (AVS) reference scale (dataset from **CONTRIB. 4**). Materials are shown in order of decreasing band gap. Note that ZnO is unstable at this pH, but since for all oxides Nernstian dependence (see eq. (4.2)) can safely be assumed, their band edges could be arbitrarily redrawn at any pH. Fill colour illustrates the *absorbed* wavelength, based on the spectral model developed by Aphalo [47] (the same colour model is used in scheme 1).

## 1.4 The race to the bottom: benefits and risks

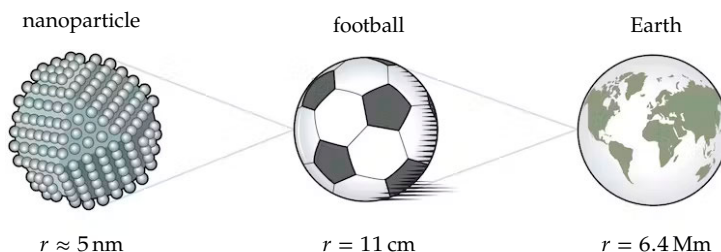


Figure 1.4. The size of a nanoparticle can be hard to grasp because it is such an unfamiliar object. A valid analogy (in terms of relative size) is the following: if we imagine that a nanoparticle is the size of a football, then a football would be the size of planet Earth. Each step in this illustration corresponds to changing the radius by a factor of  $10^7$ .

© The Nobel Foundation.

In metal oxides, the valence band edge (VBE) is determined primarily by the orbitals on the  $\text{O}^{2-}$  anion, and the conduction band edge (CBE) by metal cations and their bonding geometry.

The band gap of a semiconductor can be tuned using different methods: via the quantum size effect, or phase transformations, or solid solutions with other elements. In this thesis we have explored the quantum size effect on the band gap of ZnO (c.f. chapter 5).

Perhaps it would not be a mischaracterization to say that the ultimate goal of photocatalysis is to design a PC made out of cheap and non-toxic materials with excellent stability in water under irradiation; with a band gap  $\geq 1.6 \text{ eV}$  whose band edges straddle the  $\text{H}_2\text{O}$  redox potentials; and that performs the photocatalysed reaction at a high rate and for a long time. Although the search for that holy graal will surely continue, in the present the pressing need for quickly implementable solar-based energy generation suggests that we should make do with what we have. And what we have is very cheap PV panels and an increasing number of electrolyzers.

## 1.4 The race to the bottom: benefits and risks

Many physical and chemical properties of a material change when the constituent particles become sufficiently small. A particle with a diameter between 10 nm to 100 nm is said to be “nano”-sized, while larger particles than that are commonly referred to as sub-micron or micron-sized. But how small is a nanoparticle? Getting a grip on that is mind-bendingly hard. In figure 1.4 we try to put it into some perspective.

Of course, there is a limit to how small stuff we can build, and that is set by the size of the atoms themselves. An  $\text{O}^{2-}$  ion has a diameter of 0.28 nm, and a  $\text{Zn}^{2+}$  ion has a diameter of 0.15 nm (based on ionic crystal radii).

If particles are made into nanometre dimensions, the most noticeable change is the large increase in specific surface area (area per weight of the material),

## 1. Introduction

and thus the potential to substantially increase chemical activity at the exposed surfaces. The size of the material also changes how light interacts with it. If a nanoparticle is made small enough (depending on its composition) something rather special happens: its electronic states are literally *squeezed* by the constricted dimensions of the nanoparticle, which results in drastic changes in the material's electronic and optical properties. This phenomenon is termed *quantum confinement* and is elaborated in chapter 5.

Although humans have benefitted from the use of nanoparticles or nanostructured materials for millennia [48] (often unwittingly), we are by no means alone in doing so. Many birds have iridescent plumage and many insect exoskeletons have intricate nanostructured surfaces that create pigment-less (structural) colouration by reflecting incident light in very specific ways [49, 50]. In terms of sophistication, engineered nanostructures cannot yet compete with their counterparts in nature. The study of such nanostructures is a major interest for applications towards improving the efficiency of PV panels or in technological applications such as waveguides towards light-based computing.

Modern scientific investigations into nanoparticles were first undertaken in the late 19<sup>th</sup> century by Scottish scientist John Aitken when he took an interest in something as mundane as dust. At the time, it was obvious that the transparency of the air correlated to the amount of dust (and to the relative humidity). Aitken was the first that set out to measure these effects, and created a method for measuring these suspended dust particles in air [51], then miniaturized the device and promptly set about travelling across Europe to collect measurements ("the portable apparatus is reduced to such dimensions that it adds but little to one's personal luggage") [52]. Aitken's device was the first example of a condensation particle counter, which works by introducing airborne particles into a supersaturated vapour, where the particles act as nucleation points for the vapour to form droplets that are then counted using optical techniques. Using this technique one can detect the presence of particles down to a few nanometres in size. This was the first demonstration of a characterization technique to quantify nanoparticles (particles below 50 nm are generally undetectable with light-scattering optical particle counters), but less than 50 years later it was supplanted by the electron microscope.

Nanotechnology is the latest in a long line of technologies that promises better living through chemistry [53]. But it would behoove us to root our expectations in history, which can be an unforgiving teacher if forgotten. Only during the 20<sup>th</sup> century, chemical industry managed to spread DDT over every continent, freon into the stratosphere, and lead in every city by the combustion of leaded petrol. To be fair, the chemical industry has also been the source of some of our modern world's greatest successes, such as the catalytic Haber–Bosch process that has fed the world, vaccines that have wiped out polio and many other debilitating diseases, and the production of an amazing range of materials that have made our lives healthier and safer. Perhaps it is no wonder that we believe the nano-fication of chemistry will lead to similar rapid advances.

I guess what I am trying to convey is that we must make ourselves aware of the risks, and to do that some creativity and humility is called for. The risks of nanosized materials may not always be the same as those experienced by earlier generations of chemists, and widely spreading a technology that “works in the lab” comes with its own set of new risks. Chemists as well as chemical industry regulators (especially in the EU and USA) have a good grasp of the risks with most industrially manufactured chemicals. The main risks we need to consider are those towards human health and towards the environment. This is something that is still being actively researched [54–57], and for that reason those working in the field would do well to be cautious and avoid hyperbole when expressing the benefits of nanotechnology. When it comes to risk management, the hardest challenge might be to figure out what exactly we should be measuring in the first place; what material and particle attributes are most closely associated with health risks, and at what exposure levels? [58]

## 1.5 Will chemistry come to the rescue?

There is no denying that many of the technological and environmental challenges ahead of us are well-suited for chemical solutions. Chemistry has developed technologies and materials that can reduce pollution, improve waste management, and clean up contaminated environments. For example, catalytic converters in cars use chemical reactions to convert harmful exhaust gases into less harmful compounds before they are released into the air. Chemistry has also helped us develop materials such as activated carbon and zeolites that can absorb and remove pollutants from air and water. Additionally, chemistry has played a crucial role in developing principles of “green chemistry”, that aims to design chemical products and processes that are safe, sustainable, and minimize waste.

A not yet realized application for photocatalytic degradation lies in the complete destruction of synthetic chemicals from various waste streams. Synthetic chemicals of all kinds are produced in increasing quantities all over the world, and pollution by their release into the environment is growing [59]. In particular, pharmaceuticals are dispersed in the environment via water treatment plants that are presently ill-equipped to remove such compounds from the effluent, but worse than that, the pharmaceutical production plants themselves are a major source of local pollution and are frequently located in countries with lax environmental regulations. The Swedish government agency Naturvårdsverket published a report in 2017 [60] on advanced cleaning methods of effluent from pharmaceutical residues. The report mentions advanced oxidation processes (AOP) as a technology not yet in production, but showing promise for certain use cases, such as effluent with higher concentrations of pollutants. Ozonation has been in use in one treatment plant in Linköping since 2015.

Semiconductors are an excellent choice for photoactive materials, because their band gaps are well-suited to produce charge separation under solar irra-

## 1. Introduction

diation. For a *single* semiconductor material to split water (c.f. reaction {1}), its band gap must straddle the hydrogen and oxygen evolution reduction potentials of  $\text{H}_2\text{O}$  (c.f. figure 1.3) and it must allow efficient transport of both electrons and holes.

Unfortunately, such a semiconductor does not exist (or has not been found yet, despite well-organized research into photoelectrochemistry since at least the 1970s [40]). Wide gap semiconductors such as  $\text{TiO}_2$  or  $\text{ZnO}$  have band edges suitable for total water splitting, but on the other hand their band gaps are so large that they will only absorb ultraviolet (UV) photons which make up a very small part of the solar spectrum (c.f. table 1.1).

## 1.6 Scope of this thesis

Throughout this thesis we have studied the application of sunlight towards the synthesis of solar fuels or the degradation of chemicals with photocatalysts synthesized using cheap and easily scaled methods.

The work involved laboratory-scale wet-chemical synthesis of composite nanostructured films and colloidal low-dimensional nanoparticles; their experimental characterization using a variety of spectroscopic, microscopic, and diffractive methods; and proof-of-concept tests of their photocatalytic performance. Concurrently I got the opportunity to set up a laboratory from scratch (that was really fun!) and to create a personalized data analysis pipeline with an eye towards reproducibility and the sharing of code and data.

### PAPER I

In the first paper we set out to synthesize a large surface area nanodigitated photocatalyst “sandwich” of a wide gap semiconductor ( $\text{ZnO}$ ) coated with  $\text{CdS}$  for visible-light sensitization, which allowed us to optimize electrodeposition parameters and study the effect of  $\text{CdS}$  coating thickness vs. PC performance. Here the goal was to create a highly photoactive PC material with visible-light sensitivity via an experimentally simple and economically scalable method, which we achieved by using electrodeposition and chemical-bath deposition (both very established methods, and relatively simple in operation), although the visible-light sensitivity came at the cost of introducing the well-known toxicity of cadmium.

### PAPER II

In our second paper we looked for ways to avoid cadmium as well as making the outer coating more pH and photoresistant ( $\text{CdS}$  degrades under irradiation unless sacrificial agents are introduced in the electrolyte solution), and what could be more durable than literal rust? But for that to work the well-known extremely poor hole conductivity of  $\alpha\text{-Fe}_2\text{O}_3$  required the application of an extremely thin film on the  $\text{ZnO}$  NRs, which essentially demanded the use of atomic layer deposition (ALD). This allowed us to study how varying the  $\alpha\text{-Fe}_2\text{O}_3$  layer thickness affected the properties of the photoelectrodes.

### PAPER III

In the third paper we took a step back to study the question of how  $\text{ZnO}$  nanoparticle diameter in the quantum size regime influenced the redox potential of the photogenerated excitons. We did this by synthesizing colloidal



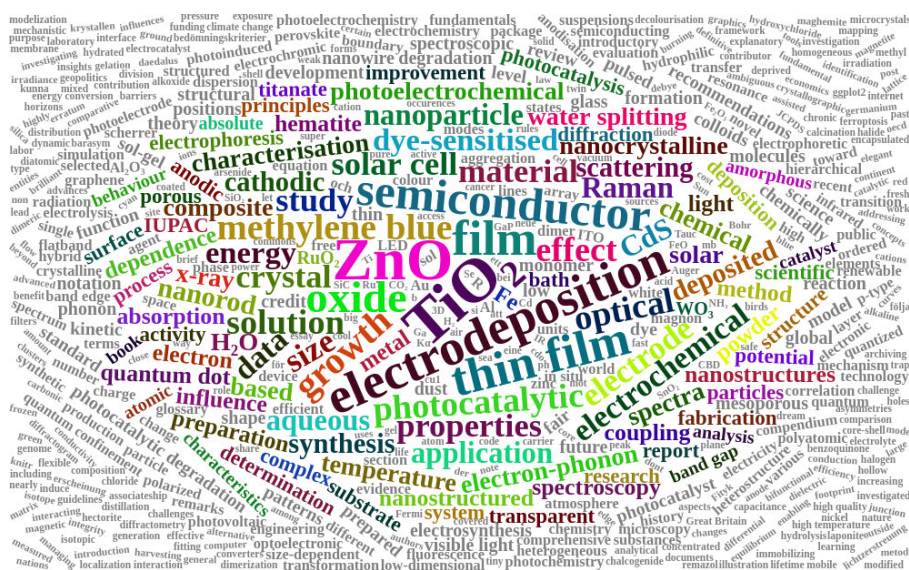


Figure 1.5. A dynamically generated word cloud of the most common words in all *titles* of works cited in this thesis. The titles form a corpus of 756 unique words across 218 cited works. With the 100 most frequent words highlighted in colour.

ZnO suspensions at varying average quantum dot (QD) diameter and measure their PC activity under simulated sunlight and simulators tracking the photodegradation of methylene blue (MB) dye. This kind of colloiddally suspended PC could be used to combat distributed pollutants using nothing more than natural sunlight and then naturally precipitate into relatively harmless ZnO sediment, a process aided by the ultrasmall size and large band gap of the PC particles.

In our fourth paper we take a deep dive into the vibronic properties of low-dimensional ZnO nanocrystals, via a series of Raman spectroscopy measurements where we quantify their phonon-phonon and electron-phonon coupling as a function of particle diameter.

This thesis also includes a chapter discussing the relative ease with which analytical reproducibility can be achieved with the use of freely available software, and also briefly presents some scientific software tools this author has publicly shared during this work.

Figure 1.5 shows a word cloud of keywords; not compiled ourselves, but rather *generated* from the corpus of all *titles* of all bibliographic records *cited in this thesis*. In a way, it is a *meta-visualization*: the thesis querying itself.

## 1. Introduction

## 2. Synthesis and preparation

In my synthetical work I strove for the simple, as far as possible. That mindset was based on the idea that if chemistry is to contribute to the conversion of our energy system at any scale, its proposed solutions must first and foremost be scaleable. That same idea was also behind our choice of elements—zinc and iron being plentiful and very cheap and practically non-toxic. Granted, we also used cadmium which is far from non-toxic, but on account of its sulfide being a commonly employed visible-light absorber in solar cells and because its synthesis method is very simple, it was too tempting a target to overlook.

At an early stage of this work we attempted to synthesize anatase  $\text{TiO}_2$  NRs on transparent conducting oxide (TCO), but after attempting several approaches including electrochemical deposition with templated membranes [61–69], cathodic electrodeposition in acidic baths [70–86], cathodic electrodeposition in alkaline baths [87–90], and anodic electrodeposition [91–97] without achieving the desired synthetical outcome apart from impressive clouds of hydrochloric acid (inside the fume hood, mind you) we looked for an alternative photocatalytic metal oxide that could be electrodeposited at mild processing conditions.

Zinc oxide is a semiconductor with known experimental methods of cathodic electrodeposition of thin films or nanostructures in aqueous electrolytes [98, 99], which we could easily adapt. ZnO wurtzite has attractive optical, electrical, and thermal properties, such as a wide and direct band gap (3.3 eV in the bulk at room temperature (RT)), a high absorption coefficient (due to its direct band gap), a large exciton binding energy<sup>1</sup> 60 meV, a high carrier mobility  $> 100 \text{ cm}^2 \text{ V}^{-1} \text{ s}^{-1}$  [101], and a high thermal conductivity, which makes  $\text{ZnO}$ <sup>2</sup> considered for applications in photocatalysis, solar cells, LEDs, transparent conducting films, and more and a viable alternative to  $\text{TiO}_2$  anatase.

$\text{ZnO}$  is amphoteric, reacting with both acids and bases, but it is nearly insoluble around neutral pH.<sup>3</sup> In acids it easily forms salts, and with increasingly alkaline conditions (starting from around pH 9) it is known to form monomeric hydroxide complexes from  $\text{ZnOH}^+$  to  $[\text{Zn}(\text{OH})_4]^{2-}$  [103, 104].

---

<sup>1</sup>The exciton binding energy is the energy needed to separate the electron and hole of an exciton into free charge carriers, i.e., the energy difference between the fundamental gap and the optical gap. It is significantly larger than  $kT$  (26 meV at RT), giving ZnO exciton emission even above RT. For comparison, GaN has an exciton binding energy of 18 meV to 28 meV [100].

<sup>2</sup>On a personal note, zinc was the first element that made a mark during my undergraduate education: at one of my cohort's very first lectures at the Arrhenius laboratory, our lecturer Lars-Johan Norrby proclaimed zinc to be his favourite element on the periodic table!

<sup>3</sup> $\text{ZnO}$  solubility at 298 K (25 °C) is  $1.23 \times 10^{-5} \text{ mol per } 100 \text{ g H}_2\text{O}$  [102], or  $\approx 1.0 \text{ mg per } 100 \text{ g}$ .

## 2. Synthesis and preparation

### 2.1 Electrochemical deposition of ZnO NR arrays

Electrochemical deposition is cheap, scalable, and affords relatively good control of the conditions during synthesis [105]. In addition, semiconductor thin-film electrodeposition is a mature technology, widely used in many industrial settings, and its basis in solution chemistry allows a wide range of synthetic parameters. Perhaps ironically then, the main disadvantages of electrodeposition are also related to solution chemistry: (relatively) complicated sample handling and residual electrolyte in the product.

Despite being cheap, electrodeposition allows shape-controlled synthesis of ZnO NRs *without* any capping agents or surfactant molecules that preferentially inhibit the growth of particular crystallographic facets, which was attractive to my experimental sensibilities.

We created ZnO NRs by cathodic deposition at  $-0.7$  V vs. Ag/AgCl for 90 min with an initial pulse at  $-1.3$  V vs. Ag/AgCl with a duration of 0.1 s, 0.5 s or 1.0 s. The aqueous electrolyte solution was ZnCl<sub>2</sub> **1** (0.1 mM) with KCl **2** (0.1 M solution in H<sub>2</sub>O). The electrodeposition was done at a temperature of 80 °C maintained using a thermostat-controlled water bath.

Our primary electrodeposition setup (see figure 2.1) used a CH Instruments 760C<sup>4</sup> bipotentiostat connected to a three-electrode cell with a CHI111 Ag/AgCl reference electrode and a CHI115 Pt wire counter electrode. Our secondary electrodeposition setup (see figure 2.2) used either a  $\mu$ AUTOLABIII<sup>5</sup> potentiostat or an AUTOLAB PGSTAT302N<sup>6</sup> connected to a three-electrode cell with an AUTOLAB reference electrode (RE) and a coiled Pt-wire counter electrode (CE).

The working electrode (WE) was fluoride-doped tin oxide (FTO) glass, i.e., sodalime<sup>7</sup> glass coated with a compact layer of fluorine-doped SnO<sub>2</sub> (TEC-7). The TEC-7 substrate has a sheet resistance of  $7\ \Omega\ \text{sq}^{-1}$ , is insoluble in dilute acids or alkalis, and microcrystalline with a highly oriented structure. Its impedance is low enough to allow direct-current cathodic deposition. The WE was kept at a potential negative to the reduction potential of O<sub>2</sub> (g), which causes oxygen gas near the electrode to be reduced to hydroxide ions (reaction {2a}). The hydroxide ions react with the zinc ions and form Zn(OH)<sub>2</sub>, ZnOOH or ZnO

<sup>4</sup>CH Instruments 760C was a compact bench-top bipotentiostat/galvanostat with a current range from 100  $\mu$ A to 1 pA and a voltage range  $\pm 10$  V.

<sup>5</sup>The  $\mu$ AUTOLABIII was a compact bench-top potentiostat with a current range from 10 mA to 10 nA and a voltage range  $\pm 5$  V with a resolution of 3  $\mu$ V. Controlled via a laptop computer running GPES v4.9 software.

<sup>6</sup>The PGSTAT302N was a high-current potentiostat/galvanostat with a current range from 1 A to 10 nA and a voltage range  $\pm 10$  V with a resolution of 3  $\mu$ V.

<sup>7</sup>Sodalime glass is a very common type of glass commonly used in containers, plate glass, microscope slides, pasteur pipettes and more. It does complicate analysis slightly due to containing several different oxides (in order of abundance): SiO<sub>2</sub>, Na<sub>2</sub>O, CaO, MgO, and Al<sub>2</sub>O<sub>3</sub>. Before deposition each cut glass substrate were prepared by ultrasonication in deionized H<sub>2</sub>O, followed by an EtOH and then an acetone rinse, and finally dried with N<sub>2</sub>.

## 2.1 Electrodeposition of ZnO NR arrays

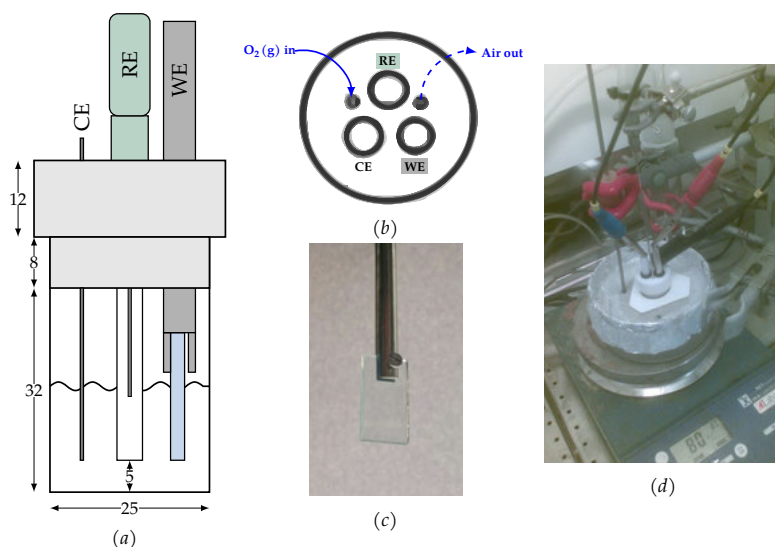
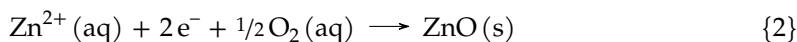
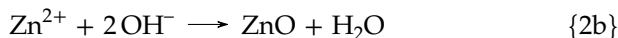


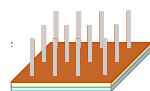
Figure 2.1. Primary setup for electrodeposition of ZnO. (a) Schematic (side view, to scale) of the low-volume cylindrical three-electrode cell used during electrodeposition, (b) the cell seen from the top, showing the location of the ports in the cap, (c) a photograph by the author of a mounted WE, and (d) an overview of the setup (water bath on hot plate inside the fume hood).

(reaction {2b}) depending on the temperature.



The oxygen was actively supplied to the electrolyte solution by either saturating the headspace with  $\text{O}_2(\text{g})$  flow or by bubbling it into the electrolyte solution.<sup>8</sup> In any case, the solution was saturated in oxygen *before* the deposition started, such that the oxygen concentration was kept as-close to constant as possible during the electrodeposition. The role of the supplied oxygen gas was to supply a source for the hydroxide ions needed at the working electrode. But note that this role could have been fulfilled by other means, for example using hydrogen peroxide, nitrate or other ions such as phosphate, carbonate, or sulfate.

Maintaining a steady temperature of 80 °C was just as important as maintaining a steady  $\text{O}_2(\text{aq})$  concentration. The target temperature was low enough to allow the use of a water bath, and for practical reasons we used a hot plate with



<sup>8</sup>I found that bubbling  $\text{O}_2(\text{g})$  directly into the electrolyte solution was better to reach and maintain saturation  $[\text{O}_2(\text{aq})]$ , but only if it could be done without the bubbles disturbing the electrolyte solution near either the WE or RE. The alternative was to maintain  $\text{O}_2$  overpressure in the headspace, which required the gas flow to be higher than the leak-rate out of the headspace, and that the electrolyte solution was given enough time prior to deposition to become saturated with  $\text{O}_2$ .

## 2. Synthesis and preparation

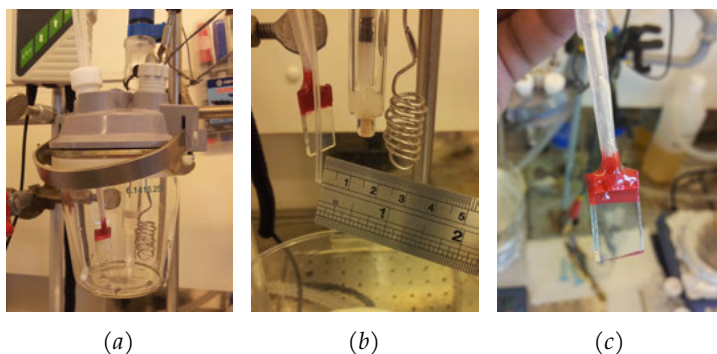



Figure 2.2. Secondary electrodeposition setup. (a) Cell with mounted electrodes and no electrolyte solution. (b) The WE–CE distance was about 25 mm. (c) A fully insulated contact covered with red nail varnish (pre-deposition).

a built-in magnetic stirrer which meant that evaporation of the water bath itself needed to be counter-acted since depositions were 1.5 h long. For that purpose I developed a custom-made cover made with small peripheral holes to allow the temperature probe access to the bath and a large centre-hole for placing the deposition cell securely (to avoid it bobbing in the water). The cover was successful in limiting evaporation and kept the water bath's level constant for over 1.5 h at 80 °C. We also improved on the gas inlet by adapting a long glass pipette for the purpose (instead of a typical gas needle which is metallic and interfered with the current inside the cell).

To improve reliability and repeatability of the electrochemical depositions I created a simple paper-based form to jot down the deposition parameters for each run (since the potentiostats' software unfortunately offered no way to save such metadata). These simple templates  also allowed us to record non-potentiostat parameters such as gas flow rate, stirring or not, temperature, etc..

The secondary electrodeposition setup (see figure 2.2) used a larger-volume cell, and was used for some projects after the completion of **PAPER I**. Due to the shallower angle of the WE in this cell (compared to the perfectly vertical configuration in the primary setup) it was necessary to immerse the entire WE in the electrolyte solution and thus to fully insulated its electrical contacting. The longer distances from the cell ports to the electrolyte solution also necessitated the use of a larger RE and CE (coiled Pt wire). The larger cell also meant a longer WE–CE distance  $\approx 25$  mm (about twice as long as in the primary setup).

The fully insulated contact was sturdy and created in the following way: the electrical wire was passed through a disposable plastic pipette (with its bulbous part cut off) and contacted to the TCO surface with electrically conductive silver lacquer, then covered with a strip of aluminium tape. The tape and the end of the plastic pipette were then fixed into place by colourless epoxy glue to add sturdiness and chemical stability to the contact, and the whole contact was then covered with a thin coat of nail varnish (figure 2.2c). The nail varnish was

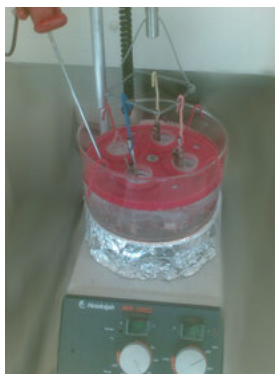


Figure 2.3. CdS chemical bath setup with four simultaneous deposition cells in a temperature-controlled water bath inside the fume hood.

applied primarily to define the active surface area, and for purposes of easier identification since we had several available colours.

## 2.2 Chemical bath deposition of CdS films

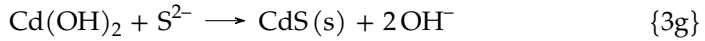
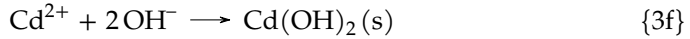
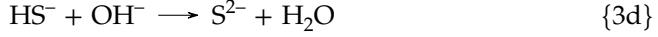
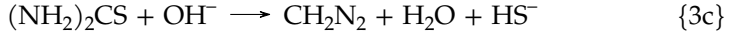
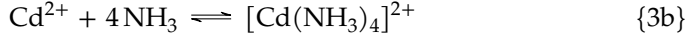
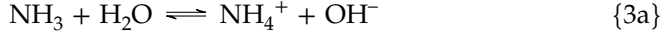
CdS nanoparticles were chemical bath-deposited onto 1.5 h electrodeposited ZnO NRs arrays. An aqueous bath solution of  $\text{CdSO}_4$  **3** (2 mM),  $\text{CH}_4\text{N}_2\text{S}$  **5** (10 mM), and  $\text{NH}_3$  **6** (1 M) was thermostatically maintained at 60 °C before immersing the substrate for a set amount of time (up to 2 h). The substrate was always suspended vertically, and the solution was continuously stirred during the deposition. To prepare the deposition bath (per above), I started by dissolving  $\text{CdSO}_4 \cdot 8/3 \text{H}_2\text{O}$  **4** (1.2365 g) in  $\text{NH}_3$  **6** (12.8 M) to  $[\text{Cd}^{2+}] = 24 \text{ mM}$  then volumetrically diluted it by a factor of eight to  $\text{CdSO}_4$  **3** (3 mM solution in 12.8 M  $\text{NH}_3$  (aq)). The cadmium sulfate salt was sourced from Merck (3  $\text{CdSO}_4 \cdot 8 \text{H}_2\text{O}$ , *pro analysi*). Next I dissolved  $\text{CH}_4\text{N}_2\text{S}$  **5** (0.2284 g) in 100 mL  $\text{H}_2\text{O}$  for a concentration of 30 mM. The thiourea powder was sourced from Merck, *for synthesis*.

For a chemical bath deposition (CBD), first 5 mL of **5** was added to each deposition bath (c.f. figure 2.3) and allowed to reach thermal equilibrium at the set temperature (at least 15 min 60 °C). Simultaneously, a container with **3** was also heated. The substrates were lowered into each of the four deposition baths, and 10 mL of **3** was then added to each to start the CBD reaction. The point of adding the Cd-precursor at the last moment was to avoid unnecessarily subjecting the ZnO/ $\text{Fe}_2\text{O}_3$  substrate to the strongly alkaline solution. After the deposition was completed, the back of the glass substrate was cleaned with a cotton swab soaked in  $\approx 0.75 \text{ mM}$  HCl, then both sides were rinsed with deionized water and blow-dried with  $\text{N}_2$ .

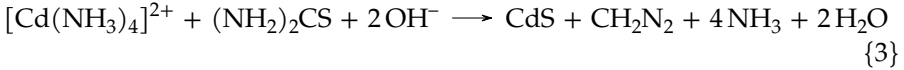
The earliest report [106] of chemical bath deposition of CdS from an alkaline solution with an ammonium salt at room temperature produced thick films in the cubic structure. Later work [107, 108] found that the thickness of the deposit *decreased* with bath temperature.

## 2. Synthesis and preparation

The CdS deposition proceeds along the following steps (most mechanistic studies of CBD of CdS have proposed the so called *ion-by-ion* mechanism, which is what we present here) [109, 110]:



usually described with the following overall reaction



Ammonia dissolved in water produces a hydroxide ion (reaction {3a}) and forms a cadmium tetramine complex (reaction {3b}) which is responsible for slowing the release of solvated  $\text{Cd}^{2+}$  ions. Sulfide ions are released (reaction {3d}) by the hydrolysis of thiourea in alkaline solution (reaction {3c}) [109, 111]. When the product of  $[\text{Cd}^{2+}]$  and  $[\text{S}^{2-}]$  exceed the solubility product<sup>9</sup> of CdS it precipitates (reaction {3e}) either homogeneously in the solution (forming colloids) [113] or heterogeneously at the substrate surface [114], leading to a film. Note that formation of the hydroxide is not desired, but may still occur (which is why it is included in the schema), but if it does occur the likelihood of sulfide substituting for the hydroxide and forming the desired sulfide is very high due to the much higher  $K_{\text{sp}}$  ( $2 \times 10^{-14}$ ) of  $\text{Cd}(\text{OH})_2$ .

## 2.3 Atomic layer deposition of iron oxide

After having successfully coated electrodeposited ZnO NRs with CdS and achieved the intended effect of sensitizing ZnO to visible light, we considered other conformal coatings that could alleviate two of the main drawbacks with CdS, viz., the alkaline conditions during its deposition, and the toxicity of the  $\text{Cd}^{2+}$  ion.

Hewing to the principle of simplicity we established earlier, and considering our alternatives, we landed on the abundant  $\alpha\text{-Fe}_2\text{O}_3$  (hematite), i.e., the principal component of rust. The iron oxides and iron oxide hydroxides (see table 3.2) have a particularly well-studied chemistry, which is no wonder considering their immense economic importance. As the most thermodynamically stable iron

<sup>9</sup>The  $K_{\text{sp}}$  of CdS has variously been reported in literature as  $10^{-25}$  [111],  $10^{-28}$  [109],  $7.1 \times 10^{-28}$  [112], and  $1.4 \times 10^{-29}$  [107].



### 2.3 Atomic layer deposition of iron oxide

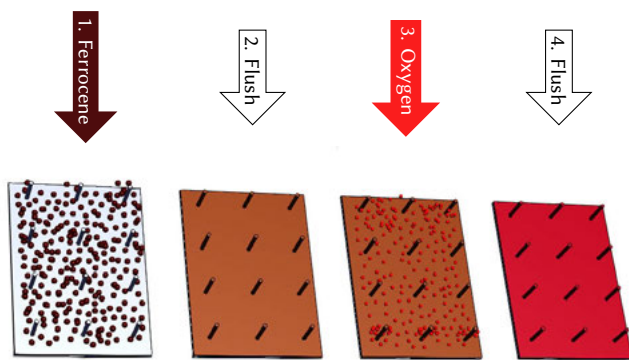


Figure 2.4. ALD is a gas-phase deposition process, where each cycle produces a single atomic layer of  $\text{Fe}_2\text{O}_3$ . In the first step, ferrocene gas is introduced into the reaction chamber, chemisorbing to terminating hydroxyls on the ZnO NR surfaces. The reaction chamber is then flushed with an inert gas, and then the last reactant,  $\text{O}_2$  (g), is introduced, reacting with the chemisorbed iron ions to form an atomic layer of  $\text{Fe}_2\text{O}_3$ .

oxide phase at STP, hematite is the end product of all steel corrosion, and has as such been studied in detail.  $\alpha\text{-Fe}_2\text{O}_3$  has a band gap of  $E_g = 2.2$  eV (564 nm), i.e., well into the visible range, and is also non-toxic, resistant to chemical corrosion in both dark and illuminated conditions, and its VBE is suitable for oxygen evolution from  $\text{H}_2\text{O}$  (c.f. figure 1.3). The main drawbacks with hematite is its indirect band gap and its short intrinsic hole diffusion length (typically 2 nm to 4 nm [115], but up to 20 nm when considering the effect of the electrolyte and band bending [8]), which was one of our main motivations behind minimizing the thickness of the hematite (Hm) layer and the reason for using ALD.

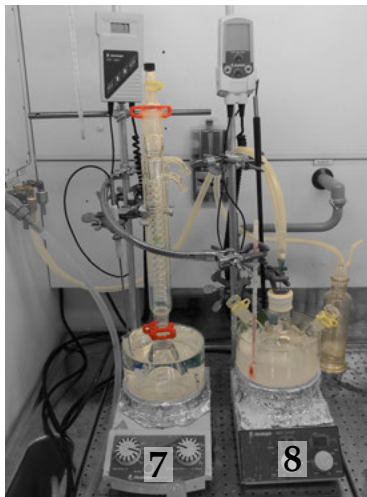
By utilizing self-limiting surface reactions, ALD can evenly deposit thin films on a substrate of arbitrary shape and form. The primary restriction is that the substrate needs to be thermostable, which was not a problem for our samples, being essentially oxide on glass. ALD is a slow deposition method, but no other technique at our disposal could deposit a perfectly even layer of material on a relatively rough substrate (such as our ZnO nanorod samples), in particular not without etching the amphoteric ZnO layer during its deposition.

Binary compounds (such as  $\alpha\text{-Fe}_2\text{O}_3$ ) are usually deposited in four steps for each atomic layer (called a *cycle*, c.f. figure 2.4). The first step contains the metal precursor, in this case ferrocene, which is transported in the gas phase by a carrier gas to the deposition chamber which was kept at 450 °C. The precursor is chemisorbed to the surface of the substrate forming one monolayer. In the second step the carrier gas is flushed to rinse off any excess precursor from the first step. The third step introduces the second precursor, which react with the already chemisorbed molecules on the surface, ideally forming one atomic layer of the desired phase. The fourth step is another flushing operation. Our ALD process was based on previous work by Fondell *et al.* [116, 117] and varied the number of cycles in a series: 35, 50, 62, 75, 87 and 100, ideally corresponding to a

## 2. Synthesis and preparation

**Table 2.1.** Molar masses, amounts and concentrations of the precursors.

	$M/\text{g mol}^{-1}$	$n/\text{mmol}$	$V/\text{mL}$	$m/\text{g}$	$C/\text{mol L}^{-1}$
<b>7</b> $\text{Zn}(\text{OAc})_2 \cdot 2 \text{H}_2\text{O}$	219.50	5.0	50	1.0975	0.10
<b>8</b> $\text{LiOH} \cdot \text{H}_2\text{O}$	41.96	7.0	50	0.2937	0.14



*Figure 2.5.* Our setup for the synthesis of ZnO QDs, allowing the simultaneous synthesis of the two precursor solutions. On the left, boiling  $\text{Zn}(\text{OAc})_2 \cdot 2 \text{H}_2\text{O}$  **7** (0.10 M solution in EtOH) under open atmosphere with water-cooled refluxer, and on the right  $\text{LiOH} \cdot \text{H}_2\text{O}$  **8** (0.14 M solution in EtOH) dissolved at 45 °C in a sealed reactor under  $\text{N}_2$  (g) over-pressure. The glassware and gas flow components have been artificially highlighted in the photo.

hematite layer thickness of 2 nm to 20 nm. Reaction conditions were optimized for hematite formation.

The ALD instrument was a Picosun 8482 R series reactor from the Finnish Sun Oy company.

## 2.4 ZnO quantum dot synthesis

Low-dimensional ZnO (wurtzite) NPs were synthesized as a colloidal<sup>10</sup> solution in EtOH, by adapting a synthetic route first described by Spanhel and Anderson [118] and also by [119, 120], and later improved by Meulenkamp [121]. The synthesis was a batch method involving two precursor solutions prepared at room temperature (for amounts, masses and concentrations see table 2.1).

In the first precursor solution zinc acetate dihydrate,  $\text{Zn}(\text{OAc})_2 \cdot 2 \text{H}_2\text{O}$  **7** (99.5 %), Fluka, was dissolved in EtOH. In the second precursor solution lithium hydroxide monohydrate,  $\text{LiOH} \cdot \text{H}_2\text{O}$  **8** (99 %), Sigma-Aldrich, was dissolved in EtOH. Note that **8** may have contained up to 1 % of  $\text{Li}_2\text{CO}_3$  (as specified on the bottle). This can cause some challenges during QD synthesis, which we will expand on later.

Preparation of precursor solutions was as follows:

<sup>10</sup>A solution that scatters light is a *suspension*. A *colloidal* solution does not. Our prepared ZnO solutions were colloidal, but gradually turned into suspensions after weeks or months of storage.

- add approximately 45 mL EtOH to the Zn-reactor (100 mL Erlenmeyer flask) and a magnetic stirrer bar; set temperature of water bath to boiling point of EtOH,
- turn on  $\text{N}_2$  (g) flow into the empty Li-reactor (round bottom flask) for a few minutes to purge  $\text{CO}_2$  (g) from it; add a magnetic stirrer bar; set temperature of water bath to 45 °C,
- quantitatively transfer the weighed mass of  $\text{Zn}(\text{OAc})_2 \cdot 2 \text{H}_2\text{O}$  **7** to the boiling EtOH,
- add approximately 50 mL EtOH and quantitatively transfer the weighed mass of  $\text{LiOH} \cdot \text{H}_2\text{O}$  **8** to the round-bottom flask,
- once the mixtures have dissolved and the solutions are transparent and colourless move both reactors to an ice bath,
- quantitatively mix the two precursor solutions to 100 mL (fill to the mark with EtOH as needed). Stir. Note the time ( $t = 0$  min for QD growth).

Both salts were easy to handle, weigh up and transfer. The zinc acetate **7** dissolved easily after a few minutes stirring in boiling EtOH **9**. But this solution was not stable for long: after a few hours it formed a milk-white suspension.

The lithium hydroxide **8** has a more challenging chemistry, primarily due to its carbonate salt. Whereas both the dry and the slaked hydroxide have moderate solubility in  $\text{H}_2\text{O}$  and EtOH, with increasing solubility with increasing temperature, the lithium carbonate, on the other hand, has poor solubility in  $\text{H}_2\text{O}$  and EtOH, and its solubility *decreases* with increasing temperature.<sup>11</sup> In practice, this meant that during dissolution of  $\text{LiOH} \cdot \text{H}_2\text{O}$  **8** (0.14 M solution in EtOH) we needed to take care to limit the competing dissolution reaction of  $\text{Li}_2\text{CO}_3$ , which was driven by the presence of dissolved  $\text{CO}_2$ . Since the hydroxide is only moderately soluble to start with, we needed to use as large a volume of solvent as possible. To avoid encouraging the formation of the carbonate,  $\text{CO}_2$  (g) should be kept out of the headspace, and in addition one should avoid heating the solution (definitely not boil it) so as not decrease the solubility of any lithium carbonate that may form. In short, the higher the temperature and the higher the flow rate of  $\text{N}_2$  (g), the more lithium ions were lost as insoluble carbonate, and the more solvent was lost to evaporation, which were both detrimental to our process.

For the same reason, the lithium hydroxide solution **8** must be stirred only gently. Even moderate stirring will draw in more air (which even under  $\text{N}_2$  (g) flow may contain  $\text{CO}_2$  (g)) into the solution, making it easier to form  $\text{Li}_2\text{CO}_3$ . This reaction also neutralizes at least one hydroxide ion, thus decreasing the precursor solution's apparent pH. Of course, strictly speaking pH is not defined in a non-aqueous solvent, but we may still use it as a proxy to discuss the changing chemistry of EtOH as air (containing  $\text{CO}_2$ ) equilibrates with it. To investigate this, I measured the proton activity (apparent pH) of EtOH of two

<sup>11</sup>The solubility of  $\text{Li}_2\text{CO}_3$  in water is 1.54 g at 0 °C, and 1.33 g at 25 °C [122]. This points to an entropy effect, i.e., the solvation of  $\text{Li}^+$  and  $\text{CO}_3^{2-}$  in water decreases the overall entropy of the solution.

## 2. Synthesis and preparation

different purities using a regular pH-meter, and found pH 8.35 (99.5 %) and pH 8.19 (99.96 %) immediately after opening the factory-sealed bottle; and pH 7.83 and pH 7.40 after aerating the samples overnight. These observations suggest that equilibration with air, just like for  $\text{H}_2\text{O}$ , significantly alter the carbonate chemistry of the solvent, which may influence the QD synthesis, and that varying trace amounts of  $\text{H}_2\text{O}$  in EtOH were likely not decisive. All ZnO QD in this work were synthesized using EtOH for reasons of cost, and used more or less immediately after opening the bottle.<sup>12</sup>

To prepare precursor solutions at precisely the intended concentration it is important to maintain the desired solvent volume, which was challenging since EtOH evaporated so readily, especially when boiling. Instead of sealing the glassware (which changes the boiling point of the solvent) we fitted the Li-reactor with a water-cooled reflux tube which successfully captured and returned effectively all the evaporated solvent.

---

<sup>12</sup>With the benefit of hindsight, I should perhaps have let the EtOH solvent aerate fully (until the pH settled) before preparing the precursors. This did not effect the quality of individual batches, but may have improved repeatability between batches.

### 3. Characterization methods

#### 3.1 UV-Vis spectroscopy

An object under irradiation can interact with the light in various ways. From an optical perspective, the incident light has to penetrate the surface of the object to interact with the material in the bulk of the object. And then the light has to penetrate another surface to exit the object [123, p. 71].

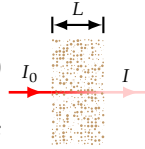
For light incident on an object, the light may (a) be transmitted through the object (in a well-defined direction), (b) be diffusely scattered at the object interfaces or in its interior, (c) be specularly reflected, or (d) be absorbed at the object interfaces or in its interior. If we posit that these processes are the only interactions that can occur between the incident light and the object, then conservation of energy requires:

$$T + R + S + A = 1 \quad (3.1)$$

where  $T$  is the transmittance,  $R$  is the specular reflectance,  $S$  is the diffuse scattering, and  $A$  is the absorbance.

The transmittance is also related to the absorption coefficient and the path length,  $L$  in the familiar Beer-Lambert law (also illustrated in the margin):

$$T \equiv \frac{I}{I_0} = \exp(-\alpha L) \quad (3.2)$$



In most of my work, we were mainly interested in the optical absorption. If scattering can be neglected, eq. (3.1) simplifies to

$$A = 1 - T - R \quad (3.3)$$

or in terms of incident and transmitted light

$$A = \log\left(\frac{I_0}{I}\right) = -\log(T) \quad (3.4)$$

In practice, absorbance,  $A$  is the base-10 logarithm of the spectral radiant power transmitted through a reference sample divided by that transmitted through the investigated sample, both observed in identical cells.

Note that *absorbance*, defined as  $-\log(1 - \frac{I_{\text{abs}}}{I_0})$  [5] is sometimes used in lieu of  $A$  for samples where scattering is not negligible, is algebraically equivalent to  $A$ , since  $I_{\text{abs}} = I_0 - I$ , and thus the expression above can be rearranged to  $\log\left(\frac{I_0}{I}\right)$ .

### 3. Characterization methods

The absorbance can thus be determined by measuring both the transmittance and the reflectance of a sample. Or, if reflectance can be neglected, then simply by measuring its transmittance.

For a thin film, the amplitude and intensity of reflected or transmitted beams of light can in principle be determined by setting up Maxwell's equations and applying the appropriate boundary conditions [124]. In practice that is very cumbersome and not something often done. More to the point, for a thin film the absorbance equals the absorption coefficient times the film thickness,  $d$ :  $A = \alpha d$ . The absorption coefficient of a thin film can be expressed in terms of the reflectance and transmittance [125]:

$$\alpha = \frac{1}{d} \ln \left( \frac{1 - R}{T} \right). \quad (3.5)$$

And if the thickness,  $d$ , is not known, simply rearrange the equation so the left-hand side gives you  $\alpha d = A$ .

We have employed ultraviolet–visible–near-infrared (UV-Vis-NIR) spectroscopy extensively, and with a few different instruments. For *in situ* experiments on films or colloidal suspensions I used an OceanOptics HR2000+ high-resolution fibre-optic spectrometer, with a Mikropack DH-2000-BAL UV-Vis-NIR light source using both a deuterium lamp and a halogen lamp. This setup was controlled via a computer running SpectraSuite on Microsoft Windows XP. *Ex situ* experiments on films were measured on the venerable PerkinElmer Lambda 900 UV-Vis-NIR spectrophotometer equipped with an integrating sphere (e.g., **PAPER I**, figure 6.1c).

UV-Vis-NIR spectroscopy gave us optical transmittance, reflectance, and/or absorbance for both thin film and colloidal samples, which allowed me to track semiconductor band edges and dye absorption peaks, among other features.

## 3.2 Photoluminescence spectroscopy

In photoluminescence (PL) spectroscopy the sample is excited with photons with higher energy than its band gap and the sample's emission spectrum is recorded [126], i.e., photons in and photons out. I have used photoluminescence (PL) to study surface or interface phenomena involving the absorption of photons that generate electron-hole pairs, which is of central importance in PC [127].

In ultraviolet–visible (UV-Vis) fluorospectrometry (also known as photoluminescence (PL) spectrometry) the sample under study is placed in front of a light source with a suitable bandpass filter between them so that only a particular wavelength in the UV-Vis region illuminates the sample. Since the sample's emission can be assumed to be isotropic, the direction of excitation was set at an angle to the detector to avoid detecting the incident light. Special care was taken to keep stray light out of the spectrometer (the room was darkened and the instrument was covered).

I recorded fluorescence spectra of electrodeposited ZnO NRs on TCO-glass with and without CBD CdS. Room-temperature steady-state emission spectra were recorded on a Fluorolog 3<sup>1</sup> (Horiba Jobin Yvon) equipped with double-grating excitation and emission monochromators and a 450 W Xe-lamp. The main sample series (CdS-coated ZnO NRs on TCO-glass) was measured using right-angle (RA) detection with the sample substrate at 30° and always with the EE (electrode–electrolyte) surface facing the incident beam, in order to minimize inner-filter effects. The excitation and emission slits were set to obtain 2 nm, 3 nm and 6 nm and 4 nm, 6 nm and 8 nm band passes, respectively (depending on excitation wavelength). Integration time was set to 0.1 s per point. A 400 nm long-pass filter was placed *after* the sample to reduce second-order diffraction by the excitation monochromator (for  $\lambda_{\text{exc}} = 350 \text{ nm}$  and 375 nm). The emission spectra were corrected for the spectral sensitivity of the detection system by using a calibration file of the detector response.

### 3.3 Raman spectroscopy

As we previously discussed (section 3.1), light interacts with matter in a variety of ways. When incident light is scattered by an object, it is overwhelmingly likely to be *elastically* scattered, meaning the light is propagated without changing its wavelength (or equivalently, its energy or frequency). With Raman spectroscopy we measure the *inelastic* spectrum scattered from the sample under illumination by laser light (high-power density, coherent, monochromatic, collimated light). In this process the vast majority of the incident laser light is scattered *elastically* (Rayleigh scattering), and only about one inelastic scattering event occurs for every  $10^7$  elastic scattering events (0.1 ppm). The inelastically scattered light has a very slightly different wavelength than the incident light, because it has exchanged vibrational (or rotational) quanta with the specimen, which can only occur if the polarizability of the specimen's electron cloud is changing during the vibration [128], and thus carries with it information on the vibrational state of the specimen which is correlated to its chemical bonding, chemical composition, and phases in crystalline materials.

For some crystal structures, Raman and infrared (IR) are complementary, in the sense that the crystal's vibrational modes are either Raman *or* IR active. A lattice vibration can be simultaneously Raman and IR-active only in non-centrosymmetric crystal structures (e.g., polar crystals such as ZnO, c.f. table 3.2). All molecules and solids have vibrational spectra, and nearly all vibrations are either Raman or IR active [129].

Inelastic scattering of light by matter was first theorized by Smekal [130] and shortly after by Kramers [131, 132] and Kramers and Heisenberg [133]. This

<sup>1</sup>The Fluorolog 3's control software was based on the Origin Pro software suite, with all recorded data saved as Origin plots by default. Not very convenient if you are not an Origin user. Using Origin's built-in command prompt, the data could be exported to ASCII in a two-liner: `fdlog.openpath(); {doc -e W {save -w %H %B%H.txt}}`.

### 3. Characterization methods

was around the same time as Venkata Raman was pondering the molecular diffraction of deep bodies of seawater during a voyage across the Indian Ocean [134], which led him and Krishnan to experimentally describe the Raman effect a few years later [135, 136]. The Raman effect was also independently described experimentally in the USSR by Landsberg & Mandelstam [137, 138]. The earliest investigations of the Raman effect in semiconductors occurred after the advent of the laser in the 1960s [139].

The terminology we use to assign vibrational spectral modes was determined by an ICSU Joint Commission for Spectroscopy in 1953 [5] but is commonly referred to as Mulliken [140–142] notation.

In this thesis we concern ourselves with the Raman effect in crystalline semiconductors. Semiconductors always have more than one atom in their unit cell, which leads the dispersion relations (the relationship between frequency and wave vector) to always exhibit two kinds of phonons with which photons can interact, viz., the *optical* and *acoustic* modes of lattice vibration. The interaction with optical phonons<sup>2</sup> is what typically generates Raman scattering, and the interaction with acoustic phonons results in so called Brillouin scattering (first predicted by Brillouin [143] in 1922) [144]. Both optical and acoustic phonons have longitudinal and transverse modes, depending on whether the vibration is along the direction of propagation or orthogonal to it.

An incident photon of a certain wavelength can give or gain some of its energy to the lattice in the form of a phonon. The precise amount of energy gained or lost by the lattice is compensated by an increase (Stokes) or decrease (anti-Stokes) in the wavelength (energy) of the scattered light [144, 145]. A phonon is a many-body-type quasiparticle;<sup>3</sup> a quantized lattice vibration and describes a collective motion of atoms in the lattice. Phonons play an important role in determining a material's thermal, optoelectronic, and electrical transport characteristics [146]. At  $T = 0\text{ K}$ , a crystal lattice would contain no phonons. At any temperature above absolute zero all matter vibrates to some extent, due to lattice vibrations being quantized. A material's phonon structure is fundamentally related to its thermodynamic properties.

Another way to look at this interaction is that the incident photon excites a phonon, causing the semiconductor to re-emit the remaining (or gained) energy as a photon. This scattering process is generally isotropic, which is why Raman scattering is commonly measured in the antiparallel direction to the incident beam. Also, both the incident and emitted light typically have limited penetration depth in the sample, which also restricts detection to the reflection

---

<sup>2</sup>They are called *optical* phonons because they can be excited by electromagnetic radiation in the optical wavelength region.

<sup>3</sup>Some other commonly encountered quasiparticles are **polaritons** (coupled photon–optical phonon modes), **excitons** (an electron–hole pair), **polarons** (coupled electron–phonon modes), **plasmons** (a collective excitation of all the electrons in the crystal, i.e., a quantum of plasma oscillation), **magnons** (a collective spin excitation of the lattice), and **trions** (a localized excitation of two holes and one electron or two electrons and one hole that may occur in optically excited semiconductor nanostructures).



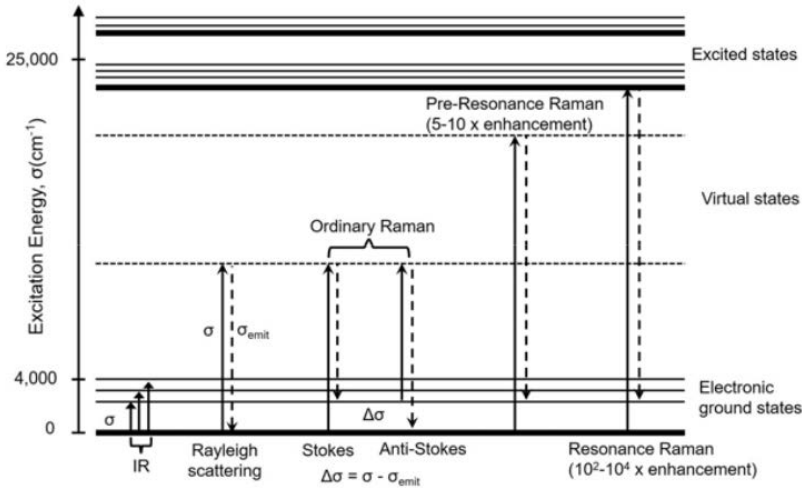


Figure 3.1. Rayleigh, IR, and Raman (Stokes, anti-Stokes, and resonance) scattering. Resonance Raman scattering occurs when the excitation energy coincides with an electronic transition (such as the band gap) in the material. Illustration courtesy of Qiu [147].

direction (just like for scanning electron microscopy (SEM) and many other techniques with opaque samples).

The created phonon can in turn interact with the lattice to produce a second phonon (of lower energy than the first), and this cascade process can be repeated, generating what is called second-, third-, fourth-order (and so on) Raman scattering, or more generally termed *multiphonon* scattering. Note that if the energy of the phonon coincides with the energy of an exciton (*resonance*), the intensity of the higher-order phonon can be strongly enhanced [144].

In polar semiconductors, i.e., materials with a permanent electric polarization due to the relative displacement of positive and negative ions in the crystal structure (in other words, ionic crystals), with few defects interaction between this polar electric field and the optical phonons is expected to be the dominant scattering mechanism at RT. This so called polar-optical-phonon scattering interacts with the charge carriers in what is known as the Fröhlich interaction [148, p. 40].

This interaction of optical phonons and charge carriers in polar semiconductors in many cases determines its carrier mobility [148] “The carrier mobility in the presence of an external electric field is determined predominantly by the rate at which the electrons emit optical phonons” [148].

Raman spectroscopy is non-destructive, simple, and often (but not always) a quick method to determine which crystal phases are present in a solid or solute sample. It yields information about bonds and crystallinity, and we can use it to tell apart different polymorphs of the same composition (e.g., hematite from maghemite) which is not always straight-forward with X-ray diffractometry (XRD). One of the major weaknesses of Raman spectroscopy is fluorescence

### 3. Characterization methods

from a sample, which can completely swamp the inelastically scattered signal and be very hard to overcome.

#### 3.3.1 Resonant Raman scattering

As we have seen, regular phonon scattering (i.e., non-resonant) occurs through excitation to virtual intermediate electronic transitions. In this section we will briefly describe *resonant* Raman scattering by optical phonons as utilized in **PAPER IV**.

When the wavelength (i.e., energy or frequency) of the incident light approaches one of the electronic transitions of the crystal (such as the band gap in a semiconductor), the Raman scattering can be enhanced by many orders of magnitude (this effect was first reported in crystals by Ovander [149]). Achieving resonance used to be hard because the wavelength of the incident laser light must be close to the band gap under study, and it is only with the development of high-power UV laser sources that wide gap semiconductors such as ZnO came within reach of resonance studies. But even with the intensity gained from resonance, resonant Raman experiments may be saddled with an even stronger phonon-aided luminescence that can drown out all or some of the Raman modes, which is a drawback particularly affecting samples with any organic residues (even very small amounts).

Under electronically exciting conditions (i.e., resonance) Raman can provide information on vibrations in the excited state and can also give clues towards the charge separation/transfer mechanisms in the material [128]. Polar crystals often complicate resonance by leading to the introduction of multiphonon processes caused by intraband Fröhlich interaction [150].

A challenge when using resonant Raman for wide gap materials is the need to utilize UV light, which puts added constraints on the optical components in the Raman spectrometer, which is why we used a near-UV objective and UV lenses in the spectrometer's optical path. All measurements were recorded at ambient conditions. Resonant Raman was measured with the 325 nm excitation line of a He-Cd laser, using a 15x/0.30 NUV objective lens (Thorlabs). The detector was calibrated against the  $1332\text{ cm}^{-1}$  line of diamond. All measurements in the resonant experiment series used the exact same acquisition parameters. Cosmic rays were removed either by the detection and removal algorithm built-in to the Renishaw software suite, or manually at a later stage by linear interpolation over the affected data points. Peak and baseline fitting was performed with the algorithm by Davies et al. [151] (also see section 4.1).

### 3.4 Photocatalysis

In order to evaluate the photocatalytic or photoelectrochemical properties of the catalysts we synthesized, we employed both solar simulators (emulating the standard air mass 1.5 global (AM1.5G) spectrum to varying degrees of



Figure 3.2. Photo by the author of a particularly organised series of Raman measurements on ZnO powder samples (**PAPER IV**), showing the objective lens mount of the Ramanoscope and its sample tray. The inset shows a close-up of the transparent sample wells on the tray.

fidelity) and custom or off-the-shelf lamps. I designed and built many of the experimental setups from scratch.

### 3.4.1 The solar spectrum

To get a firm grasp of the solar spectrum it helps to first understand the black body spectrum and the concept of air mass (AM).

The spectral radiance of an ideal black body<sup>4</sup> is given by Planck's law<sup>5</sup> [36, sec. 2.3]

$$I_{(\lambda,T)} = \frac{2\pi hc^2}{\lambda^5} \frac{1}{\exp\left(\frac{hc}{\lambda kT}\right) - 1} \quad (3.6)$$

This represents the emitted power per unit area of emitting surface and per unit wavelength.  $I_{(\lambda,T)}$  is called the spectral radiance, and when referring

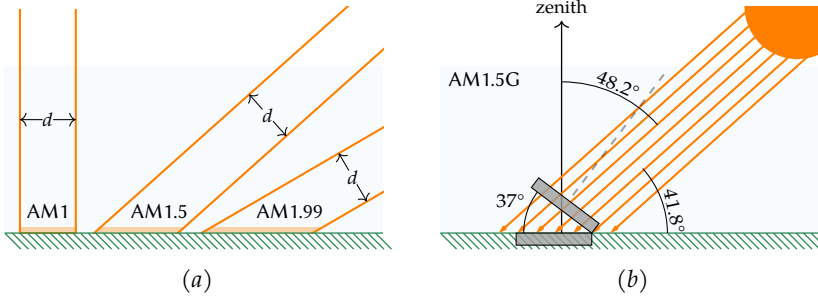
<sup>4</sup>Every object at above 0 K emits and absorbs electromagnetic radiation to some degree. An object that absorbs all radiation is a black body and by definition has an emissivity of unity. For a black body the spectral distribution of this radiation depends *only* on the object's absolute temperature.

<sup>5</sup>By the year 1900, physicists had been trying to understand the dependence of the black body spectrum as a function of temperature and wavelength for almost half a century. Several proposed equations existed, but as they were within the confines of classical physics they all failed to match observations at higher frequencies. As the story is commonly told, in an act of desperation (Planck feared being scooped) he submitted an equation that seemingly worked but made use of Boltzmann's entropy law which rested on the assumption of atoms (quanta) and was statistical, both phenomena disliked by Planck who was a conservative physicist.

### 3. Characterization methods

**Table 3.1.** Physical quantities related to Planck’s law eq. (3.6) and the calculation of the solar spectrum. For sources please see **CONTRIB. 8**.

Name	Symbol	Value	Unit
Speed of light	$c$	$2.997\,925 \times 10^8$	$\text{m s}^{-1}$
Elementary charge	$e$	$1.602\,177 \times 10^{-19}$	C
Planck’s constant	$h$	$6.626\,070 \times 10^{-34}$	J s
Planck’s constant	$h_{\text{eV}}$	$4.135\,668 \times 10^{-15}$	eV s
Boltzmann’s constant	$k$	$1.380\,649 \times 10^{-23}$	$\text{J K}^{-1}$
Temperature of the Sun	$T_{\text{Sun}}$	$5.772\,000 \times 10^3$	K
Astronomical unit	$R_{\text{AU}}$	$1.495\,979 \times 10^{11}$	m



**Figure 3.3.** Illustration of the air mass concept. (a) Demonstrating the geometric projection effect of different air mass values. As the air mass increases, the projected area on the ground of an identical beam of light increases (diameter  $d$  is the same for all cases). AM1.99 corresponds to Uppsala’s latitude. (b) Geometry of the AM1.5G standard, here shown with a light beam incident also on a horizontal surface, illustrating how the surface tilted  $37^\circ$  collects more light. The *zenith angle* is  $48.2^\circ$  for AM1.5G, which is complementary to the *solar altitude* (angle from the horizon,  $41.8^\circ$ ).

to a black body it is considered independent of viewing angle (isotropic), independent of time, and independent of position on the emitting surface (spatially homogeneous).

By plugging the surface temperature of the Sun (see table 3.1) into eq. (3.6) we can accurately model its radiance and the irradiance on Earth<sup>6</sup> (stars are to a very good approximation black bodies). Once the sunlight enters our atmosphere, though, things become much more messy, and we are better off leaving analytical equations behind and embracing international standards. To understand the standard solar spectrum we need to briefly familiarize ourselves with the AM concept.

The air mass concept (see figure 3.3) offers a compact way to express the influence of atmospheric absorption and scattering (both of which depend on path length in the atmosphere, i.e., air mass) on the terrestrial irradiance for all latitudes except for the highest. Just outside the atmosphere, the air

<sup>6</sup>For an *emitting* surface, the term is **radiance**, and for an *absorbing* surface it is **irradiance**.

mass is zero at all latitudes. On the equator with the sun at zenith, air mass is unity. Assuming zero altitude (sea level) and a homogeneous plane-parallel atmosphere (i.e., one in which density is constant and Earth's curvature is ignored), AM is the secant of the zenith angle in degrees,  $z$ :

CONTRIB. 8

$$\text{AM} = \sec(z) = 1/\cos(z) \quad (3.7)$$

This equation breaks down above  $75^\circ$  latitude, which is a problem for astronomers but perfectly fine for our purposes.<sup>7</sup>

### 3.4.2 Photocatalysis rigs

I designed several rigs for photocatalytic testing over the course of my work. Some were tailored towards thin film evaluation and others towards the evaluation of colloidal photocatalysts, all at room temperature (no active cooling of the PC reactor). Our light sources are described in box 3.1.

#### Box 3.1: Laboratory light sources

To maintain a stable power density on the irradiated sample it is always advisable to allow the light source sufficient time to warm up before starting the measurement, in order for any filament to reach its working temperature, or heat transfer across a sink to reach equilibrium, etc.. If the light is not too bright nor too dim, the evenness of the produced patch can easily be judged simply by looking at it. Evenness can be improved considerably by adding suitable optics in the light path. Light sources are commonly rated by their power draw, but this says nothing about the intensity of the produced light nor its spectral distribution. It is therefore important to measure both the power density of the lamp (which depends on the distance) and its spectral distribution.

In contrast to natural sunlight, we can tailor the spectral output of a lamp to suit a particular application, e.g., a wide gap semiconductor might be put under illumination of a UV lamp. Since light is effectively a reactant in a PC reaction, this can significantly increase its throughput.

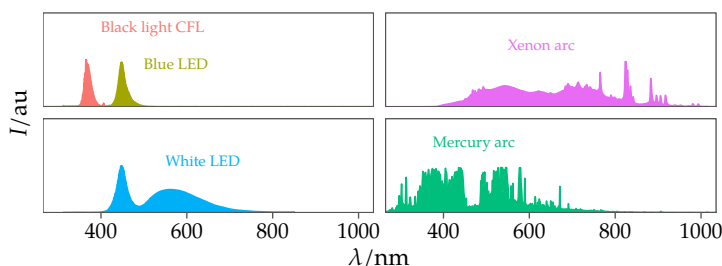


Figure 3.4. Emission spectra of black light compact fluorescent light (CFL) (digitized from manufacturer's datasheet) and a custom-order blue light-emitting diode (LED) array (experimentally recorded), a xenon arc solar simulator lamp (experimentally recorded), typical white LED (digitized from manufacturer's datasheet), and mercury arc lamp (experimentally recorded).

<sup>7</sup>Better models of the atmosphere [152] demonstrate that air mass reaches at most around 38 for astronomical objects towards the horizon ( $z = 90^\circ$ ).

### 3. Characterization methods

Philips PL-S BLB/2P CFL black light with a power draw of 8.6 W and producing 1.65 W UV-A centered at 370 nm and with less than 0.2 % UV-B, according to the manufacturer's datasheet. This kind of lamp has the form-factor of a consumer-grade CFL, is cheap and easy to source but produces very little visible light (hence the name). But because the light source itself is about a decimetre long and half as wide, the power density even very close to the lamp was very low, which made it unsuitable for our PC experiments.

Our blue LED was a custom-made array with 49 surface-mounted blue LEDs with an integrated heatsink and fan (branded "Allray"). Spectral output was centered at 450 nm with FWHM of 20 nm and a power draw of 50 W. We measured power density at the distance of the sample (c.f. figure 3.5b) to 34(4) mW cm<sup>-2</sup>.

The Oriel Instruments Newport 67005 solar simulator used a xenon arc filament and an AM1.5G optical filter to produce 100 mW cm<sup>-2</sup> at the sample (see blog for details [\[153\]](#)).

The bottom-left panel shows a typical white LED emission spectrum, here represented by a Perkin-Elmer ACULED™ with a colour temperature of 6500 K. This spectral distribution is typical for GaN (emitting at 465 nm) and Ce<sup>3+</sup>:YAG (Ce-doped yttrium aluminium garnet) acting as a phosphor emitting a broader Stokes-shifted yellow light. This sort of white light suffers from "blue overshoot" and a "cyan gap", which new materials based on perovskite nanostructures aim to overcome [153].

The high-pressure mercury arc filament can sustain very high intensities (commercially known as a "tanning lamp"). Here showing the emission of a Philips HPA 400S high-pressure mercury lamp (400 W). Apart from broad visible (Vis) emission it also outputs lots of UV-A and heat.

After a few not-so-successful lighting setups involving white-light LEDs and "black light" CFLs (both turned out to be too low-intensity for any experiments), we achieved our first working PC reactor (figure 3.5a) using a high-intensity blue-light LED array. The reactor for this lamp was simply a beaker wherein the sample was placed face-up on a custom-machined acrylic platform so that a magnetic bar could freely spin underneath it and stir the solution. Progress monitoring was done by periodically transferring a sample of the solution to a cuvette for *ex situ* UV-Vis spectrophotometry. This setup was used in **PAPER I**.

We quickly evolved the setup to use a quartz cuvette to allow *in situ* UV-Vis tracking, but with the down-side of no longer being able to stir the solution (see figure 3.5b). We managed to improve the intensity and uniformity of the light from the LED array with the addition of an optical tube (containing a convex lens with adjustable position along its length) and two aspheric condenser lenses (Thorlabs ACL-5040,  $d = 50$  mm,  $f = 40$  mm) to the optical path, producing a dense and even patch of light approximately 2 cm in diameter. We chose to continue mounting the light source vertically because the quartz cuvette only had two transparent sides. This setup was in **PAPER II**, where we also experimented with a mercury arc lamp.

I also performed a number of PC experiments with a mercury arc lamp (as a "poor-man's" solar simulator), which resulted in quite poor photocatalytic degradation, but some interesting morphological changes of our core-shell nanorods reported in **PAPER II**.

With our third and fourth generation of the PC reactor (figures 3.5c and 3.5d) we graduated to using a solar simulator with a xenon arc lamp. The proximate cause for this setup was to have the light impinge directly onto a thin-film photocatalyst that was lying on the bottom of the cuvette (facing up). The ultimate cause was that the quartz cuvette had only two transparent sides,

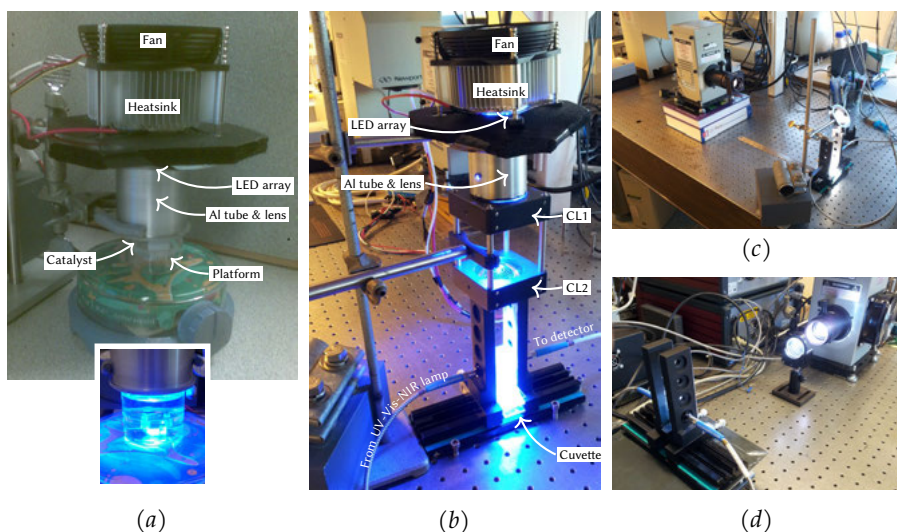
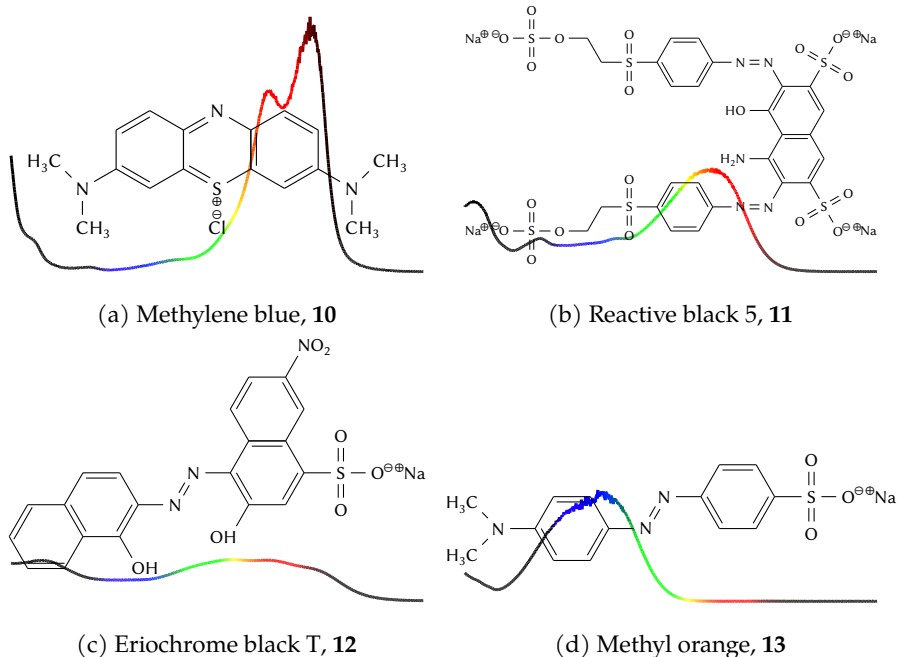


Figure 3.5. Representative depictions of laboratory setups used for photocatalytic evaluation. (a) Illuminating the sample from above using the blue LED array. The inset shows a close-up of the beaker with a sample while illuminated. (b) With the same light source, but better optics and cuvette with *in situ* tracking of optical absorption. (c) This setup represented a sort of evolutionary step (solar similar light source, but keeping the *in situ* UV-Vis tracking and the vertical illumination via mirror above the cuvette), before switching to (d) broadband illumination with solar simulator and AM1.5G filter.

which meant *in situ* spectrophotometry would not have been possible with horizontal illumination. The light from the solar lamp hit a mirror placed at a  $45^\circ$  angle above the cuvette. The dye degradation was tracked *in situ* using our fibre-optic spectrophotometer.

Constructing these PC rigs gave me ample reason to learn more about basic optics like how to collimate visible light with lenses or redirecting beams with mirrors, and the use of optical tables. For the earliest setups an optical tube fitted with a convex lens movable along the tube's length (labelled as "Al tube & lens" in figure 3.5) was the only beam-forming component. As such, I devoted some thought to whether the inside of the tube would reflect the (small) UV emission of the blue LED (which is what we desired). A metallic aluminium surface would be highly UV-reflective, but the question in my mind was how reflective a naturally oxidized aluminium surface would be. Aluminium oxide itself is a quite good UV absorber. But the natural oxide layer should be quite thin. I proceeded under the assumption that UV reflectivity in the tube was sufficient, with consideration given to the fact that the blue LED was expected to produce relatively little sub-400 nm light. In hindsight, a UV reflectance experiment would have settled the matter, but at the time I was young and reckless.

### 3. Characterization methods



Scheme 1. The chemical structures of the evaluated dyes overlaid with a line plot of their experimentally determined absorption coefficient in aqueous solution. Note that although the scales are not shown (for aesthetic reasons), all are plotted using the *same* scales.

#### 3.4.3 Dyes

When evaluating a photocatalyst with regard to its effectiveness to photodegrade a pollutant, we most often want to substitute the actual pollutant for a model compound that (a) is reasonable safe to work with, (b) has chemical properties that as far as possible match the pollutant, (c) and has a distinct absorption band in the UV-Vis-NIR region for easy tracking. As many pollutants of interest are polycyclic aromatic compounds, and aromaticity often produces colour, *dyes*<sup>8</sup> were perhaps an obvious model for photocatalytic degradation.

The source of the colour of all dyes is the electronic transitions of their conjugated ring system. And since they are more-or-less water-soluble, they are also salts (the aromatic part may be cationic or anionic, and the formal charge may be localized or not).

Dyes containing the  $-N=N-$  functional group are called *azo* dyes, which schemes 1b to 1d are examples of. Out of the dyes presented in this thesis (see scheme 1), MB exhibited the least changes to its absorption spectrum on the addition of EtOH (discussed further in section 6.3). Both Eriochrome black T (EBT) and methyl orange (MO) exhibited pronounced changes in their spectrum as well as poor linearity with concentration on addition of EtOH,

<sup>8</sup>Soluble colourants are called *dyes*, and insoluble colourants are called *pigments*.

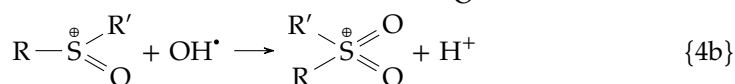
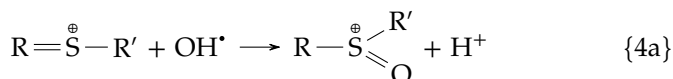


and reactive black 5 (RB5) decolourized completely in less than an hour under illumination in the same conditions.

MB is a cationic dye in the thiazin family of structures, and one of many derivatives of phenothiazine. It has brilliantly strong colour (high absorption coefficient) making it very useful in the dyeing industry [154], and was historically used as an anti-malarial drug (the first such drug actually). Around 40 years ago MB was a popular dye sensitizer in thiazine photogalvanic cells [155] (this was before the discovery of Ru-based DSSCs).

Both dye *degradation* and *decolourization* will lead to a decrease in the optical absorption spectrum, but whereas decolourization (also called *bleaching*) is reversible and leaves the dye molecule conformationally intact, degradation is irreversible and eventually leads to the mineralization of the organic phase (producing water, carbonates, nitrates, sulfates, etc.).

Photocatalytic degradation is the complete breakdown of the bonds in the target molecule by the action of reactive species in solution formed by the photoexcited charges on the photocatalyst's surface. This degradation is commonly thought to proceed first via a two-step attack of photogenerated  $\text{OH}^\bullet$  radicals in solution on the sulfur of the thiazine ring to form sulfoxide then sulfone:



The formed sulfone group on the central ring makes the thiazine ring unstable causing it to cleave leaving two benzenic rings and leading to the total loss of colour. Hydroxyl radicals are expected to be the most potent of the photogenerated reactive oxygen species (ROS), but in principle the step-by-step photodegradation of the dye may proceed via ROS in solution, or via oxidation or reduction of adsorbed dye molecules or fragments. It is perhaps useful to remember that at this point in the reaction, decolourization is total despite the reaction not yet reaching complete mineralization. This is a result of our choice of tracking variable: decolourization will occur as soon as the first bond is broken (roughly requiring 2 holes), but complete mineralization of MB requires 102 holes [155]. Note that once decolourization has occurred, the degradation process can no longer be spectrometrically tracked, and without using other analytical methods (such as mass spectrometry) we cannot know how much time elapses until complete mineralization, only that once the first irreversible degradation step has occurred, mineralization will occur eventually.

The so called *leuco*<sup>9</sup> form of the dye is formed in the reversible reaction



( $E^0 = 0.011\text{ V vs. NHE at pH 7}$ ) that breaks the conjugated bonding and shifts the absorption maximum far into near infrared (NIR), causing *decolourization*

<sup>9</sup>Greek λευκος (leukos) "white", c.f. *leucocyte* (white blood cell).

### 3. Characterization methods

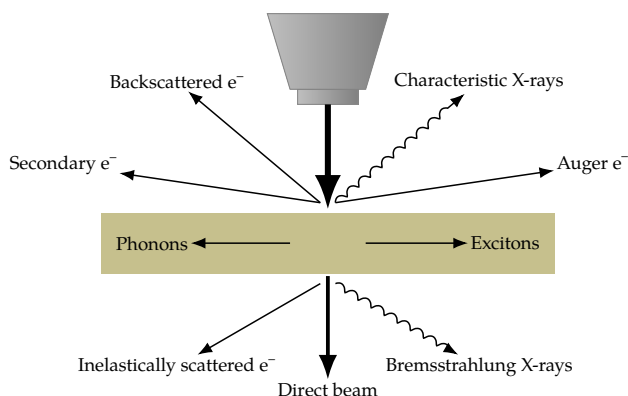


Figure 3.6. Illustration of electron beam interactions with matter.

without degradation. MB may also form the semi-reduced form  $MB^{\bullet-}$  with an absorption maximum at 420 nm, which readily disproportionates into MB and LMB. In addition, MB has a colourless oxidized form,  $MB^{\bullet+}$  which is unstable in alkaline conditions [155].

## 3.5 Electron microscopy

Electron microscopy allows us to resolve features impossible to resolve with visible-light microscopy (VLM). Furthermore, due to the rich interactions between high-energy electrons and matter (see figure 3.6), a host of related techniques can be used to study elemental composition and more.

### 3.5.1 Scanning electron microscopy

I made extensive use of SEM to inspect the electrodeposited ZnO nanoarrays and their different coatings.

Like many other scientific advances, the electron microscope was the result of scientific and technical advances progressing in lockstep. Diffraction with X-rays having been established some two decades earlier, diffraction with electrons soon followed. Louis de Broglie theorized (in 1925) that electrons (and all other matter, for that matter) have wavelike properties, which would give them a very short wavelength, which would mean much higher resolving power than VLMs. Funnily enough, electron optics and the electron microscope were invented in 1932 by Knoll and Ruska [156–158]<sup>10</sup> who had not heard about de Broglie's ideas [159] and embarked on the project because they thought the wavelength limit did not apply to electrons (it does). Within a year, the resolution limit of VLM was surpassed. Commercial production of TEMs began in Germany in

<sup>10</sup>Max Knoll, with a doctorate from the Institute for High Voltage Technology at the University of Berlin, soon after took a job at Telefunken to work in the budding field of television design.

1939, and in many other places after 1945. Despite being commercially available for so long, the electron microscope is still a very expensive piece of equipment, but it has also seen impressive improvements in resolution due to higher beam brightness and ingenious corrections of the spherical and chromatic aberrations that are inherent to electron optics. The first SEM was patented by von Ardenne [160] who managed to *scan* a very small raster with a finely focused electron beam. Compared to TEMs, commercial interest was slower to develop for SEMs and did not take off until the 1960s.

The interactions between the direct beam (also called the incident beam, or *primary electrons*) and the sample (c.f. figure 3.6) can be divided into elastic and inelastic scattering.

Elastic scattering may entail a change in direction of the primary electrons, but no detectable change in energy. They are referred to as backscattered electrons, because it is easier to detect the elastically scattered electrons that happened to deflect *away* from the direct beam than the ones more or less in its path. Back-scattering increases with increasing atomic number  $Z$ , making heavier atoms appear brighter in back-scatter mode. Back-scattered electrons have a large information depth in the sample (they come from deep inside the sample).

Almost all the kinetic energy carried by the direct beam will eventually be dissipated by inelastic scattering events, ending up as heat in the sample. The small proportion of the direct beam ending up as back-scatter, secondary electrons, or X-rays form the whole basis for imaging or analysis. Inelastic scattering can be further subdivided into phonons, plasmons, and inner shell excitations, and so called secondary electrons. Secondary electrons is a somewhat loosely defined term, used to describe any electrons with less than around 50 eV in kinetic energy escaping from the surface of the sample [161]. They are most likely the result of inelastic scattering very close to the sample surface, and their yield (i.e., the number of secondary electrons per primary electron) is often above unity which makes them very useful for SEM imaging. Because of their low kinetic energy, the secondary electron detector is positively charged to attract them. To form the two-dimensional micrograph from the secondary electron signal, it is simply synchronized in time with the scanning of the direct beam over the sample.

I used SEM to record the micro-morphology of our thin film samples deposited via electrochemical deposition (ECD), CBD, or ALD on various types of transparent conducting oxide substrates. As TCO on glass makes for a fairly poor conductor (certainly in terms of dissipating the electron beam without charging up the sample), I always contacted an exposed part of the TCO film with the metallic SEM sample holder. For the same reason I generally avoided electron beam voltages higher than 3 kV.

### 3. Characterization methods

#### 3.5.2 Transmission electron microscopy

In a transmission electron microscope a highly focused beam of electrons is generated either thermionically or by field emission (the latter can produce beams only 1 nm in diameter at the sample). The emitted beam is passed through a series of electromagnetic condenser lenses and objective lenses before hitting the sample, and then a series of projector lenses to form the resulting image.

A TEM specimen is typically no thicker than the mean free path of electrons at the accelerating voltage of the beam, or more precisely we could say that the likelihood of a single scattering event to occur while passing through the specimen is 50 %.

The core-shell nanorods studied in **PAPER I** were sliced with the focused ion beam (FIB) to prepare thin specimens of individual nanorods for imaging in the TEM. To improve conductivity, the specimens were coated with Pd/Au, and Pt.

### 3.6 X-ray methods

#### 3.6.1 Thin-film X-ray diffraction

A special case of scattering is when the material is periodic and the incident light is monochromatic and parallel, resulting in *diffraction*, which is the constructive interference of elastically scattered electromagnetic waves by electrons in a crystalline material. As interatomic distances in crystals typically are a few ångströms, X-rays are the most suitable light source.

X-rays scattered by different lattice planes will interfere constructively only when their difference in path length is equal to an integer  $n$  times their wavelength  $\lambda$ , and thus give rise to a reflection in the diffractogram. This is Bragg's law:

$$2d \sin \theta = n\lambda \quad (3.8)$$

where  $d$  is the adjacent crystal plane spacing and  $\theta$  is the angle between the incident X-ray beam and the normal of the reflecting lattice plane, and  $n$  is the diffraction order. The distance  $d$  between two parallel and adjacent atomic planes in a cubic crystal system is  $d = a/\sqrt{h^2 + k^2 + l^2}$ , and in the hexagonal crystal system:

$$\frac{1}{d^2} = \frac{4}{3} \frac{h^2 + hk + k^2}{a^2} + \frac{l^2}{c^2} \quad (3.9)$$

XRD was not very useful for our thin film samples, which were thin and non-monolithic and thus realized very little interaction volume. Instead, we used grazing incidence X-ray diffractometry (GI-XRD) at very incident low angles and even then had some trouble quantifying the sample's reflections. We mainly used diffraction as a phase identification technique, but XRD is of course capable of yielding many sorts of structural information, such as crystal

**Table 3.2.** Names and symmetry properties of the materials under study as well as chemically adjacent phases. PDF number signifies our chosen JCPDS reference, mineral the naturally occurring mineral (if any), class the typical crystal structure, system the crystal family, and space group is shown using Hermann-Mauguin (international) notation.

Phase	PDF number	Mineral	Class	System	Space group	Ref.
SnO <sub>2</sub>	00-041-1445	cassiterite	rutile	tetragonal	$P4_2/mnm$ (136)	[163]
Zn <sub>2</sub> SnO <sub>4</sub>	00-024-1470			cubic	$Fd\bar{3}m$ (227)	
ZnO	00-036-1451	zincite	wurtzite	hexagonal	$P6_3mc$ (186)	[164]
CdS	41-1049	greenockite	wurtzite	hexagonal	$P6_3mc$ (186)	
CdS	01-89-0440	hawleyite	zincblende	cubic	$F\bar{4}3m$ (216)	
ZnFe <sub>2</sub> O <sub>4</sub>	01-070-3377	franklinite		cubic	$Fd\bar{3}m$ (227)	[165]
$\gamma$ -Fe <sub>2</sub> SiO <sub>4</sub>	00-034-0178	fayalite		orthorhombic	$Pnma$ (62)	
$\alpha$ -Fe <sub>2</sub> SiO <sub>4</sub>	04-008-1861	ringwoodite		cubic	$Fd\bar{3}m$ (227)	
FeO	01-089-0687	wustite		cubic	$Fm\bar{3}m$ (225)	[166]
Fe <sub>3</sub> O <sub>4</sub>	00-019-0629	magnetite	spinel	cubic	$Fd\bar{3}m$ (227)	[167]
$\alpha$ -Fe <sub>2</sub> O <sub>3</sub>	00-033-0664	hematite	corundum	trigonal	$R\bar{3}c$ (167)	[168]
$\gamma$ -Fe <sub>2</sub> O <sub>3</sub>	00-039-1346	maghemite		cubic	$P4_332$ (212)	[169, 170]
$\beta$ -FeOOH	00-034-1266	akageneite		monoclinic	$C2/m$ (12)	[169, 170]
$\delta$ -FeOOH	01-077-0247	ferroxhyte		hexagonal	$P3m1$ (156)	[169]
$\alpha$ -FeOOH	04-014-5919	goethite		orthorhombic	$Pnma$ (62)	[169]
$\gamma$ -FeOOH	00-044-1415	lepidocrocite		orthorhombic	$Cmcm$ (63)	[169, 170]

structure, average grain size, preferred crystal orientation, epitaxy, periodic defects, and the presence and magnitude of strain in the material.

The relation between the grazing incidence angle,  $\alpha$ , and the depth traversed by the X-rays into the material,  $\tau$

$$\tau_{1/e} = \frac{\sin \alpha}{\mu} \quad (3.10)$$

which is the depth at which the intensity of the X-ray beam has decreased to  $1/e$ .  $\mu$  denotes the linear attenuation coefficient, which is a material-specific value.

XRD measurements were also employed to determine the average crystallite sizes in solid materials. Smaller particle sizes cause a broadening of the reflections, which can be calculated by the Scherrer equation [162]

$$g = \frac{K\lambda}{B \cos \theta} \quad (3.11)$$

where  $g$  is the crystallite size,  $K$  is the particle shape factor which is typically 0.9 for spherical particles,  $B$  is the full-width half maximum (FWHM) of the reflection (minus the instrumental broadening), and  $\theta$  is the diffraction angle.

To identify material phases we compared the measured  $d$ -spacings and their fitted intensities with reference values from the JCPDS PDFs [164] (see table 3.2).

### 3. Characterization methods

#### 3.6.2 X-ray spectroscopy

In addition to XRD, some projects in this work also involved X-ray fluorescence or X-ray photoelectron spectroscopy. In both of these techniques X-rays are absorbed by the sample, and they only differ (on a conceptual level) by what happens next: with X-ray fluorescence (XRF) we detect the emitted characteristic X-rays, and with X-ray photoelectron spectroscopy (XPS) we detect the emitted photoelectrons. A major practical difference is that XPS requires a vacuum between the sample and the detector, but with the upside of a much higher energy resolution and a very surface-sensitive signal.

Whereas observed peaks in XPS are due to *elastically* scattered photoelectrons (*inelastically* scattered photoelectrons in fact make up the background), observed peaks in XRF are due entirely to *inelastically* scattered X-ray radiation (i.e., fluorescence).

For a maximum fluorescence yield, the incident X-ray energy should lie just above the binding energy of the electronic transition of interest (for incident X-ray energy much higher the yield decreases, analogous to how photons much higher than the  $E_g$  are a waste of energy). Therefore, we always selected a secondary target with atomic number just larger than the heaviest element in our sample, usually Ge ( $Z = 32$ ).

Our XRF experiments were performed on a PANalytical Epsilon 5 with a W (tungsten) anode operated at 75 kV and 8 mA. Each recorded spectrum was usually set to a live time of 240 s with dead time varying between 10 % and 15 %.

XPS is based on the *photoelectric effect* (of Einstein and Nobel Prize fame), stating that a surface exposed to electromagnetic radiation of energy large enough to overcome its first ionization energy emits electrons [171]. The kinetic energy of the emitted photoelectron is related to its binding energy,  $E_B = h\nu - E_k$  [171]. The binding energy,  $E_B$ , is the difference between the total energy of the system in its initial state (before X-ray excitation) and final state (after emission of a core-level electron). From a conservation of energy standpoint, then, the following holds:

$$\begin{aligned} h\nu + E_{\text{initial}}(N) &= E_{\text{final}}(N-1) + E_k \\ E_B &= E_{\text{final}}(N-1) - E_{\text{initial}}(N) \\ h\nu &= E_B + E_k \end{aligned} \tag{3.12}$$

where  $E_{\text{initial}}(N)$  is the total energy of the neutral system with  $N$  electrons, and  $E_{\text{final}}(N-1)$  is the total energy of the now cationic system *after* an electron with kinetic energy,  $E_k$  has been ejected due to its absorption of the X-ray photon  $h\nu$ .

Assuming the Fermi levels of the sample and the XPS spectrometer are aligned (true if the sample is conductive and in good electrical contact with the spectrometer) the binding energy can be determined from the experimentally measured kinetic energy,  $E_k$  [9]:

$$E_B = h\nu - \phi - E_k \tag{3.13}$$

Since the emitted core electron has to pass through the electron density at the atom's surface, the  $E_B$  measured by XPS experiences a *chemical shift* that depends on the valence electron charge density due to chemical bond formation [9]. The realization that the chemical shift observed in core-level XPS provides information about the chemical environment in the sample was made by Siegbahn et al. [172] at Uppsala University. The simplest way I have found to conceptualize the chemical shift is probably in terms of electronegativity: if the valence electrons of the atom in question are being pulled away by a more electronegative neighbour, the core electrons experience less *screening* of the nuclear charge, and should thus be bound harder than otherwise, causing a chemical shift towards higher binding energy.

Samples need to maintain electrical neutrality during the measurement. Insulating or semiconducting samples will otherwise experience charge-up, leading to mismatch in Fermi level between the sample and the spectrometer. This can be corrected by use of a flood gun (low energy electron gun) inside the sample chamber to neutralize the sample. But even so, it is difficult to perfectly compensate for this charge-up, which will lead to an observed shift in the binding energy making it necessary to calibrate the energy scale using a known elementary peak. We calibrated against the hydrocarbon surface contamination peak C 1s which has a known value of 285.0 eV.

If the atom is in an excited state (such as at a higher oxidation state) the chemical shift is perturbed further, causing a so called "shake up" transition at the higher energy side of the core level transition. The  $\Delta E$  between the core level and the shake up transition is highly characteristic of the chemical oxidation state of the atom.

The XPS at the department of chemistry (in the ESCA-lab) has a tungsten anode which we operated with an aluminium cathode that emits radiation at 1487 eV. The measurements were performed using a PHI 5500 spectrometer, using monochromatic Al  $K\alpha$  radiation (1487 eV), with an electron emission angle of  $45^\circ$  (tungsten anode, aluminium cathode). The dimensions of the probed region were approximately 2 mm by 4 mm. We used a flood gun since our samples (thin semiconducting films on glass) were not sufficiently electrically conductive.

Peak fitting was done with Fityk v1.3.1 [173]. I stripped the baseline of each C 1s spectrum using a spline function and the transitions were fitted using three pseudo-Voigt kernels, and the offset of the fitted C 1s transition from the reference value 285.0 eV was calculated. Finally, the energy scale of each survey spectrum and all its transitions were offset accordingly.

Apart from using X-ray spectroscopy one can also probe the characteristic X-ray energies from core levels using energy dispersive spectroscopy (EDS), which was used to record the equivalent of XRF spectra but on the micro-scale as well as to create 2D maps of elemental composition over areas of interest. The elemental *fluorescence yield* (c.f. figure 4.1a) applies also for EDS, which had the practical effect of making lighter elements effectively invisible.

### 3. Characterization methods



## 4. Algorithms & datasets


It seems that we live in a time of transitions. The energy transition is underway, even if at times the speed appears glacial. Simultaneously, the scholarly publishing system is indeed morphing into one built on open science. But whereas the energy transition is driven by an urgent need to halt GHG emissions, the transition to open science has been inevitable [174] since the Web was gifted to the world by Berners-Lee and CERN [175] and dropped the marginal cost of distribution of text (and later images and videos) to effectively zero.


*Open science* or *open scientific knowledge* commonly refers to the “open access to scientific publications, research data, metadata, [...], software, and source code” under a *libre* licence and free of charge [176, 177]. This chapter mainly concerns itself with open access to *research data*, as defined by OECD [178] almost 20 years ago:

[...] factual records [...] used as primary sources for scientific research, and that are commonly accepted in the scientific community as necessary to validate research findings. A research data set constitutes a systematic, partial representation of the subject being investigated.

The Swedish Research Council stated in 2020 that the transition to open access to research data shall be fully implemented no later than 2026.<sup>1</sup> Which may sound ambitious, but a lot has actually been happening both across Europe and the world in recent years, for example: guidelines have been published for the scientific management of FAIR data (also specifically for chemistry data) [179–183], as well as practical guides on how to manage data to ensure reusability [184] and a radical idea on how to finance it [185]. FAIR principles have also been introduced for *research software* [186], and a light shone on the perceived barriers to sharing [187].

There is clearly a lot of inertia in science, but I would like to believe that once it picks up speed the transition will be unstoppable. That also means that the best time to influence this transition is right now. There are different levels of software reproducibility, and you should strive for the highest one you can manage:<sup>2</sup> (i) software is not mentioned; (ii) software is mentioned, but not described; (iii) software is described, but not made available (or by request only); (iv) software is made openly available; (v) ...with a permissible licence; (vi) ...with documentation and testing; and (vii) software is shared as a generalized package.

<sup>1</sup><https://www.vr.se/english/mandates/open-science/open-access-to-research-data/the-way-towards-open-access-to-research-data.html> 


<sup>2</sup>These criteria were formulated by Steve Crawford  in a NASA talk.

## 4. Algorithms & datasets

The benefits of sharing data are, I would like to think, self-evident. By also sharing the code that was used to turn that data into the reported results, the combined artefact gains more value than the sum of its parts. It is natural to worry that one's code is not "good enough" to be publicly shared, but in the words of the *Code is science Manifesto* [188]: "You do not have to be a computer scientist or professional software developer to write code, and your code does not have to be perfect in order to be published. If code produces paper-ready results, the code too is paper-ready." By sharing your data *and* your code, you give others the ability to stand on your shoulders, instead of just admiringly looking at you flexing them. Shared data and code is a prerequisite to *validate* and *reproduce* research findings.


An important part of a reproducible scientific workflow is to express visualizations and tables as code rather than producing them by copy-pasting data into a point-and-click tool. Likewise, and this might not be a popular opinion, the command line is powerful and can save a serious amount of time doing otherwise mundane computation tasks [189].




The scientific quality of your shared data can be significantly improved by including units and/or uncertainties in the data itself [190]. This can be achieved with both R and Python, but is still somewhat of a challenge. In **PAPER III** we managed to include uncertainties (but not units) in the data itself, such that the error propagation then became automatic. In fact, in 2022 the Physical Chemistry division of IUPAC launched the project "Digital representation of units of measurement" in collaboration with CODATA and CIPM [191, 192].

To make a paper completely reproducible you can use the following approach:<sup>3</sup> (i) use Git for version control, (ii) use Quarto for your analysis code and *generate* the desired output format using pandoc, (iii) when your paper is done post it to a preprint server, (iv) post your data to an appropriate repository like SND  or a general-purpose repository like Zenodo, (v) publish any software you develop to a controlled repository like CRAN, and (vi) participate in the post-publication discussion on the Fediverse and with a blog The point is to inextricably tie the data to the manuscript by expressing visualizations as code, in addition to putting all of it under version control. Such a manuscript can be called a *reproducible manuscript*.

The rest of this chapter briefly presents some of the algorithms and datasets that I have shared publicly<sup>4</sup> and that this thesis has reused in some form. I have always used Git to have version control (this allows a specific version of the code/data to be referenced, which is invaluable in case the implementation changes or in case of bugs). And to make it easier for others to get started quickly, I have almost always managed to share these tools as R packages.<sup>5</sup>

---

<sup>3</sup>These criteria were inspired by Jeff Leek <https://simplystatistics.org/posts/2015-12-11-instead-of-research-on-reproducibility-just-do-reproducible-research> .

<sup>4</sup>Almost all via GitHub , but also via Git hosting services Codeberg  and Gitea .

<sup>5</sup>An R package is a way of collecting code, data, and documentation into a structured and standardized collection of files that can also explicitly state its dependencies.

## 4.1 Notes on spectral peak fitting

Peak fitting is a very complex problem, but luckily it is one that has already been solved many times over. Unless you have very specific needs, there is no need to implement your own peak fitting algorithm. In the R ecosystem, there is of course the well-regarded `hyperSpec` package, but I never felt comfortable with its attempt to do *everything*. My preference is software that hews closer to the Unix philosophy of “doing one thing and doing it well”. I believe this software philosophy also happens to agree well with the scientific principle of parsimony [193].

I was lucky to have decided from the get-go to only consider peak fitting software that enabled a reproducible analysis, meaning not only the output but also the input parameters must be possible to put under version control. So I was delighted when the `diffraction` CRAN package crossed my path. Here was an extremely well-documented, fully automatic, R-based peak fitting algorithm [151] specifically geared for X-ray diffraction but whose documentation [194] noted it could be useful for the analysis of Raman, FTIR, NMR or mass spectrometry data.

I tested its baseline identification and peak decomposition functions successfully on my own Raman, XRF, Mössbauer and XRD data, and created simple wrapper scripts to work around some of the idiosyncracies of the `diffraction` package (primarily by reining in its tendency to happily repeat an already accomplished fitting). The algorithm provided all the expected peak parameters such as centroid position, area, height, FWHM, goodness of fit values, etc.. The resonant Raman analysis in **PAPER IV** was completed using my `diffraction` wrapper. I found that this algorithm struggled when presented with spectra that required fitting multiple kernels to each physical peak, as it lack the ability to “lock” certain parameters and re-run the fitting.

Sticking to my guns, I started looking for alternatives. Enter Fityk by Wojdyr [173], a GUI peak fitting program which thanks to an ingenious built-in command-line terminal coupled with a built-in logging mechanism affords the same degree of reproducibility by automatically writing the corresponding text command (including arguments) for every user interaction in the GUI to a text file that is then *executable* by the Fityk built-in terminal.

In light of this parity with regards to reproducibility and marked improvements in many other respects, Fityk has become this author’s tool of choice for spectral peak fitting.

## 4.2 Converting between reference electrode scales

The algorithm at the heart of **CONTRIB. 6** was not complicated, as the electrochemical reference scales are essentially related by constant offsets, but to make the algorithm more useful it also takes into consideration each reference scale’s temperature and concentration dependence. This involved creating a matrix

## 4. Algorithms & datasets

for each reference scale, and then finding the desired point in  $(T, C)$ -space (so to speak) by linear interpolation.

This package supports conversion to/from any of the following reference electrodes: standard hydrogen, silver–silver chloride, mercury calomel, lithium, sodium, magnesium, and the absolute vacuum scale. I designed the internals of the package to make it relatively easy to extend it with more reference electrode scales or with additional temperature/concentration values.

### 4.3 Tauc fit algorithm

In order to facilitate the calculation of optical band gap values from hundreds of UV-Vis spectra, I designed a semi-automatic algorithm based in part on work shared with me by a former colleague. Many papers in the literature that rely on band gap values determined via Tauc fitting unfortunately lack the necessary information for someone else to reproduce the analysis. In this algorithm such reproducibility is near guaranteed since all the input parameters (that control the Tauc fit) must be provided explicitly as function arguments. If the user additionally uses version control (as they should), *and* create their Tauc plots with code, reproducibility should be ensured. In fact, that is precisely how the Tauc fits in **PAPER I** were managed.

Tauc fitting builds on the known fact [195, 196] that the product of a semiconductor's absorption coefficient,  $\alpha$  and the incident photon energy  $h\nu$  is proportional to the square root of the energy difference between its  $E_g$  and the incident photon energy  $E$ :

$$\alpha h\nu \propto (E - E_g)^{1/r} \quad (4.1)$$

where the exponent  $r$  indicates the nature of the electronic transition:  $r = 1/2$  for direct allowed transitions,  $r = 3/2$  for direct forbidden transitions,  $r = 2$  for indirect allowed transitions, and  $r = 3$  for indirect forbidden transitions.

A detailed description of the implementation of my Tauc algorithm can be found in the vignette to the `uvvistauc` package (link in the margin).

CONTRIB. 5 

The `uvvistauc` package is a *dependency* of **PAPER I**. Of course, the paper has many other dependencies,<sup>6</sup> such as the SpectraSuite software and driver on the computer, its operating system, and any software running on the hardware of the spectrometer itself. Ideally, the source code for all these dependencies would be freely available to everyone, so that the behaviour of the system could be validated and data reproducibility ensured.

### 4.4 Dataset of band edges and gaps

This dataset lists the energy position (potential) of the valence and conduction band edges for some semiconductors in contact with an aqueous electrolyte. It

---

<sup>6</sup>For the sake of brevity, let us limit ourselves to *software* dependencies.

**Table 4.1.** Absolute band edge potential at the pH of zero-point charge for each material. All band edge potentials vs SHE.

Formula	$E_{CB}/V$	$E_{VB}/V$	$E_g/V$	pH	$pH_{ZPC}$	Ref
ZnS	-0.98	2.62	3.60	1.70	1.70	[214]
SnO <sub>2</sub>	0.06	3.56	3.50	4.30	4.30	[214]
NiO	-0.44	3.06	3.50	10.30	10.30	[214]
<i>n</i> -TiO <sub>2</sub> (anatase)	-0.23	2.97	3.20	5.80	5.80	[214]
ZnO	-0.25	2.95	3.20	8.80	8.80	[214]
In <sub>2</sub> O <sub>3</sub>	-0.56	2.24	2.80	8.64	8.64	[214]
CdS	-0.46	1.94	2.40	2.00	2.00	[214]
<i>n</i> -Fe <sub>2</sub> O <sub>3</sub> (hematite)	0.34	2.54	2.20	8.60	8.60	[209, 214]

is certainly not comprehensive, but manages to include most binary and tertiary semiconductors found in the literature. Table 4.1 shows a subset of the dataset, in this case with the band edge potentials at the pH of point of zero  $\zeta$  potential (PZZP) for each material (all in the dark). You may note that figure 1.3 is also built on this dataset.

This sort of “band edge level” plot showing relative or absolute position of the VBE and CBE at the surface of various semiconductor electrodes abounds in the photoelectrochemical literature.<sup>7</sup>

The package was designed with functions to add new data (new materials), to create L<sup>A</sup>T<sub>E</sub>X-formatted tables of the data, or to plot the dataset. By recording the pH at PZZP, and explicitly noting whether the material follows Nernstian pH dependence, the dataset can provide relative band edge levels at any given pH between multiple semiconductors provided they are all Nernstian. For oxide semiconductors in aqueous solutions, H<sup>+</sup> and OH<sup>-</sup> are the dominant adsorbed species, and therefore the potential drop across the Helmholtz layer,  $V_H$ , and the flatband potential,  $E_{fb}$  changes systematically with pH. The pH at which the potential drop across the Helmholtz layer is zero is called the point of zero  $\zeta$  potential [209]. The change of  $V_H$  with pH then follows a straight-forward Nernstian relationship:

$$V_H = 0.059 (pH_{PZZP} - pH). \quad (4.2)$$

<sup>7</sup>For some examples in the primary literature, see Hernández-Alonso et al. [197], Burnside et al. [198], Matsumoto [199], Serpone [200], Kung et al. [201], Kohl, Frank, and Bard [202], Bolts and Wrighton [203], and Lafière, Cardon, and Gomes [204]; in review articles see Mills and Le Hunte [35], Kudo and Miseki [205], Navarro Yerga et al. [206], Grätzel [207], Linsebigler, Lu, and Yates [208], and Nozik [209], Gleria and Memming [210, p. 173]; and in the secondary literature see Miller and Memming [211, p. 89], Morrison [212, p. 289], and Sato [213, p. 313].

## 4. Algorithms & datasets

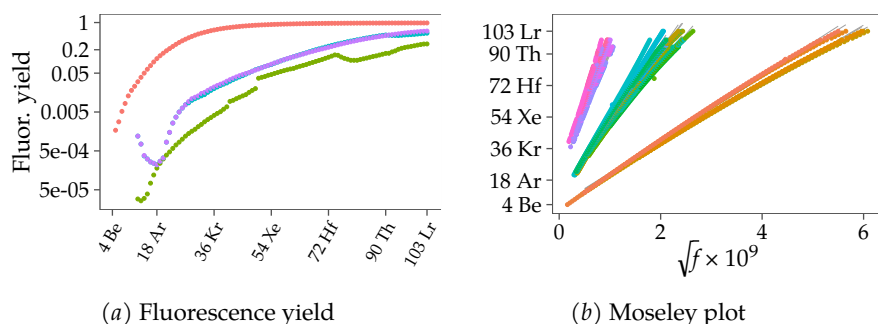


Figure 4.1. (a) Fluorescence yields of the K, L<sub>1</sub>, L<sub>2</sub>, and L<sub>3</sub> lines. (b) The classic Moseley plot reproduced from our dataset of X-ray transitions, showing the expected close-to-linearity of each transition line. The increasingly larger slope of the outer-shell lines says something about the increased shielding experienced by those electrons.

## 4.5 Dataset of X-ray transition lines

For analysing XRF spectra (as well as EDS), it is most useful to have at hand a list of all X-ray transitions of the elements. Freely available data could be found on the web in the form of HTML-formatted “Tables of Physical & Chemical Constants” from Kaye & Laby hosted by the National Physical Laboratory,<sup>8</sup> or in our PANalytical Epsilon 5 XRF instrument’s software,<sup>9</sup> or in the primary literature as poorly formatted tables in PDF files. None of these tables were very convenient to work with, to say the least.

I combined the Epsilon 5 dataset with that of Kaye & Laby, and where the they diverged (usually at the third decimal) I gave priority to the former on account of it being more recent, and extended this combined dataset by adding natural line widths and fluorescence yields for each transition from Krause and Oliver [215] and Krause [216]. To avoid ambiguity I relabelled all transitions that used Siegbahn notation into the systematic IUPAC notation; I was helped by table 10.11 of Lengyel, Ure, and Inczédy [217].

As a quality check, the dataset can be used to recreate the classic Moseley plot<sup>10</sup> (see figure 4.1b).


<sup>8</sup>[https://web.archive.org/web/20190511222636/http://www.kayelaby.npl.co.uk/atomic\\_and\\_nuclear\\_physics/4\\_2/4\\_2\\_1.html](https://web.archive.org/web/20190511222636/http://www.kayelaby.npl.co.uk/atomic_and_nuclear_physics/4_2/4_2_1.html)

<sup>9</sup>Version 2.0J/ICSW 2.8 of Dec 7, 2010 with kernel PW5050. Contained data on every transition’s energy and relative intensity, as well as edge energies for each element. Which were stored in a user-accessible format but had to be manually transcribed.

<sup>10</sup>First constructed by Moseley [218], and at the time a major breakthrough (this was before the discovery of the proton). It identified the existence of up-to-then unknown elements corresponding to  $Z=43$ , 61 and 75 (Tc, Pr, and Re) [219]. Perhaps more importantly, it demonstrated that the elements in a solid sample could be identified by measuring the spectrum of the X-rays it emits.

## 4.6 Dataset of some properties of the elements

Frustrated by the lack of freely available tools to plot one's own periodic table, and realizing that `ggplot2` [220] could be quite easily adapted for the task, I put together a small dataset and designed a proof-of-concept table of elements plot that worked for my own purposes. The IUPAC campaign for the year of chemistry in 2019 gave me the impetus to clean up the generated periodic table and share the code publicly. The eagle-eyed reader might notice that figure 1.2 was in fact created using this dataset.

CONTRIB. 10 

#### 4. Algorithms & datasets



## 5. Optical quantum confinement in low-dimensional ZnO

Chemistry graduates are commonly taught the concept of the triad of *structure, composition, property*, to underscore that a material's properties are determined by its chemical structure and chemical composition. While this is certainly true, it is not the whole truth. There are other parameters along which a material's properties can be tailored. Nanosized semiconductor crystals, despite having the same structure and composition as bulk materials, can have their electronic and optical properties systematically controlled by just *one* parameter: size. This is caused by *quantum confinement*, which opens up another way to tailor the optical and electronic properties of semiconductors.

Quantum confinement effects can become apparent when the distance between allowed energy levels exceed  $kT$ . In semiconductors the Fermi level lies *in* the  $E_g$ , and as the density of states (DOS) in the bulk is generally much smaller near the band edges, confinement effects (splitting of energy levels) can remain apparent even for fairly large particle sizes. Contrast this to metals, where the Fermi level lies in the *centre* of a band, where the DOS is usually large and the distance between energy levels thus small even for very small particles [221]. Quantum confinement is the effect wherein the energy level spacing (the potential difference between energy levels) in the material increases as its particle size decreases. Other phenomena are also affected as nanocrystals are shrunk [221, p. 114], such as the spin-orbit coupling, the electron-hole Coulomb interaction, and the electron-hole exchange interaction, but this chapter will limit itself to the quantum confinement effect.

Quantum confinement provides a way to perturb the semiconductor's band structure by an (external) parameter, in this case the particle size, which we have explored in this thesis. But there are many other ways to perturb the band structure, for example by external pressure (causing uniaxial strain in non-centrosymmetric structures), or temperature, or electric field effects (Stark effects, ionization effects), or magnetic field effects (Landau splitting, the Zeeman effect) [144]. Common for all of them is that they require a sustained external force (i.e., energy) to maintain the perturbation. In contrast, the particle size is a permanent perturbation of the material.

Based on the Schrödinger equation, which shows that when particles become nanosized the electronic states would be *squeezed*, and based on the free-electron gas model for metals, Fröhlich [222] predicted that nanoparticles would have very different values of specific heat of their electrons compared to the bulk metal [223]. Although correct, observing this effect in metals would require

## 5. Optical quantum confinement in low-dimensional ZnO

exceedingly small particle sizes (as we discussed above). Sandomirskiĭ [224] was the first to point out that the effect of quantum confinement should be more easily achievable in semiconductors (owing to their smaller effective electron mass and thus larger exciton Bohr radius,  $a_B$ ), and cause a measurable shift in the optical absorption edge. By the early 1980s experimental observations of quantum effects in thin films were well established [223], and was soon followed by evidence of quantum size effects in *colloidal* nanoparticles [225].

In semiconductors quantum confinement can be approximately described by a simple particle-in-a-box model and its most distinctive effect is that the band gap becomes size dependent [226]. This occurs when the dimension of the semiconductor is commensurable or smaller than the diameter of its exciton Bohr radius, which results in an increase of the exciton binding energy (caused by electron-hole-pairs being forced closer together than in the bulk) [227] and the loss of translational symmetry (due to the smaller size of the particle), causing a splitting of the energy levels instead of the continuous bands in the infinite periodic solid. The size at which this effect manifests itself for different materials depends on their chemical composition (actually the exciton Bohr radius which depends sensitively on the effective mass of the electron which of course depends on the lattice and its composition).

A particle that is quantum-confined along all three dimensions is called a quantum dot (QD), a 2D confined material is called a quantum wire (or rod, depending on aspect ratio<sup>1</sup>), and a 1D confined material is a quantum well (ultrathin film).

An exciton is a quasiparticle made up of an electron and a hole in a bound state, attracted to each other by the electrostatic Coulomb force. In materials with large dielectric constant (such as semiconductors) the Coulomb interaction between electrons and holes is effectively screened, generally causing excitons to have a radius larger than the lattice spacing (so called Wannier–Mott excitons). An exciton forms when a photon is absorbed by a semiconductor crystal, generating an electron in the CB and a hole in the VB, and as the electron and hole relaxes across the  $E_g$  to recombine, the energy released by recombination from the excited state back to the ground state is the sum of three contributions, viz., the electron and hole confinement energy, the exciton binding energy, and the band gap energy [229]. The exciton binding energy is the energy difference due to the exciton having slightly less energy than the unbound electron and hole (this energy depends on the material). And the confinement energy is due to the size of the particle literally restricting the exciton's movement across the finite lattice which increases its energy and thus its radius. So by varying the size of a QD, the confinement energy of the exciton can be controlled, which in turn affects its transition probability and thus its optical behaviour.

For a direct semiconductor (such as ZnO) the optical quantum confinement is simply the electronic quantum confinement, whereas for an indirect semiconductor (such as  $\alpha$ -Fe<sub>2</sub>O<sub>3</sub>) the optical quantum confinement is the combined

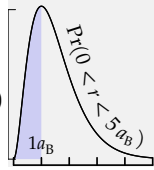
---

<sup>1</sup>With regard to nomenclature, rods generally have a lower aspect ratio than wires, with the cutoff usually at 10 (although this definition is neither official nor always adhered to) [228].

effect of the electronic quantum confinement and the vibrational quantum confinement [8] (indirect transitions are not vertical in an energy-band diagram and thus involve the nuclear coordinate; recall that phonons are effectively nuclear motions of freedom).

The exciton can be described as a electron (negative charge) orbiting a hole (positive charge) at a certain radius, which is analogous to a hydrogen atom. However, the exciton binding energy is much smaller and the exciton radius much larger than the energy or Bohr radius of a hydrogen atom. The exciton Bohr radius,  $a_B$ , can be expressed in terms of the hydrogenic radius,  $a_0$ :

$$a_B = \frac{\hbar^2 \epsilon_r \epsilon_0}{\mu q_e^2} = \frac{\epsilon_r}{\mu/m_e} a_0, \text{ where } \mu = \frac{m_e m_h}{m_e + m_h} \quad (5.1)$$



where  $\mu$  is the so called reduced mass, and  $\epsilon_r$  is the dielectric constant of the semiconductor.

For bulk ZnO,  $a_B = 2.3 \text{ nm}$  but can vary a lot depending on what values of effective masses are used when calculating it. Note that this radius defines the maximum on a *probability distribution* function,  $P(r) = 4r^2/a_B^3 \exp(-2r/a_B)$ , which means that a majority (two thirds, to be precise) of exciton radii will actually be larger than  $a_B$ , and one third smaller (illustration in the margin shows  $P(r)$  in the interval  $0 < r < 5a_B$ ), leading to quantum confinement effects being observed in systems even when their average particle size is larger than the exciton Bohr radius, as observed in our own work (**PAPER III**) and by others [121, 230].

To describe this distribution of exciton radii, one speaks of different *confinement regimes*. When the QD size is larger than several exciton radii ( $d \gg a_B$ ) we are in the weak confinement regime, where the Coulomb interaction between the electron and hole dominates, and thus the exciton is confined, but not the electron and hole individually (the character of the exciton as a quasiparticle is conserved) [231]. When the QD size is smaller than the exciton radii ( $d < a_B$ ) we are in the strong confinement regime, where the quantum confinement energy is much larger than the Coulomb interaction and thus both the electron and hole are independently confined. In this regime the electron–hole exchange energy is larger than the spin–orbit interaction [221, p. 115]. The transition between the strong and weak regimes occurs when the QD size is approximately equal to the exciton Bohr radius,  $d/a_B \approx 1 \sim 3$ .

As we have seen, in the quantum confinement regime the energy required to create excitons will be larger than in the bulk and this energy will increase with decreasing particle size. This means that by decreasing the particle size of a photocatalyst, we can increase the reactivity of the photogenerated electrons and/or holes (depending on whether both band edges shift with particle size). Of course, by increasing the band gap we also further restrict the amount of solar photons the photocatalyst can absorb (c.f. figure 1.1), which may or may not be crippling. The band gap,  $E_g$ , of the photocatalyst in a quantum-confined

## 5. Optical quantum confinement in low-dimensional ZnO

system can be described as a modification of the bulk band gap,  $E_{g,\text{bulk}}$  [8]:

$$E_g = E_{g,\text{bulk}} + \frac{h^2}{8R^2} \left( \frac{1}{m_e^*} + \frac{1}{m_h^*} \right) - \frac{1.8q_e^2}{\epsilon_r R} + \frac{q_e^2}{R} \sum_{n=1}^{\infty} \alpha_n \left( \frac{r_e + r_h}{R} \right)^{2n} \quad (5.2)$$

where the second term is the increased kinetic energy of the electron–hole pair due to being restricted inside a sphere with radius  $R$  ( $m_e^*$  and  $m_h^*$  are the effective mass of the electron and hole, respectively), the third term is the Coulomb attraction in a screened environment, and the fourth term is an average polarization (where  $\alpha_n$  is the polarizability,  $r_e$  and  $r_h$  the coordinate of the electrons and holes with the particle) [8]. As the particles grow and  $R$  increases  $E_g$  will approach  $E_{g,\text{bulk}}$ . This gives a physical motivation for a functional dependence between the band gap,  $E_g/\text{eV}$ , and the particle diameter,  $d/\text{nm}$ :

$$E_g = C_1 + \frac{C_2}{d} + \frac{C_3}{d^2} \quad (5.3)$$

where the constants  $C_1 = 3.30$ ,  $C_2 = 0.293$ , and  $C_3 = 3.94$  were determined in previous work by Jacobsson and Edvinsson [230]. We utilized this model in **PAPER III** to estimate the band gap and particle diameter of ZnO QDs from a series of UV-Vis spectra.

Equation (5.3) can be rearranged to express the particle diameter,  $d/\text{nm}$ , in terms of the band gap,  $E_g/\text{eV}$ :

$$d = \frac{2C_3}{-C_2 + \sqrt{C_2^2 - 4C_3(C_1 - E_g)}}. \quad (5.4)$$

The functional dependence between size and band gap is thus  $d \propto E_g^{-1/2}$ . In section 6.5 I investigated the ZnO QD growth over time based on this relationship.

Several material properties are expected to depend strongly on particle size in quantum confinement regime. Apart from optical and electronic properties, which matter greatly for a photocatalyst, particle size will also affect phonon modes and exciton–phonon coupling, which I have explored in **PAPER IV** (for particle sizes above the weak confinement regime).

Literature suggests that the exciton binding energy is usually smaller than the lattice vibrational energy (LO phonons) in many semiconductors [232], which is supported by our findings in **PAPER IV** ( $E(\text{LO}) = 71.33(5) \text{ meV}$  for the smallest particle sizes studied, c.f. figure 6.14c), but only by about 10 meV if we assume the commonly cited ZnO exciton binding energy of 60 meV.

## 6. Results

In this chapter I summarize results from our published papers (**PAPERS I** and **III**) and results from our not-yet published manuscripts (**PAPERS II** and **IV**), as well as some work on the growth of ZnO QDs that are not presently part of any manuscript (section 6.5).

### 6.1 PC properties of ZnO/CdS nanoarrays

PAPER I

With its wide, direct band gap of  $E_g = 3.3$  eV and with band edge energies close to those of TiO<sub>2</sub> anatase (c.f. figure 1.3), wurtzite ZnO generally shares the same photochemical qualities that make TiO<sub>2</sub> such a compelling PC, but has several advantages such as a higher charge carrier mobility, a direct band gap (and thus high absorption coefficient), longer charge carrier lifetime (reduced recombination), and more flexible methods for nano-crystalline synthesis [233, 234].

From my own experimental experience, ZnO was significantly easier to work with, allowing me to coax it into interesting nanostructures using relatively mild synthesis conditions, whereas TiO<sub>2</sub> required comparatively harsh conditions.

The crystallinity of the electrodeposited ZnO nanorod (NR) films was confirmed by powder X-ray diffractometry (PXRD) (see FIG. 1 of **PAPER I**), which also confirmed its crystal structure to be the thermodynamically stable wurtzite. The NRs grew preferentially along the polar *c*-axis, increasing with deposition time (but not beyond 1.5 h), as expected for a non-centrosymmetric crystal as the surface energy is higher for the non-polar surfaces perpendicular to it. The nanorod diameter was effectively independent of deposition time, which meant that the aspect ratio of the rods also reached its maximum by  $t_{\text{ECD}} = 1.5$  h.

We therefore selected the samples with  $t_{\text{ECD}} = 1.5$  h for subsequent coating with CdS using CBD. As you may recall, the bath for depositing CdS was strongly alkaline, meaning the duration of CdS deposition had to be balanced against the expected etching rate of ZnO. This was also what the XRD results indicated: bath deposition times beyond 10 min markedly decreased the ZnO 2 reflection (indicating that the ZnO nanorods were etched primarily from the top rather than from the sides).

Despite rather low S/N ratio, Raman spectroscopy (see FIG. 2 of **PAPER I**) of the electrodeposited ZnO films confirmed the wurtzite structure. And more interestingly, clearly indicated that the deposited CdS film was in the hexagonal rather than the cubic crystal system (cubic CdS being the thermodynamically stable phase at RT) suggesting an epitaxial effect from the ZnO substrate. Even

## 6. Results

so, the relatively low total mass of deposited material (whether ZnO or CdS) in each sample and the thinness of the film combined with the glass/TCO substrate made it quite challenging to attain high-quality Raman spectra of the deposited film, because of two factors, viz., (a) the well-known roughness of the TCO substrate layer led to a large degree of unevenness in the deposited film, since it was not thick enough to even those out, (b) the laser interaction volume often included not only the deposited film but also the TCO substrate.

The SEM micrographs (FIGS. 3 & 4 of **PAPER I**) indicated that the electrodeposition produced high-density arrays of hexagonal-shaped nanorods with mostly smooth sides and rough-looking end-caps, clearly angled orthogonally to the TCO substrate but due to its unevenness (under SEM observation the clean TCO substrate surface can be seen to consist of many small grains, creating a surface that on the micro-scale looks undulating, almost like sand dunes in a desert but with harsher edges) the nanorods appear to grow in almost all possible directions upwards from the substrate. The specific electrodeposition parameters had a large influence on the density of nanorods and their individual shapes.

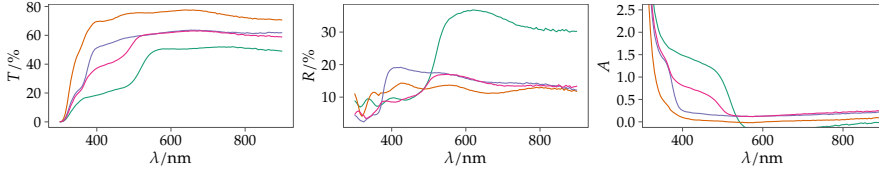
For the shortest CBD deposition times the presence of a CdS coating on the ZnO nanorods was not at all obvious from the SEM micrographs, so we sacrificed a few samples by scratching off the deposited nanorods onto holey carbon and managed to image individual nanorods and record EDS (c.f. FIG. 5 of **PAPER I**). The TEM micrographs demonstrated that the CdS had indeed formed a homogeneous film conformal to the nanorods, and EDS confirmed the formation of a core-shell ZnO/CdS nanorod.

To investigate the UV-Vis absorbance with the integrating-sphere-equipped spectrophotometer we separately measured transmittance (figure 6.1a) and reflectance (figure 6.1b) and then calculated the absorbance (figure 6.1c). The absorbance increased just below 500 nm, as expected for CdS. Furthermore, we used the Tauc method to estimate the optical band gap of the ZnO and the CdS phase, respectively (see FIG. 6 of **PAPER I**). Looking at the high-energy band edge region, the ZnO transition was easy to observe and fit for all samples except for the highest CdS loading whose band gap was severely diminished probably on account of the ZnO phase being mostly etched off. Looking at the low-energy band edge region (inset in FIG. 6 of **PAPER I**), where the CdS band gap is expected, there was no interference from the ZnO which is optically transparent at these wavelengths, and the highest loadings of CdS featured the strongest band edges.

We measured PL spectroscopy (see figure 6.2) at different excitation wavelengths around the expected band gap of ZnO in order to probe the transport of the photoexcited charges across the oxide-sulfide interface. Our hypothesis was that photoexcited electrons on CdS could transfer from its higher-energy CB to the lower-energy CB of ZnO, while the photoexcited holes on CdS would be hindered from doing the same due to the opposite relationship between the VBs (c.f. figure 1.3 for an illustration at equilibrium, in darkness).

At this point it is important to note that the oriented growth of the ZnO nanorods from the FTO surface, although successfully forming dense arrays

## 6.1 PC properties of ZnO/CdS nanoarrays

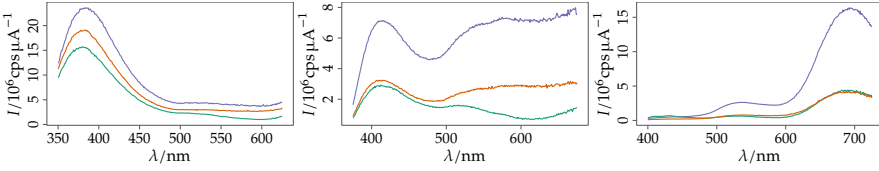


(a) Transmittance

(b) Reflectance

(c) Absorbance

Figure 6.1. Transmittance, reflectance, and absorbance (c.f. eq. (3.5)) spectra of a representative selection of ZnO/CdS samples, subsequently used to calculate their optical band gaps (c.f. Tauc plot in FIG. 6 of PAPER I).



(a)  $\lambda_{\text{exc}} = 325 \text{ nm}$ .

(b)  $\lambda_{\text{exc}} = 350 \text{ nm}$ .

(c)  $\lambda_{\text{exc}} = 375 \text{ nm}$ .

Figure 6.2. Photoluminescence spectra of ZnO/CdS nanorod arrays with varying excitation wavelength ( $\lambda_{\text{exc}} = 325 \text{ nm}$ ,  $350 \text{ nm}$  and  $375 \text{ nm}$ , corresponding to  $3.81 \text{ eV}$ ,  $3.54 \text{ eV}$  and  $3.31 \text{ eV}$ ).

of nanorods, left the parts of the TCO surface not occupied by nanorods as-is, meaning even after ZnO NR deposition the samples were still expected to have lots of exposed FTO surface area. This meant that there were necessarily some CdS deposited *directly onto* FTO, forming an CdS/FTO interface in addition to the desired CdS/ZnO interface. And if the ZnO NR density is low enough, it may well be the case that most of the PL signal would be due not to CdS/ZnO, but instead to CdS/FTO.

All PL spectra showed the two expected luminescent bands of ZnO, viz., the UV and the green emission peaks (except for the longest excitation wavelength, which as expected could not excite the UV peak). For the excitation wavelength larger than the band gap of even the smallest ZnO crystallites ( $3.81 \text{ eV}$ ), only the UV excitation band was observed in the PL spectra, and for the “intermediate” excitation wavelength both the UV and the green emission band could be observed, although the former was diminished about an order of magnitude in intensity. There was no indication of fluorescence attributable to the CdS phase.

The PL results thus suggested that photoexcitation from longer-wavelength light was absorbed by CdS and successfully transferred to ZnO where it caused photoluminescence in the green band.

In experiments to evaluate the PEC properties, samples prepared at different electrodeposition conditions were tested for solar-driven water splitting. The short-circuit current density of some ZnO/CdS samples showed over  $3.3 \text{ mA cm}^{-2}$  under solar-simulated illumination.

## 6. Results

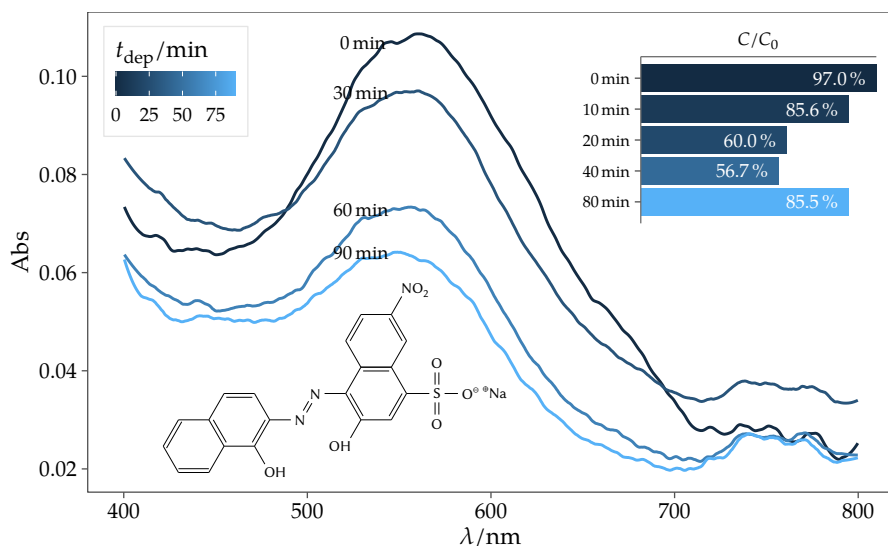


Figure 6.3. Photocatalytic degradation of EBT (structure inset) with PC made of ZnO NR array coated with increasingly thicker layer of CdS (tallied in deposition time,  $t_{\text{dep}}$ ). Main plot shows the experimentally recorded UV-Vis spectra of the dye for varying CdS loading, and the inset barplot shows the calculated  $C/C_0$  for (slightly different) CdS loadings.

To evaluate the ability of our material to act as a short-circuit PC in solution we setup a photodegradation experiment under blue LED light (c.f. box 3.1), yielding an effective irradiance at the sample surface inside the electrolyte solution of  $0.4 \text{ W cm}^{-2}$  and using EBT dye as the model pollutant.<sup>1</sup>

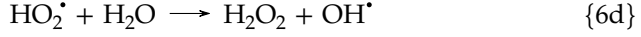
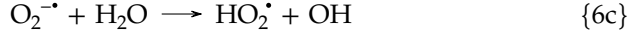
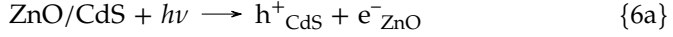
Importantly, we sought to answer whether the CdS-coated nanorod films offered any improvement over their non-coated brethren (by using a visible-light lamp the bare ZnO should not be able to generate photoexcited charge carriers by its lonesome), and additionally, to investigate the degradation mechanism.

We found (c.f. figure 6.3) that the bare ZnO NR film showed practically no photodegradation (the observed 3 % can comfortably be ascribed to self-degradation of the dye under irradiation) and that the PC degradation for the ZnO/CdS films increased slightly with increased CdS loading, which I ascribe to an increased optical absorption in the thicker films. But as the CdS film loading went beyond a certain point, the PC efficiency plummets, which suggests an explanation whereby longer deposition times more or less completely etch off the ZnO nanorods, leaving only the much less powerful CdS as the photocatalysis.

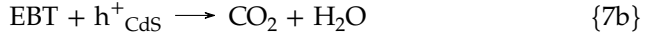
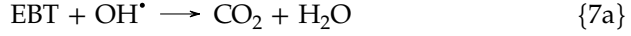
<sup>1</sup>As this was my first foray into dye degradation experiments, the spectrophotometric tracking was performed *ex situ* every 30 min by withdrawing a small aliquot from the continuously mixed PC reaction solution.



This is supported by a (schematic) photodegradation mechanism along the following lines:



where the CdS phase acts as a visible-light absorber, the resultant electron and hole each quickly moving along their energetically favourable directions, effectively separating across the oxide–sulfide interface. The CB electrons in ZnO then react with dissolved  $\text{O}_2$  at its surface, forming  $\text{O}_2^{\cdot-}$  which immediately reacts with  $\text{H}_2\text{O}$  in the solution to form another radical,  $\text{HO}_2^{\cdot}$ , which in turn reacts with another  $\text{H}_2\text{O}$  molecule to create the hydroxyl radical,  $\text{OH}^{\cdot}$ . The dye is then primarily attacked by the highly reactive hydroxyl radical (in solution) or by the hole (at the CdS surface) ideally completely mineralising it (over several steps, not shown here):



So immediately we can infer that a complete coverage of all ZnO surface by CdS would actually not be beneficial to the photocatalytic activity, since that would preclude any formation of hydroxyl radicals. This is in contrast to the PEC performance, which benefits from an even coverage.

We performed this PC evaluation without adding any sacrificial agents, which as expected led to the sulfide layer eventually photocorroding, despite forming a heterojunction with ZnO which removed the photogenerated electrons [235]. This is a well-known limitation of sulfide-based photocatalysts, one that is usually circumvented by adding hole scavengers such as alcohols or sulfide/sulfite ions to the electrolyte solution. At first glance this sounds completely unsustainable, but there are actually many industrial processes that involve sulfates or sulfides where this would not be an objection.

## 6. Results

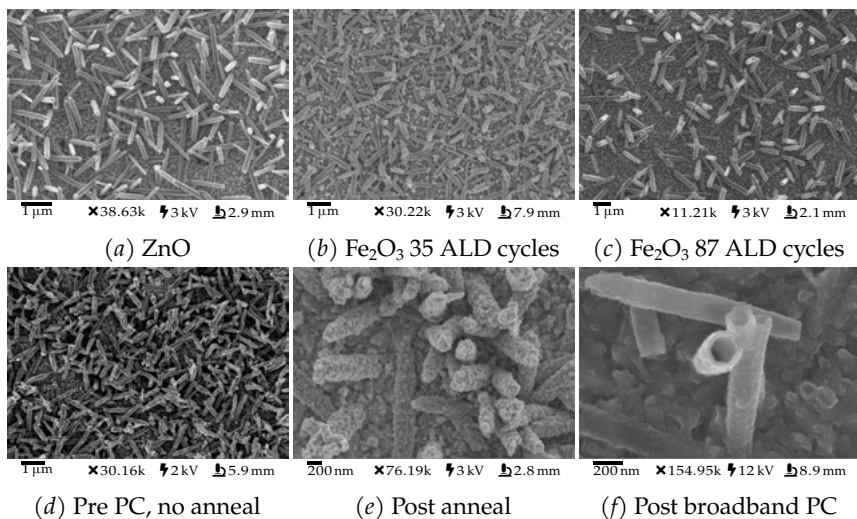


Figure 6.4. Top row: SEM micrographs of photocatalyst before PC, (a) ZnO nanorods prior to  $\text{Fe}_2\text{O}_3$ -coating, and (b) after 35 cycles and (c) 87 cycles. Bottom row: a specimen (d) before annealing, (e) after annealing, and (f) after broadband irradiation during a PC experiment.

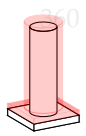
### PAPER II

## 6.2 $\text{ZnO}/\text{Fe}_2\text{O}_3$ core-shell nanorods

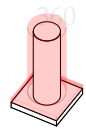
Here we summarise the work and results for  $\text{Fe}_2\text{O}_3$ -coated ZnO NRs. The NRs were synthesised via a template-less electrodeposition route. We observed that the formation of dense arrays of electrodeposited ZnO NRs generally benefitted from an initial voltage pulse, with the best results obtained using a 1 s pulse. Although this is likely very dependent on the deposition conditions we used, including the electrolyte composition and its concentration, the type of TCO substrate, and so on. If we simply apply Faraday's law to the ZnO electrodeposition (reaction {2}), we find that the transferred charge corresponds to no more than  $1.5 \text{ mg cm}^{-2}$ . The real amount of electrodeposited ZnO is most certainly less, since a non-negligible amount of charge is lost to possible side-reactions and cell inefficiencies.

To improve our picture of the electrodeposited ZnO nanorods we also constructed a geometric model based on a typical SEM micrograph (see illustration in the margin). Based on this geometric model, we found that the amount of ZnO was  $0.12 \text{ mg cm}^{-2}$ , or about 10 times less than the amount indicated assuming 100 % Faradaic efficiency of the electrodeposition (reaction {2}).

Electron microscopy confirmed that the electrodeposited nanorods had a hexagonal cross-section and a length just over  $1 \mu\text{m}$  and a diameter of 300 nm, meaning their aspect ratio was above 3. The nanorods faced in practically all possible directions in the hemisphere above the substrate, but this was likely caused by the jagged microstructure of the FTO substrate itself, with each individual nanorod growing orthogonally from the surface of its FTO crystallite, resulting in the varied nanorod directions observed.



Side view.



Oblique view.

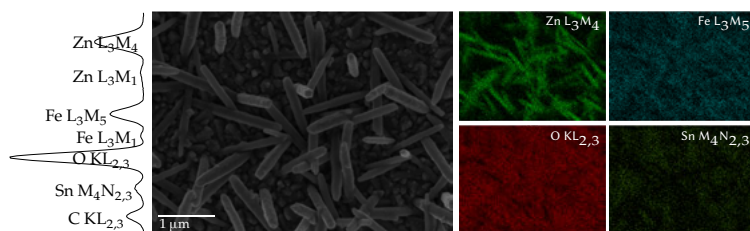


Figure 6.5. EDS map of zinc oxide/iron oxide nanorod array, with EDS sum spectrum shown as sparkline on the left, and elemental map distributions for zinc, iron, oxygen, and tin on the right.

The presence of Fe<sub>2</sub>O<sub>3</sub> is barely noticeable in SEM, except for the highest numbers of ALD cycles and at higher magnification. Annealing the samples did not cause any apparent change to their microstructure. High-intensity irradiation (under the mercury arc lamp, corresponding to several suns) caused the complete etching off of the ZnO phase in the core-shell nanorods leaving the apparent Fe<sub>2</sub>O<sub>3</sub> shell intact (EDS mapping was performed across the mouth of such etched NRs and showed iron in the shell and low zinc signal overall), even retaining the hexagonal shape of the original ZnO core. We would expect iron oxide (rust) to be more chemically and photochemically stable than zinc oxide, particularly under intense irradiation in solution, although such a dramatic effect was unexpected. We did not pursue this further, but this sort of photoetching could be a neat method to produce nanostructured shells (although far from energy effective synthetically speaking).

EDS mapping, presented in figure 6.5, shows the spatial distribution of the expected elements and no unexpected contaminants across the nanorod array. Zinc is clustered along the nanorods themselves, and iron is more evenly distributed, as we would expect. A single Fe<sub>2</sub>O<sub>3</sub>-coated ZnO NR was prepared with FIB-SEM and analysed with TEM (figure 6.6), conclusively demonstrating the presence of an iron oxide coating. Note that the shape of the nanorod and the thickness of the Fe<sub>2</sub>O<sub>3</sub> layer is not necessarily representative due to the effect of how this individual nanorod was cut in the focused ion beam (FIB) and to projection effects in the TEM imaging. We also performed a line scan along the width the nanorod, whose zinc and iron components of its sum spectrum clearly support the ZnO/Fe<sub>2</sub>O<sub>3</sub> core-shell structure.

Even using very low incident angles in GI-XRD configuration the ZnO reflections emanated just above the noise and were still weak compared to the SnO<sub>2</sub> reflections (c.f. figure 6.7). In non-GI configurations the ZnO reflexes were not observable at all. Evidently, the contributions of the relatively sparse nanorods to the X-ray interaction volume was too small compared to the contribution of the compact FTO layer.

We varied the incident angle  $\theta$  between 0.05° and 6°. At incident angles above 0.3° the FTO substrate dominates the pattern. At lower angles it was possible to quantify (fit) some ZnO reflections. For a single diffractogram, we managed to peak fit what was clearly a Hm reflection (by the principle of

## 6. Results

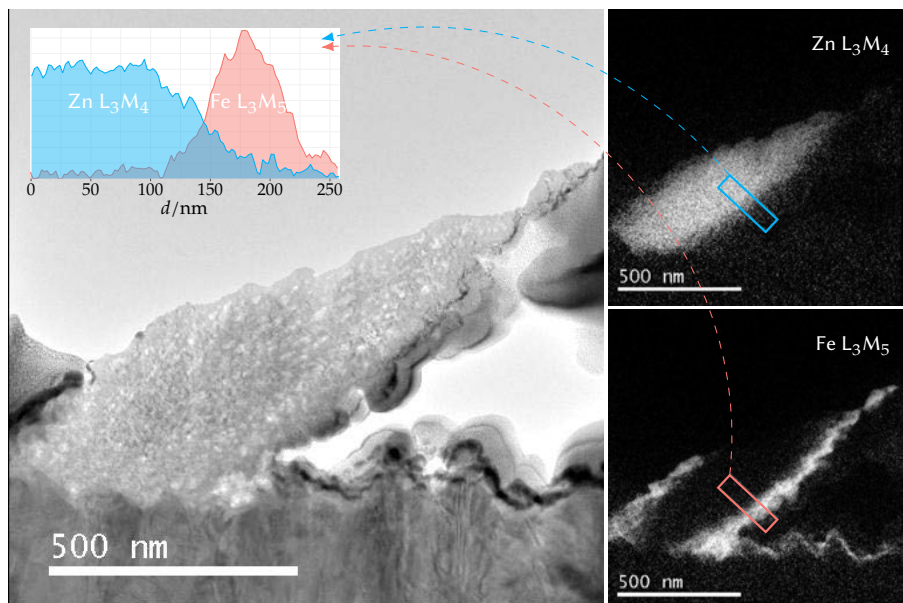


Figure 6.6. TEM micrograph and line profile of a single ZnO/Fe<sub>2</sub>O<sub>3</sub> nanorod.

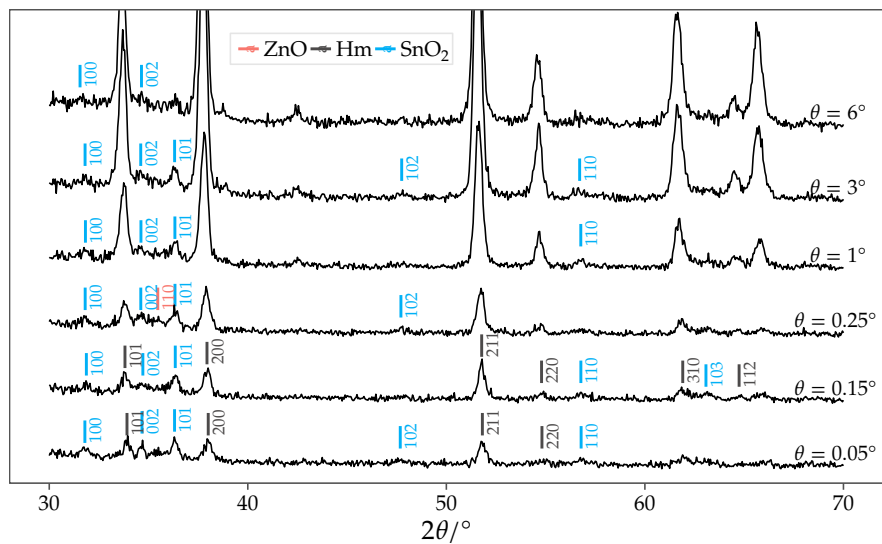


Figure 6.7. GI-XRD series on a ZnO/Fe<sub>2</sub>O<sub>3</sub> thin-film sample (on FTO glass substrate). We varied the incident angle  $\theta$  between 0.05° and 6°.

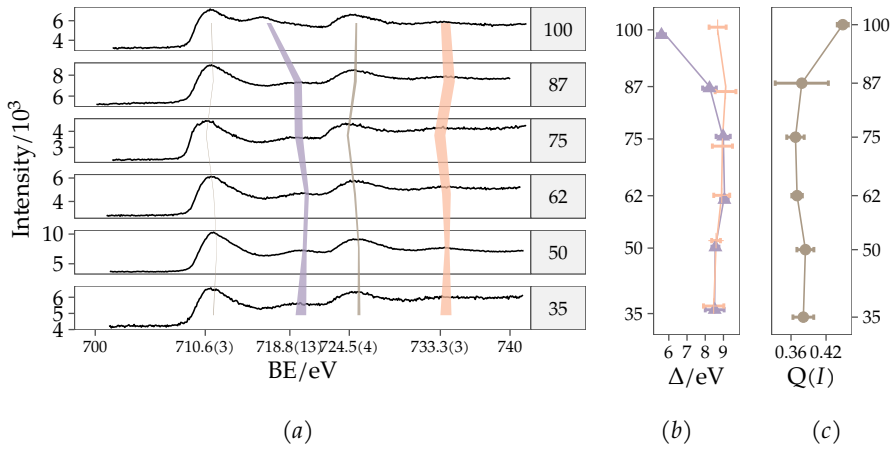


Figure 6.8. XPS spectra of ZnO/Fe<sub>2</sub>O<sub>3</sub> nanorod arrays.

exclusion), although it was below the limit of quantification. An incident angle of approximately  $0.3^\circ$  maximised the ZnO reflections compared to the SnO<sub>2</sub>.

As we were not able to glean structural data on the Fe<sub>2</sub>O<sub>3</sub> phase from XRD, we decided to try the most surface-sensitive technique at our disposal, viz., XPS. Considering the capabilities of the technique, our aim was fairly modest; we merely sought to confirm the presence of  $\alpha$ -Fe<sub>2</sub>O<sub>3</sub>.

Figure 6.8 shows the Fe  $2p$  elemental transition spectrum with the fitted energy (position) of the main and satellite peak marked with vertical-running bars whose widths indicates the uncertainty (standard deviation) in the determined peak position (note how the uncertainty is vanishingly small for the main peaks and quite substantial for the weaker satellite peaks). The determined average peak energy across all Fe<sub>2</sub>O<sub>3</sub> thicknesses is also shown on the horizontal axis labels.

The observed binding energy of the main peaks, as well as the difference between the two main peaks conclusively indicate that the iron oxide phase is Fe<sub>2</sub>O<sub>3</sub>. As shown in figure 6.8b the main peaks are accompanied by satellite peaks about 8 eV away on the high-energy side, which narrows down the possible iron oxide phases to either hematite ( $\alpha$ -Fe<sub>2</sub>O<sub>3</sub>) or maghemite ( $\gamma$ -Fe<sub>2</sub>O<sub>3</sub>).

The quest to conclusively identify the iron oxide polymorph in the core-shell nanorods made us try Raman spectroscopy. Observing any non-ZnO or SnO<sub>2</sub> signal in the Raman spectra was very challenging, likely due to a combination of the substrate being made of glass and the vertical extent of the nanorod array film being very small (less than half a micrometre). It took a significant amount of operator skill (certainly not mine!) to configure the spectrometer and achieve the spectral series in FIG. 8 of PAPER II.

The uncoated nanorods show the expected ZnO Raman spectrum, as well as some SnO<sub>2</sub> modes (c.f. figure 6.9). The hematite Raman spectrum is only apparent for the thickest Fe<sub>2</sub>O<sub>3</sub> coats (which was only about 20 nm thick), suggesting that the thinner Fe<sub>2</sub>O<sub>3</sub> coatings are simply too thin to crystallise

## 6. Results

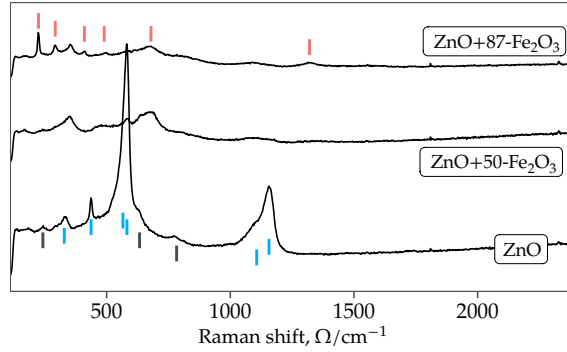


Figure 6.9. Raman spectra ( $\lambda_{\text{exc}} = 405 \text{ nm}$ ) of ZnO/Fe<sub>2</sub>O<sub>3</sub> NR arrays. The short vertical line segments show the Raman shift of the peak fitted center values (red for hematite or Fe–O modes, blue for ZnO, and dark gray for SnO<sub>2</sub>).

properly. Which would make sense from a lattice mismatch perspective and also agrees well with observations by other workers in this laboratory [117, 236].

### Box 6.1: The vibrational properties of hematite

The vibrational modes of hematite (trigonal system, c.f. table 3.2) at the Brillouin zone center are:

$$\Gamma_{\text{vibrational}} = 2A_{1g} + 2A_{1u} + 3A_{2g} + 2A_{2u} + 5E_g + 4E_u \quad (6.1)$$

The symmetrical modes (*gerade*) are Raman active, and the asymmetrical modes (*ungerade*) are IR active, except for the  $A_{1u}$  and  $A_{2g}$  modes which are optically silent [237]. That makes for six IR modes:  $4E_u + 2A_{2u}$ , i.e., four transverse ( $E_u$ ) with dipole moments perpendicular to the crystal  $c$ -axis and two longitudinal ( $A_u$ ) with dipole moments parallel to it [238], and seven Raman modes:  $5E_g + 2A_{1g}$ . Furthermore, hematite is antiferromagnetic and its collective spin movement can be excited in a *magnon*. The interaction of two magnons at anti-parallel spin sites in close proximity create a distinct and broad spectral feature in its Raman spectrum at  $1320 \text{ cm}^{-1}$  [170, 239–242] which can be observed for the thickest film in figure 6.9.

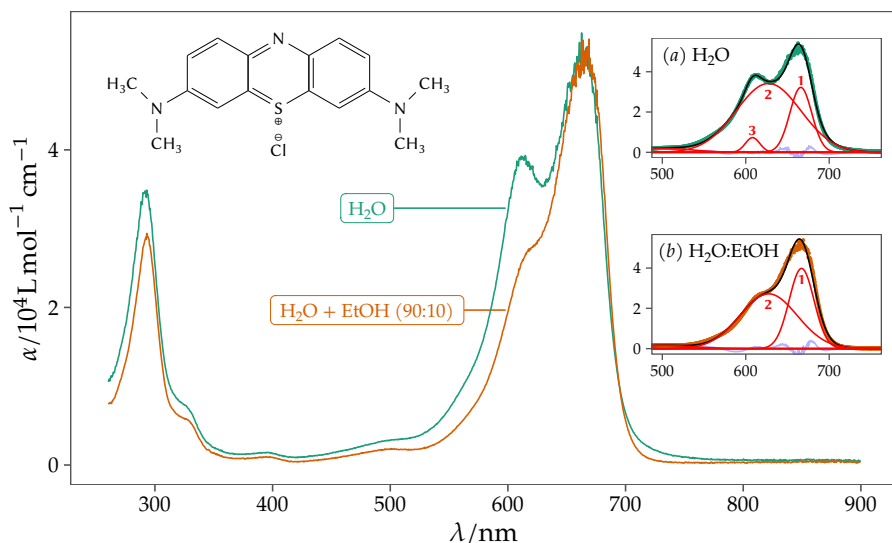


Figure 6.10. Absorption coefficient,  $\alpha$ , for methylene blue in  $\text{H}_2\text{O}$  and  $\text{H}_2\text{O}:\text{EtOH}$  (90:10 by volume), respectively. Insets show the fitted Gaussian kernels (red line) and residual (azure) on top of  $\alpha$  (black dots), sum of kernels (blue line) for (a)  $\text{H}_2\text{O}$  and (b)  $\text{H}_2\text{O}:\text{EtOH}$ . Fitting parameters are listed in SI of PAPER III.

## 6.3 Non-degradative processes in methylene blue dye

PAPER III

In my view, an ideal PC model pollutant would possess (a) a strong absorption band in the UV-Vis-NIR range that does not overlap the band edge of the photocatalyst,<sup>2</sup> (b) no photochemistry of its own, (c) no acid–base reactions, (d) no aggregation or polymerization reactions, and (e) no easily reachable *leuco* state. Methylene blue, despite being a commonly employed model pollutant for photocatalysis with ZnO [243–247], scores only one out of five criteria as specified above (the colour of its main absorption band is well clear of the ZnO band edge). Finding a model pollutant lacking any photo- or redox-chemistry would, of course, be quite impossible. Despite its shortcomings, MB is a good approximant of many polycyclic aromatic compounds that can (unfortunately) be found in the effluent from many industries, and as such it is an important model for photocatalytic degradation.

Our synthesis of ZnO QDs used EtOH solvent, which meant that upon adding the PC to the aqueous-based MB solution some EtOH would be added. This made it necessary to carefully consider our choice of dye, and after testing a few different dyes (c.f. scheme 1) we chose MB as it exhibited the least amount of spectral changes upon mixing with EtOH. And since EtOH and  $\text{H}_2\text{O}$  are completely miscible, I saw no point in attempting to exchange the QDs solvent after synthesis, as some EtOH would always remain. Also, the continued

Blog

<sup>2</sup> Assuming the PC is a wide gap semiconductor this would require the dye to absorb primarily in the red.



## 6. Results

growth of the QDs (even when diluted ten times in H<sub>2</sub>O) added an interesting dimension to the experiment.

The absorption coefficient of methylene blue in H<sub>2</sub>O and in H<sub>2</sub>O:EtOH (90:10 by volume) shown in figure 6.10 was calculated by measuring its absorbance spectrum at seven different concentrations spanning 0.5  $\mu$ M to 50  $\mu$ M. At first glance it appeared that the low-wavelength secondary peak present in H<sub>2</sub>O was simply depressed with the addition of EtOH.

But a closer look revealed that the secondary peak, visible in only H<sub>2</sub>O, went completely missing with the addition of EtOH, and that the remaining shoulder (present in both solvents) was thus due to a third contribution. A comparison with literature confirmed this picture, and our own peak fitting (see figures 6.10a and 6.10b) allows us to propose the following assignments: a monomer  $n - \pi^*$  (also called 0 – 0) band at 666 nm (1) [248, 249], a monomer 0 – 1 vibronic transition at 627 nm (2), and a dimer band at 608 nm (3, which was only observed in the presence of EtOH) [250].

This sort of blue-shift of the main absorption band is called *metachromasy* [249], and is commonly exhibited by dyes whose permanent ionic charge cannot be assigned to a specific atom but is rather part of the chromophoric system (the delocalized electrons of the aromatic system) [251], causing the dye molecules to stack (primarily face-to-face) forming di-, tri-, or even higher aggregates, depending on concentration, pH [252], temperature [253], or solvent (i.e., dielectric constant) [248, 250, 251, 254–257]. Dimerization of MB is favoured in pure water at concentrations as low as 10  $\mu$ M [249], but suppressed on adding alcohol [258]. In alcoholic solvents *monomers only* can be assumed to be present [256, 258, 259]. This is in line with our observations.

### 6.4 Photocatalysis with quantum-confined ZnO

PAPER III

In this paper we proposed that an ensemble of growing ZnO QDs in suspension could be used to photodegrade an environmental pollutant using just sunlight, with the nanoparticulate photocatalyst and the degradation products naturally aggregating into a comparatively harmless sediment.

We observed that the initial nanoparticle diameter (in the quantum confinement regime) had a marked effect on the redox behaviour of the photocatalyst. Apart from tracking the degradation of our organic model pollutant (MB) we also used the UV-Vis band edge of ZnO to track the band gap and derive the particle diameter (c.f. figure 6.11), among other things.

With the changing particle size of the QD not only the band gap was affected, but other physical parameters such as its volume, surface area, and crucially, the *ratio* of surface area to volume. More surface area means more crystal edges, which is expected to increase catalytic activity.

There is also a trade-off between NP size and optical absorption, in that as size decreases and band gap increases, the chance of a photon being absorbed in any one nanoparticle decreases (simply because of less interaction volume



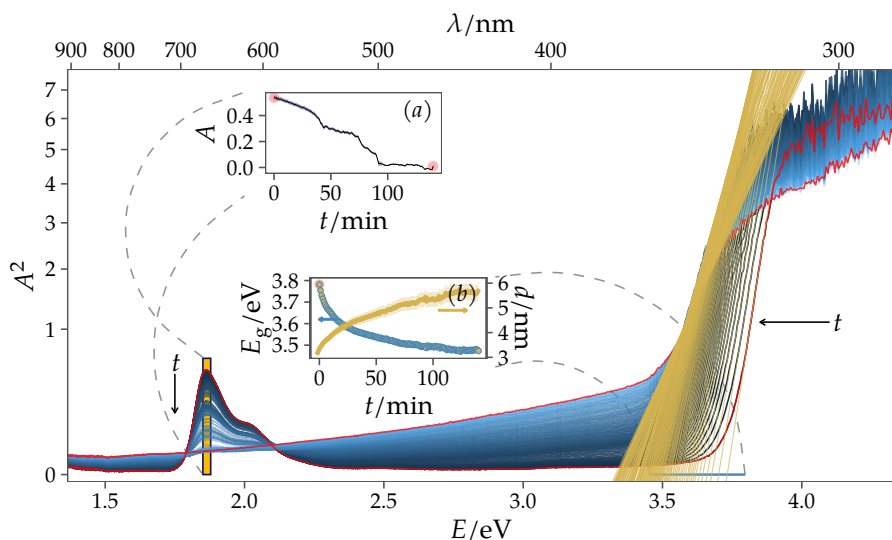


Figure 6.11. Optical absorption spectra recorded under 1 Sun illumination from  $t = 0$  (when ultra-small ZnO(EtOH) nanoparticles were added to the MB(aq) dye solution) until  $t > 2$  h with  $\Delta t = 1$  min. The top inset (a) shows the fitted height of the strongest methylene blue absorption peak vs time. The bottom inset (b) shows the result of a Tauc analysis on the band edge (the Tauc fits are highlighted by the yellow lines intersecting the band edge region of each spectrum in the main plot).

between light and matter). But there are other effects to keep in mind: different wavelengths are absorbed differently at different material thicknesses (i.e., particle size). Another consideration occurs when considering the ensemble of nanoparticles, namely, multiple scattering and thus increasing chance of absorption. The small particle size is expected to decrease the likelihood of charge recombination (because electron and hole are stabilized by surface states where they might react usefully instead of recombining with each other in the bulk).

Animated

We should also mention that although the overall efficiency of our ZnO QDs is expected to be poor under sunlight (only a very small fraction of solar photons have energies above the band gap of our QDs, c.f. figure 1.1), the formed excitons will have large redox potentials thanks to the same large band gap and high quantum efficiency for these wavelengths. Although the photon flux under non-concentrated solar light is very low, this could easily be overcome (with only a minor efficiency penalty) by using a tailored artificial light source.

In this paper we presented a relative comparison of the kinetics of decolourization between ZnO QD ensembles growing from different starting sizes, and found that the smallest nanoparticles (starting size  $< 6$  nm) quickly decolourized MB, whereas the larger nanoparticles ( $> 6$  nm) levelled off without reaching complete decolourization after an initial dip in absorption (c.f. FIG. 6 of PAPER III). We rationalized this behaviour as follows. The photogenerated CB

## 6. Results

electrons may directly reduce MB molecules adsorbed on the nanoparticle, or they may successively produce ROS in solution along the steps we outlined in reactions {6b} to {6e}. We proposed that these processes are in fact competing with each other, depending on the ZnO nanoparticle size which in the quantum confinement regime has a CBE energy level that depends sensitively on particle size.

On the issue of nanotoxicity, which was briefly discussed in the paper, I might add that certainly ZnO (even in the bulk) is not inert, but has a small degree of chemical reactivity, which is in fact what makes it so useful in its many industrial applications. And by controlling the particle size, we are effectively tailoring the material's chemical reactivity (well, in one direction, increasing it), which is very beneficial for its role as a photocatalyst, but is also the reason for its nanotoxicity (or that of any nanoparticulate material for that matter) [54, 56, 260, 261]. This is true in the nanoparticle regime, and even more so in the quantum dot regime. One should also consider the toxicity of the  $\text{Zn}^{2+}$  ion, which although small is considered ecotoxic for aquatic organisms [262]. For comparison, the naturally occurring amount of Zn ions ( $\text{Zn}^{2+}$  being the only one) in seawater is around 5 ppb, and human metabolism requires a daily intake of about 10 mg [262]. As we have noted earlier, at neutral or slightly alkaline conditions the dissolution of ZnO is expected to be minimal, and thanks to the observed aggregation (and subsequent sedimentation) on photoreaction with the pollutant the *nanotoxicity* is thus reduced. Admittedly, this does make it a worse *catalyst*, but since zinc is quite plentiful (c.f. figure 1.2), this sort of application might still be of value where cost-effectiveness in terms of material expenditure is outranked by other considerations, such as environmental cleanup.

### 6.5 Long-term tracking of growth of ZnO QDs

Here we report an unpublished observation on the relationship between ZnO QD particle size and growth time for the same conditions (concentration, temperature, etc.) as those we employed in **PAPER III**.

We spectrophotometrically observed the growth of ZnO QDs in colloidal suspension and tracked their diameter via the empirical relationship between optical band gap and particle size that we established previously (figure 6.12). Initially (from 0 min to 1193 min) spectrophotometry was performed *in situ*, but to track the growth over a longer period of time, later spectra were recorded *ex situ* at a semi-regular frequency until approximately 143 000 min (100 days). The QD colloidal suspension was stored in a sealed glass bottle at ambient conditions and behaved like a sol (the suspension was stable over time) without any gel formation.

Plotting the logarithm of time (in minutes) vs. the particle size (figure 6.12b) shows that the particle diameter grows approximately linearly: for every decade increase in time the diameter increases by 2 nm. The deviation from linearity appears strongest initially, where growth is slower.

## 6.5 Long-term tracking of growth of ZnO QDs

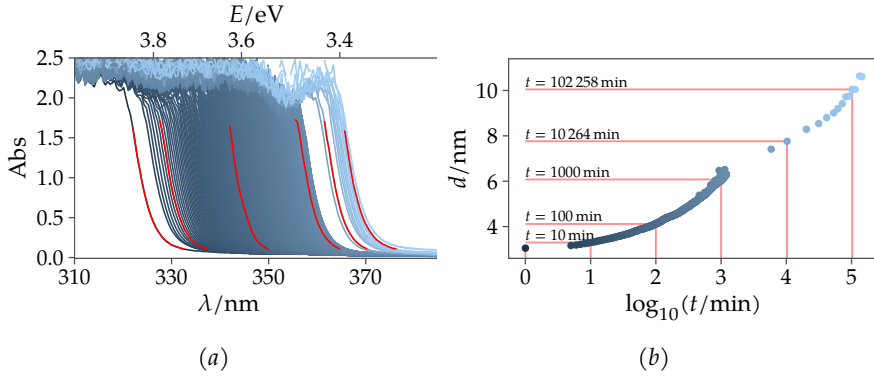


Figure 6.12. (a) Spectrophotometrically tracking the shifting band edge of growing ZnO QDs. As the experiment progressed, the band edge red-shifted (towards higher wavelengths or lower energies). Red lines highlight recorded spectra at  $t \approx 0$  min, 10 min, 100 min, 1000 min, 10 000 min and 100 000 min. (b) Diameter of ZnO QDs vs. time.

The data allows us to relate particle diameter  $d$  in nanometres, to time  $t$  in minutes, using the following empirically derived logarithmic relationship:

$$d = 1.77 \times \log(t) - 0.65 \quad (6.2)$$

This gives an average growth rate of 0.02 nm/min, or  $2.44 \times 10^{-5}$  mm/day. Which is very slow compared to other synthetical routes.<sup>3</sup> Assuming the Zn–O inter-ionic distance is 1 Å, this rate would correspond to just 10 atomic layers per hour.

<sup>3</sup>For comparison, ZnO grown by the hydrothermal method grow around 1 mm/day and by the vapour phase method around 7 mm/day [263, 264]. ALD, which is considered a slow method, deposits material about as fast (depending on whether the flushing steps are counted or not) as a fingernail grows (about 0.1 mm day<sup>-1</sup>).

## 6.6 Non-resonant Raman in nano-dimensional ZnO

In this study, nano-dimensional ZnO powders with particle sizes varying from 10 nm to 150 nm (synthesised by other workers in this laboratory [265]) were studied by non-resonant Raman spectroscopy using blue, green, red, and IR lasers.

For the smallest particle size, 10 nm, corresponding to 200 °C, 300 °C and 400 °C, the spectra were plagued by fluorescence that could drown out the Raman modes, and more so at higher wavelength of excitation. This was likely due to minute organic residues.

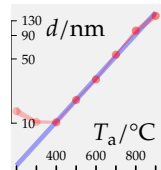
The particle size,  $d$ , was determined using TOPAS full-profile fitting of the ZnO PXRD reflections, and we may note that  $d$  increases logarithmically with annealing temperature,  $T_a$ , if the two lowest temperatures (200 °C and 300 °C) are excluded from the linear fit (blue line is the linear fit, note the  $\log_{10}$   $y$ -axis—all tick marks are equi-distant on the number line; the red ribbon shows the standard error of the TOPAS fit).

We analyzed the  $c/a$  lattice axis ratio to find out if there were any variation in unit cell shape with particle size, and found no such variation within the estimated standard deviation (the pale yellow-coloured band in c.f. FIG. 4 of PAPER IV). This puts to rest any lingering suspicion that the observed trend in the phonon–phonon signal was due to changing unit cell parameters (or due to strain from the rapid cooling step during synthesis).

Another potentially confounding factor we wanted to control for was the well-known effect of local heating due to the laser beam incident on the sample [266], which may potentially cause phase transitions, oxidation of any intrinsically doped oxide, or a local thermal expansion in turn causing a peak shift. To assess this, we fitted both the Stokes and anti-Stokes of the same mode for all particle sizes (c.f. FIG. 5 of PAPER IV and FIG. S3 of PAPER IV), under the assumption that any laser-induced heating would increase the probability of the crystallite being in a vibrationally excited state and thus strengthen the anti-Stokes signal. We saw no indication of that.

The symmetry of space group  $P6_3mc$  dictates that only the  $A_1$ ,  $E_1$  and  $E_2$  optical modes of ZnO are Raman active, but due to overtones and sum/diff modes the non-resonant spectra actually contain a multitude of peaks, which we have assigned after baseline subtraction and peak deconvolution (see box 6.2).

Our access to non-resonant Raman spectra using both blue and green laser excitation (and varying particle sizes) allowed us to make reasonable assignments even in cases where a single observation might have been ambiguous. And by plotting the fitted Raman shift vs. particle size (figure 6.13) it was apparent that the  $E_{1(LO)}$  mode and its overtone behaved differently (at least under blue laser excitation). Whereas all other modes showed practically no shift in  $\Omega$  with particle size, the  $E_{1(LO)}$  modes shifted to higher energy with increasing particle size, which brought it closer in energy to the  $A_{1(LO)}$  mode.



**Box 6.2: The vibrational properties of zinc oxide**

The wurtzite structure has a hexagonal unit cell and belongs to space group  $P6_3mc$  (c.f. table 3.2) ( $C_{6v}^4$  point-group symmetry). Wurtzite ZnO has four atoms per unit cell (and due to the commonly chosen primitive unit cell, two formula units per unit cell) giving a total of 12 fundamental phonon modes. The vibrational modes of wurtzite ZnO at the Brillouin zone center thus belong to the following irreducible representations:

$$\Gamma_{\text{vibrational}} = 2A_1 + 2E_1 + 2E_2 + 2B_1 \quad (6.3)$$

where the  $A_1$  and  $E_1$  modes (optical branches) are both Raman and IR active, the  $E_2$  modes are Raman active, and the  $B_1$  modes are Raman inactive. In addition (not shown) the  $2A_1$  and  $2E_1$  acoustic branches [145].

The following table lists all ZnO Raman modes we observed in this work (first-order modes highlighted in bold, c.f. **PAPER IV**), with our proposed assignments.

Symmetry	$\Omega/\text{cm}^{-1}$	Symmetry	$\Omega/\text{cm}^{-1}$
$E_{2(\text{low})}$	99	$E_{1(\text{LO})}$	574
$2E_{2(\text{low})}$	204	$B_{1(\text{high})}$	—
$B_{1(\text{low})}$	—	$A_{1(\text{LO})}$	581
$E_{2(\text{high})} - E_{2(\text{low})}$	330	$E_{2(\text{high})} + 2E_{2(\text{low})}$	665
$A_{1(\text{TO})}$	384	$2E_{2(\text{high})} + E_{2(\text{low})}$	983
$E_{1(\text{TO})}$	411	$2(E_{2(\text{high})} + E_{2(\text{low})})$	1103
$E_{2(\text{high})}$	438	$2E_{1(\text{LO})}$	1143
$E_{2(\text{high})} + E_{2(\text{low})}$	541	$2A_{1(\text{LO})}$	1153

*Continued on the right*

The  $A_1$  and  $E_1$  modes are each split into LO and TO components due to the macroscopic electric fields associated with the LO phonons [234]. The  $E_{1(\text{TO})}$  and  $A_{1(\text{TO})}$  modes reflect the strength of the polar lattice bonds [234].

Note that our assignment of the  $E_{1(\text{LO})}$  and  $A_{1(\text{LO})}$  modes in this work are in the opposite order compared to some other workers [234, 267, 268]. But this order is more consistent with the observed relative intensities of their respective overtones under the assumption that the stronger overtone should be the  $2A_{1(\text{LO})}$  mode.

## 6.7 Resonant Raman in nano-dimensional ZnO

PAPER IV

The resonant Raman spectra (figure 6.14) are markedly different from the non-resonant Raman spectra: no modes except for  $A_{1(\text{LO})}$  and its harmonic overtones can be observed. The presence of multiple higher-order modes are a strong indicator of the high crystallinity of the ZnO phase, and at the same time the strong fluorescence observed for the smallest particle sizes suggest they are not entirely free of organic residues from the synthesis. Nonetheless, we managed to record the full series of spectra using identical capture parameters allowing us to do a more detailed peak analysis.

After stripping the baseline and peak fitting each LO mode, we set out to investigate the dependence of the physical peak parameters (height, area, width)

## 6. Results

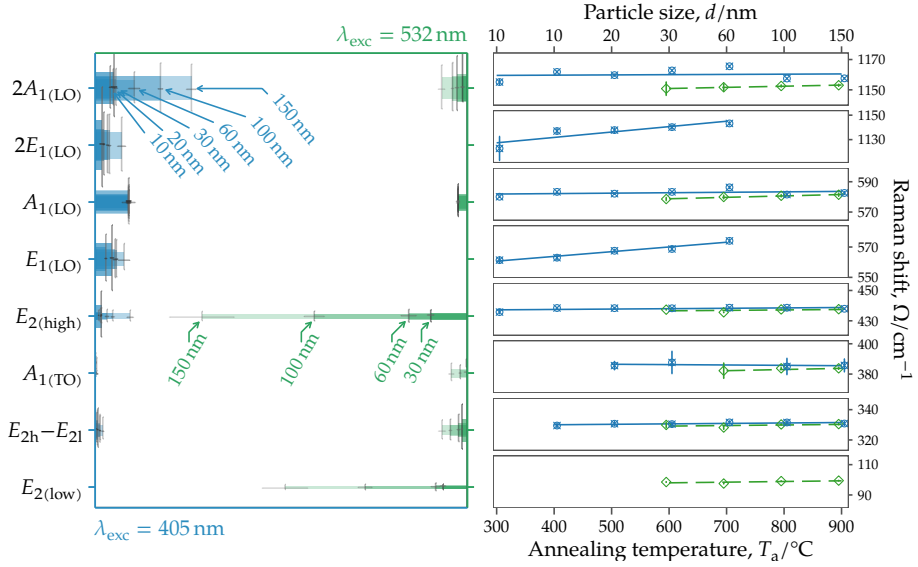


Figure 6.13. Relative peak widths and heights (left panel) and Raman shifts (right panel) of peak-fitted Raman spectra of both blue and green laser excitation. Fitted peak widths and heights are represented as bars (height along the horizontal axis). Some observed Raman modes have been excluded (modes with weak S/N, or those observed for only a subset of particle sizes). Interestingly, only the  $E_{1(LO)}$  mode (and its overtone) show a visible shift vs. particle size. Note that the range in  $\Omega$  of each subpanel has been kept precisely the same to make the slopes visually equivalent. Also note that there is a horizontal correspondence between the bars on the left and their slopes on the right.

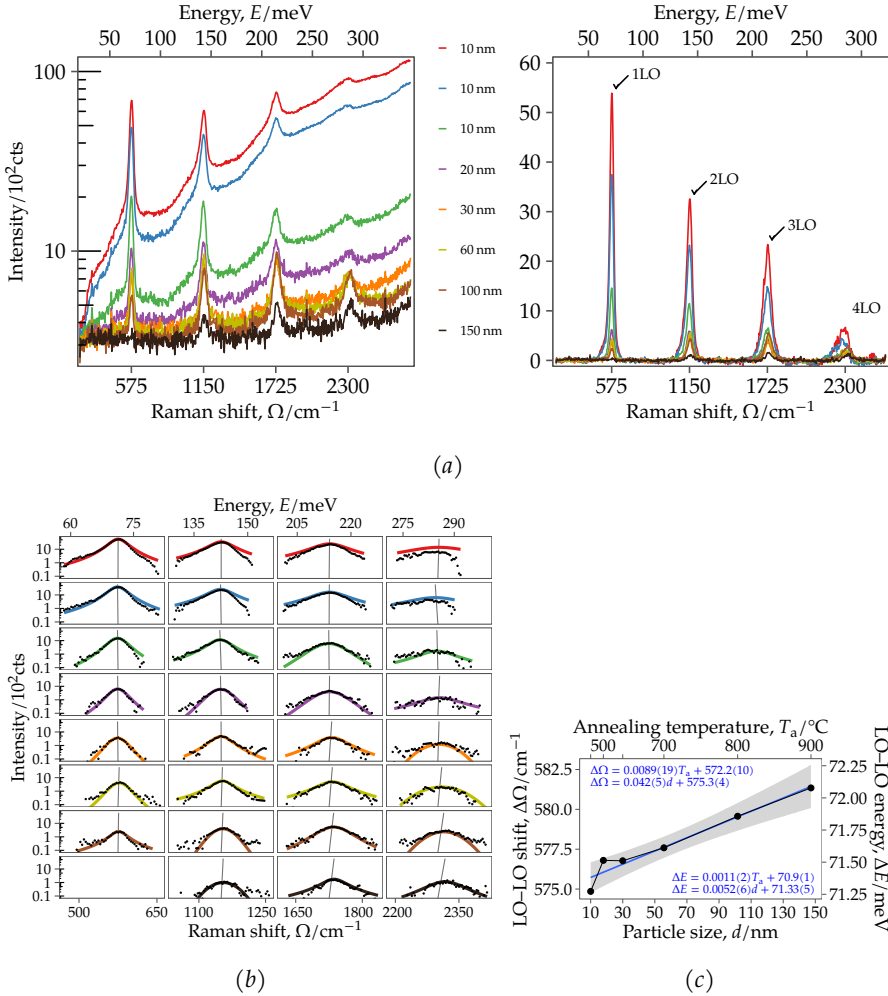


Figure 6.14. Resonant Raman spectra of ZnO nanosponge powder at varying particle sizes. (a) Left panel shows experimentally recorded spectra, right panel after the baseline was removed. Stronger LO modes as particle size decreases. Note the  $\log_{10}$  ordinate of the left panel (fluorescence was intense for the smaller particle sizes). (b) Peak fits in grid, with columns as LO modes, and rows as particle sizes (150 nm at bottom, decreasing sizes upwards, the three top-most rows are 10 nm). Each panel shows the observed LO mode after baseline stripping (black dots), the fitted peak (solid coloured line), and a visual marker whose top and bottom position along the horizontal axis signifies the position of the peak centroid and the expected position of the centroid assuming zero LO-LO shift, respectively. The oddly shaped peaks are caused by the  $\log_{10}$ -transformed ordinate axis. (c) The average LO-LO shift increases linearly with particle size. The linear fit (blue line) gives this slope as  $5.15(60) \mu\text{eV nm}^{-1}$  (or in terms of wavenumbers,  $0.0415(49) \text{ cm}^{-1} \text{ nm}^{-1}$ ), with an  $R^2 = 0.935$ .

## 6. Results

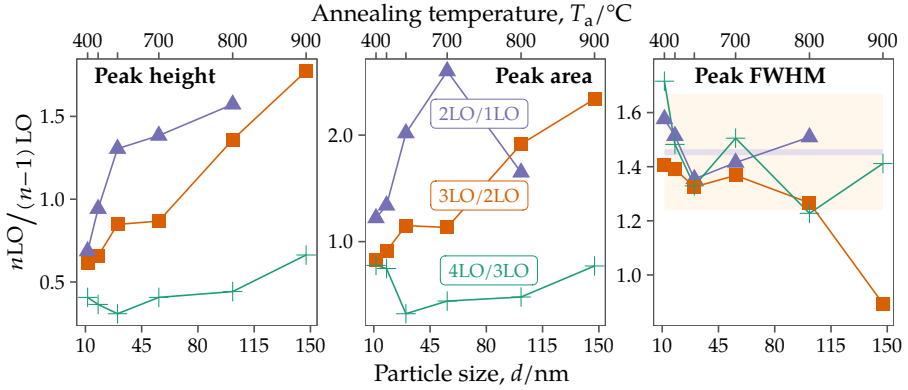


Figure 6.15. Relative height, area and FWHM (expressed as 2LO/1LO, 3LO/2LO, and 4LO/3LO) vs. particle size. In the right-most panel (FWHM), the horizontal blue line denotes the average FWHM ratio across all sizes and LO modes, and the shaded yellow area its standard deviation (vertically), viz., 1.45(22).

vs. particle size (figure 6.15). In line with previous workers, our plot reports relative LO–LO peak properties as  $n/n-1$  [269–275], but extends the range all the way to  $n = 4$ . Relative peak height demonstrated an almost monotonic increase with particle size with a diminishing slope for higher-order modes. The relative peak area showed the same overall trend as height, but less well-behaved. The relative peak width (FWHM) increased with a factor we quantified as 1.45(22) for each higher order step (so the 2LO modes were on average 45 % wider than the 1LO modes, and so on for 3LO/2LO and 4LO/3LO).

These results indicate a stronger electron–phonon coupling as particle size increases in the range from 10 nm to 150 nm.

Looking at the grid in figure 6.14b, what struck me was how this *shift* in LO mode centroid position clearly appeared to depend on particle size. For instance, if we “walk along a column”, it is quite apparent how the sloping marker increases in slope as we go down said column (except for the first, obviously, where the observed and expected Raman shift of the mode is the same by definition). There is also an increasing shift in centroid position happening as we go towards higher-order modes (“walk along a row”). So I set out to quantify this *shift* (delta) in Raman shift of the higher-order modes, which I chose to name the *LO–LO shift*.

The precise value of this LO–LO shift will depend on whether we perform the analysis vs. particle size (figure 6.14c, note that in the case of LO–LO shift vs.  $d$  I chose to average the tree 10 nm samples) or vs. annealing temperature (FIG. S15 of PAPER IV). In either case, the shift is small, on the order of  $\mu\text{eV}$  per nm or  $^\circ\text{C}$ .



## 7. Summary and outlook

In this work we have investigated all-inorganic semiconductor photocatalysts for solar hydrogen evolution or photocatalytic water purification. The projected growth in demand for both energy and freshwater places a responsibility on science to come up with solar-powered methods to fill these needs, which will be crucial to achieve the renewable energy transition.

We have demonstrated a simple and cheap route to synthesize nanoscale arrays of core-shell ZnO/CdS on TCO glass substrates by combining electrodeposition (in the first step) and chemical bath deposition. These inorganic-sensitized ZnO nanorods showed a much stronger sensitivity to visible light than ZnO-only nanorods (as measured in both PC and PEC experiments), demonstrating that the ZnO/CdS interface successfully separated the photo-generated charge carriers across it. Varying durations of CBD were tested, and  $t_{\text{CBD}} = 40$  min was found to yield the best balance between deposited CdS vs. etched ZnO and PEC performance. These results indicate that such ZnO/CdS nanoarrays could be used as the basis for the photoanode in cheap and easily fabricated solar-energy conversion devices, given further optimization of the system.

We coated electrodeposited ZnO nanoarrays with an ultrathin, conformal layer of Fe<sub>2</sub>O<sub>3</sub> using ALD which protected the ZnO core from photocorrosion under all but very intense illumination. Although GI-XRD did not yield a conclusive phase determination of the ultrathin iron oxide film, a Raman investigation demonstrated the deposition of hematite. The PC activity of the samples were evaluated using EBT dye under a blue lamp and found to be marginally better than the uncoated sample.

The optical and photocatalytic properties of ZnO QD suspensions in the quantum-confined regime ( $d < 9$  nm) were studied *in situ* in a system targeted towards distributed pollutants, here modelled by MB dye. Particle sizes from 3.2 nm to 6 nm were found to effectively photodegrade MB under AM1.5G irradiation, almost completely photo-oxidising MB. Larger particles ( $d > 6$  nm) caused a lesser degree of photo-oxidation, and also promoted a competing photo-reduction process, which was not observed for the smaller QDs. The fact that the PC particles clearly aggregated and sedimented as they degraded the pollutant made us envision using such nanoparticulate PCs as a low-cost, low-toxicity method to aid in the remediation of distributed environmental threats.

We have presented a comprehensive investigation of the first and second order Raman processes in nanoscale ZnO crystalline powders with particle size ranging from 10 nm to 150 nm using two different visible laser excitation

## 7. Summary and outlook

sources, allowing us to assign all the observed phonon modes including higher-order sum or diff modes, which we also compared to density functional theory predictions. The phonon–phonon coupling increased with particle size, but the LO–TO split remained constant over the same size range. We also quantified the electron–phonon coupling of the ZnO nanocrystal sample by carefully analysing the resonant Raman spectra (up to the 4th overtone) with regard to mode position, width, and height.

In general, our methods of fabrication have not been overly specialized nor expensive, which makes them applicable to a wide range of PC materials. By characterizing the optical, electronic, and thermal properties of the proposed PCs we have contributed data of technical interest for the design of novel, sustainable photocatalysts.

For the future, we anticipate that similar approaches can be used for adjacent material systems utilized alone, or in combination with ZnO for applications within catalysis. It would for example be interesting to utilize the tuning of the CB in ZnO to target and optimize potential-dependent reactions such as the creation of C1 (one-carbon) and C2 (two-carbon) species from the CO<sub>2</sub> reduction.

## 8. Populärvetenskaplig sammanfattning

Världen har byggt upp ett industriellt system som har gjort sig helt beroende av ett ständigt ökande flöde av fossil olja och gas, både som energikälla och som råvara. Detta trots att vetenskapen i över 100 år varnat för de globala klimatförändringar som vore följden av att släppa ut dessa enorma mängder uråldrigt kol i atmosfären. Industrialiseringen har dessutom lett till utbredd miljöförstöring, i form av föroreningar av vatten och luft.

Ett viktigt steg för att inom en snar framtid helt avveckla samhällets beroende av fossilbränslen är den pågående elektrifieringen, som för närvarande är mest synlig inom transportsektorn (med elbilar och så vidare). Men för vissa sektorer, till exempel kemisk industri, räcker inte elektrifiering för att åstadkomma den gröna omställningen – de behöver *förnybara bränslen*. Samtidigt behöver vi och många andra länder hantera miljöföroreningar på ett bättre och billigare sätt än dagens metoder som mest skyfflar föroreningarna från en plats till en annan (eller ett land till ett annat).

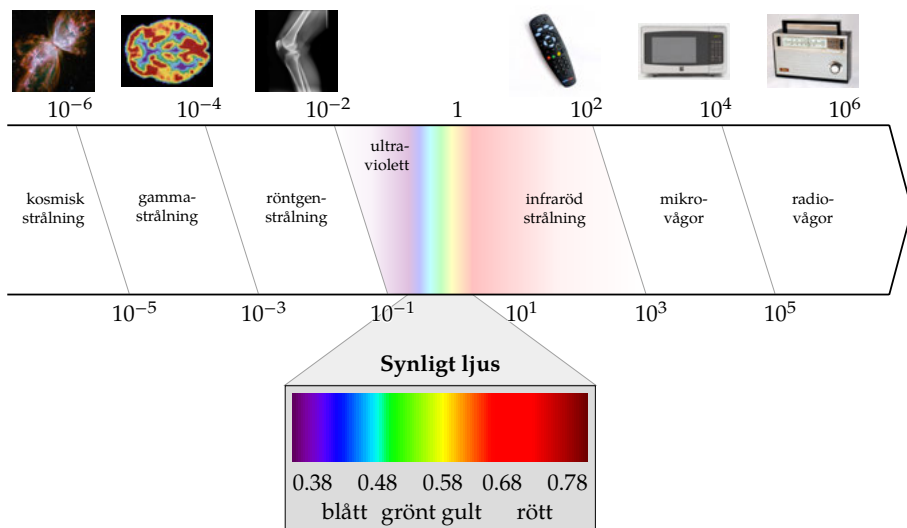
För att finna metoder att lösa dess problem behöver vi bara titta upp. I solljus har vi energi som kan omvandlas direkt till elektricitet (solceller uppfanns redan på 50-talet och är idag världens mest kostnadseffektiva elkälla) eller med hjälp av halvledande kristallina material kan driva den kemiska reaktionen av energifattiga kemikalier (t.ex. vatten,  $\text{H}_2\text{O}$ ) till energirika kemikalier som vätgas,  $\text{H}_2$ , så kallad *soldriven vattensplittring*. Solljus kan också utnyttjas, med hjälp av andra halvledande kristallina material, för att bryta ner föroreningar (oftast kolbaserade kemikalier) i en process som kallas *soldriven fotokatalys*.

Som du säkert lagt märke till har både vattensplittring och fotokatalys en sak gemensamt: de kan katalyseras av halvledande material. Halvledare är material som är varken bra eller dåliga på att leda elektricitet, och detta beror på att de har ett så kallat *bandgap* mellan ett ledande och ett icke-ledande elektroniskt tillstånd. Ett halvledande materials ledningsförmåga kan kontrolleras med en extern elektrisk spänning, eller med belysning (beroende på ljusets färg), eller med temperatur och några andra sätt.

Halvledande material är intressanta som fotokatalysatorer på grund av att vi kan anpassa storleken på deras bandgap genom valet av material (inklusive dopning) eller till och med genom att kontrollera materialets partikelstorlek, vilket är något jag utforskat för zinkoxid ( $\text{ZnO}$ ) i denna avhandling. Bandgapets storlek avgör materialets optiska och elektroniska egenskaper, båda viktiga parametrar för att optimera soldriven vattensplittring eller soldriven fotokatalys.

För att använda en liknelse kan bandgapet i en halvledare liknas vid en höjdhoppsribba, och ljuset (fotoner) som faller på materialet som höjdhoppare med olika mycket "studs i benen". Fotoner med kort våglängd har mycket

## 8. Populärvetenskaplig sammanfattning

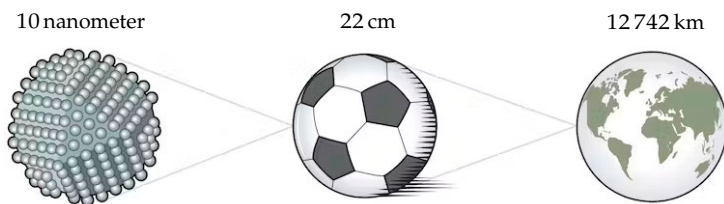


*Figur 8.1.* Det elektromagnetiska spektrat, med våglängder angivna i mikrometer (en  $\mu\text{m}$  är en hundra delar mm). I illustrationen kan ses att skillnaden mellan blått ljus och rött ljus är ungefär  $0.3 \mu\text{m}$ . Solen utstrålar alla möjliga våglängder, även med kortare eller längre våglängd än vad som visas här. Räknat som frekvensintervall omfattar det synliga ljuset bara en tiondel av det elektromagnetiska spektrat, men mätt som intensitet är en överväldigande majoritet av solens utstrålning synligt ljus. Bildkällor (från vänster till höger): planetarisk nebulosa NGC 6302 ("fjärilsnebulosan") i stjärnbilden Skorpionen, © NASA; PET-bild av mänsklig hjärna, © OpenStax; röntgenbild av mänskligt knä, © Wikimedia Commons; fjärrkontroll, av Priyanshu Kumar (Unsplash); mikrovågsugn, © Consumer Reports; AM radio, © Joe Haupt.

energi och kan enkelt hoppa över även högt lagda ribbor, medan fotoner med lång våglängd har lite energi och bara klarar lågt lagda ribbor. Varje foton som tar sig över ribban *absorberas* av materialet och kan sedan omvandlas till en elektron och ett hål. Fotoner som inte kan ta sig över ribban kan inte heller absorberas och går till spillo. Det är därför viktigt att anpassa bandgapet till det ljus som kommer att falla på fotokatalysatorn. Detta ställer väldigt olika krav på materialet beroende på om det ska drivas av naturligt solljus eller en artificiell ljuskälla (ljus är elektromagnetisk strålning, se fig. 8.1).

Genom att anpassa storleken på ZnO nanopartiklar eller kvantprickar, kan vi kontrollera bandgapets storlek inom vissa gränser, och därmed förutbestämma vilka våglängder av ljus som kommer absorberas av materialet.

ZnO är en vanligt förekommande halvledare (produceras några miljoner ton per år, främst för användning inom däcktillverkning) och ett välkänt fotokatalytiskt material med ett stort bandgap som bara kan absorbera UV-ljus (inget synligt ljus kan absorberas, och ZnO har följaktligen vit färg). Detta innebär att odopad ZnO inte kommer på fråga för soldriven vattensplittring, men ur katalytisk synvinkel kan dess stora bandgap vara fördelaktigt för att



Figur 8.2. Partiklar mindre än 100 nanometer kallas *nanopartiklar*. Nanopartiklarnas värld är mycket, mycket liten. Förhållandet i storlek mellan en fotboll och jorden är nästan precis samma som mellan en nanopartikel och en fotboll. Så om du kunde förminska dig till nano-storlek, skulle en vanlig fotboll vara lika stor för dig som en planet är för oss andra. Måtten avser diameter. ©©© Nobelstiftelsen.

generera högre redox-potentialer, särskilt i kombination med större ytareal via nanostrukturering.

I den här avhandlingen har jag tillverkat nanostrukturerade filmer av ZnO för sig självt eller i kombination med CdS eller  $\text{Fe}_2\text{O}_3$ , och undersökt dessa films egenskaper med hjälp av olika metoder såsom röntgendiffraktometri, UV-Vis spektrofotometri, elektronmikroskopi, röntgenfluorescens, med flera.

Jag syntetiserade kvantprickar av ZnO och övervakade deras fotokatalytiska verkan under simulerat AM1.5G solljus samtidigt som bandgapets storlek förändrades.

Jag utförde även fundamentala undersökningar av kristallvibrationer (fononer) och fonon-fonon- samt elektron-fonon-kopplingar i ZnO nanopartiklar.

Nanopartiklar ger material helt nya kemiska egenskaper enbart på grund av deras storlek. Det handlar om partiklar som är mindre än 100 nm i diameter (se fig. 8.2). Som jämförelse får ungefär 10 atomer på rad plats på en nanometer, och ett hårstrå är cirka 50 000 nm i diameter. Tillverkning av nanomaterial är som kemiskt finsnickeri; rena atomslöjden.

Det kan finnas risker med nanotekniken. Vi måste beakta att partiklarnas själva litenhet kan öka risken att de tas upp av lungorna eller till och med genom huden, alldeles oavsett om materialet ifråga är giftigt när det inte är nanostrukturerat. Vi behöver vara respektfulla inför att vi ännu kan för lite om riskerna, men samtidigt ska vi inte vara onödigt rädda. Nanopartiklar bildas helt naturligt vid många olika processer, till exempel när du tänder eld på en tändsticka. Dessutom har de flesta användningsområden inget behov av lösa nanopartiklar, utan de är vanligtvis inneslutna i en film eller i en lösning av något slag (t.ex. innehåller flera nya TV-skärmar kvantprickar, "quantum dots", för rikare färgåtergivning).

Denna avhandling har studerat en-dimensionella nanostrukturer av ZnO belagda med olika tjocka filmer av CdS och funnit att sulfidfilmen ger kompositmaterialet markant förbättrad optisk absorption i det synliga våglängdsområdet, och att denna effekt visar ett beroende på sulfidfilmens tjocklek. De olika energinivåerna för valens- och ledningsbandkanterna i oxid- respektive sul-

## 8. Populärvetenskaplig sammanfattning

fidfilmen gav också en observerbar laddningsseparation av de fotogenererade laddningsbärarna.

Denna avhandling har visat att 1D nanostrukturer av ZnO kan beläggas med nanofilmer av  $\text{Fe}_2\text{O}_3$  som effektivt skyddar materialet mot fotokorrosion, men de tunnaste filmerna har sannolikt låg kristallinitet vilket försämrade deras fotokatalytiska förmåga.





Vi har visat att kvantpunkter av ZnO kan användas för att effektivt bryta ner distribuerade miljöföroreningar med hjälp av solljus, och observerat hur redox-kemin ändrat sig för olika diameter på kvantprickarna.

För nanostrukturerade ZnO pulver med partikelstorlekar i intervallet 10 nm till 150 nm undersökte vi deras fundamentala kristallvibrationer inklusive flera övertoner samt kopplingen mellan elektroniska och vibrationella moder i materialet.









I denna avhandling har ZnO tillverkats i storlekar från 3 nm till över 100 nm och studerats med avseende på dess elektroniska, optiska och vibrationella egenskaper, samt i flera fall har deras förmåga att verka fotokatalytiskt undersökts.

Förutom att öka den fundamentala förståelsen för materialet i sig har denna avhandling även bidragit med praktiskt användbar information och vägledning om vilka ändringar i främst partikelstorlek som ger optimerad fotofysik för soldriven vattensplittring och soldriven fotokatalys.

# Acknowledgements

I am very thankful for the unwavering support from my advisors Tomas  and Jiefang ; without your help I would never have started on this endeavour, and certainly not finished it. Thank you for freely sharing your time and experience with me, and for giving me space to pursue my own ideas at other times. I would like to thank Mats Boman for taking on the mantle of assistant advisor at a time when the going was rough for me: thank you for helping steady my boat. And to Kristina  and Torbjörn : I will never forget your kindness that day at café Fågelsången.


I could not be here without the work of my co-authors: I thank you all for your invaluable research contributions. My gratitude to all the research groups at the Ångström laboratory who gracefully allowed me the use of their instruments for my research.

I would like to thank all current and past members of the Edvinsson group, including Ilknur , Jakob , Rafael, Mustafa, Bitao, Robin , Carlos, and Zhen . It has been delightful. I would also like to thank Jesper  for his collegiality and for sharing his MATLAB scripts with me; Delphine Lebrun, for pleasant discussions and for giving me the push to start that R course; Daniel Hedlund , for reviewing that manuscript; Mario , for always offering encouraging words or advice; Mikaela , for helping me save an old dataset from bitrot; Jonas Högström, for showing by example that a L<sup>A</sup>T<sub>E</sub>X thesis was doable; and Pierre Sandin, for being an excellent research student. I suppose the expression “it takes a village to...” certainly applies to raising a PhD—I have definitely benefitted from the guidance and inspiration from far too many people to thank them here by name—please know that I extend my earnest gratitude to you all.

I offer my deepest appreciation to the research groups in structural chemistry, inorganic chemistry, and theoretical chemistry for fostering an academic environment conducive to learning and growth. I would like to express my gratitude to the stellar technical staff, current and former, at both the departments of chemistry and engineering. Without your support and expertise many of my experiments would never have been realized. And how could I forget to acknowledge our kind and supportive administrative staff, in particular I would like to thank Eva Larsson for always lending a kind ear.

During this PhD I have had the pleasure to get to know many other PhD candidates through my stints as an elected member in the TekNat faculty doctoral council (TNDR) and later the university doctoral board (DN); I wish all of you the best and hope we will get the chance to meet again in the future.

## Acknowledgements

If you will allow me a moment to reminisce; I would like to thank Hans Adolfsson  for teaching me about chirality and introducing me to chemistry research when I was but a highschool student. I still remember your bottles of limonene. Thanks also to my highschool teachers in chemistry and physics, who as it happened both held PhDs, for encouraging me and so many of my cohort to pursue a path of seeking knowledge.

Thanks to the futsal organizers at the physics department and to all the players over the years, it was fun while it lasted! My thanks to the Uppsala Linux user group and Cykelfrämjandet for organising worthwhile extracurricular activities, and to the indefatigable cadre of instructors at Campus1477. And where would I have been without the help of kind strangers online, whether on the T<sub>E</sub>X and R StackExchange forums or elsewhere on the web.

Thank you all, and keep up the good work! Every bit matters.



## References

- [1] Liz Allen et al. "Publishing: Credit where credit is due". In: *Nature* 508.7496 (2014), pp. 312–313. [doi](#)
- [2] Vincent Larivière, David Pontille, and Cassidy R. Sugimoto. "Investigating the division of scientific labor using the Contributor Roles Taxonomy (CRediT)". In: *Quantitative Science Studies* 2.1 (2021), pp. 111–128. [doi](#)
- [3] Marcia K. McNutt et al. "Transparency in authors' contributions and responsibilities to promote integrity in scientific publication". In: *Proceedings of the National Academy of Sciences* 115.11 (2018), pp. 2557–2560. [doi](#)
- [4] S. E. Braslavsky. "Glossary of terms used in photochemistry, 3rd edition (IUPAC recommendations 2006)". In: *Pure and Applied Chemistry* 79.3 (2007), pp. 293–465. [doi](#)
- [5] E. Richard Cohen et al. *Quantities, units and symbols in physical chemistry: IUPAC green book*. 3rd ed. Cambridge: IUPAC & RSC Publishing, 2008. 250 pp. [ORCID](#)
- [6] IUPAC. *Compendium of chemical terminology: IUPAC gold book*. IUPAC, 2012.
- [7] J. W. Verhoeven. "Glossary of terms used in photochemistry (IUPAC recommendations 1996)". In: *Pure and Applied Chemistry* 68.12 (1996), pp. 2223–2286. [doi](#)
- [8] Tomas Edvinsson. "Optical quantum confinement and photocatalytic properties in two-, one- and zero-dimensional nanostructures". In: *Royal Society Open Science* 5.9 (2018), p. 180387. [doi](#)
- [9] Grzegorz Greczynski et al. "X-ray photoelectron spectroscopy of thin films". In: *Nature Reviews Methods Primers* 3.1 (1 2023), pp. 1–19. [doi](#)
- [10] Daniel Giovannini et al. "Spatially structured photons that travel in free space slower than the speed of light". In: *Science* 347.6224 (2015), pp. 857–860. [doi](#)
- [11] Antoine Kahn. "Fermi level, work function and vacuum level". In: *Materials Horizons* 1.1 (2015). [doi](#)
- [12] S. Trasatti. "The absolute electrode potential: an explanatory note (Recommendations 1986)". In: *Pure and Applied Chemistry* 58.7 (1986), pp. 955–966. [doi](#)
- [13] Eric D. Schneider and Dorion Sagan. *Into the cool: energy flow, thermodynamics, and life*. Chicago: University of Chicago Press, 2005.

## REFERENCES

- [14] John Perlin. *Let it shine: the 6000-year story of solar energy*. Novato, California: New World Library, 2013.
- [15] Svante Arrhenius. "XXXI. On the influence of carbonic acid in the air upon the temperature of the ground". In: *The London, Edinburgh, and Dublin Philosophical Magazine and Journal of Science* 41.251 (1896), pp. 237–276. [doi](#)
- [16] John Tyndall. "I. The Bakerian Lecture.—On the absorption and radiation of heat by gases and vapours, and on the physical connexion of radiation, absorption, and conduction". In: *Philosophical Transactions of the Royal Society of London* 151 (1861), pp. 1–36. [doi](#)
- [17] Roland Jackson. "Eunice Foote, John Tyndall and a question of priority". In: *Notes and Records: the Royal Society Journal of the History of Science* 74.1 (2019), pp. 105–118. [doi](#)
- [18] J. J. Thomson. "XL. Cathode rays". In: *The London, Edinburgh, and Dublin Philosophical Magazine and Journal of Science* 44.269 (1897), pp. 293–316. [doi](#)
- [19] Marc Hudson. "Climate change first "went viral" exactly 70 years ago". In: *The Conversation* (2023). [🔗](#)
- [20] William D. Nordhaus and James Tobin. "Is growth obsolete?" In: *Economic research: retrospect and prospect*. Vol. 5. Economic growth. National Bureau of Economic Research, 1972. [🔗](#)
- [21] William D. Nordhaus. *Managing the global commons: the economics of climate change*. Cambridge, Mass.: MIT, 1994.
- [22] IRENA. *A new world: the geopolitics of the energy transformation*. 2019. [🔗](#)
- [23] Linn Persson et al. "Outside the safe operating space of the planetary boundary for novel entities". In: *Environmental Science & Technology* 56.3 (2022), pp. 1510–1521. [doi](#)
- [24] Donella H. Meadows et al. *The limits to growth*. Universe Books, 1972.
- [25] Richard Wolfson. *Energy, environment, and climate*. 3rd ed. W. W. Norton & Company, 2018.
- [26] J. B. S. Haldane. *Daedalus or science and the future*. New York: E. P. Kutton & Company, 1923.
- [27] Krishnan Rajeshwar, Robert McConnell, and Stuart Licht. *Solar hydrogen generation: toward a renewable energy future*. Ed. by Krishnan Rajeshwar, Robert McConnell, and Stuart Licht. Springer, 2008.
- [28] Andreas Roos. "Renewing power: Including global asymmetries within the system boundaries of solar photovoltaic technology". Lund University, 2021. [🔗](#)
- [29] United Nations World Water Assessment Programme. *The United Nations world water development report 2020*. Paris: United Nations Educational, Scientific and Cultural Organization, 2020. [🔗](#)

- [30] Wendy Wilson, Travis Leipzig, and Bevan Griffiths-Sattenspiel. *Burning our rivers: The water footprint of electricity*. River Network, 2012. [ORCID](#)
- [31] Wenbin Wang et al. "Simultaneous production of fresh water and electricity via multistage solar photovoltaic membrane distillation". In: *Nature Communications* 10.1 (2019), p. 3012. [DOI](#)
- [32] Math Bollen and Fainan Hassan. *Integration of distributed generation in the power system*. Ed. by Mohamed E. El-Hawary. Institute of Electrical and Electronics Engineers, 2011. [DOI](#)
- [33] Torben Nilsson Pingel et al. "Influence of atomic site-specific strain on catalytic activity of supported nanoparticles". In: *Nature Communications* 9.1 (1 2018), p. 2722. [DOI](#)
- [34] Zhen Ma and Francisco Zaera. "Heterogeneous catalysis by metals". In: *Encyclopedia of inorganic chemistry*. Wiley, 2005. [DOI](#)
- [35] Andrew Mills and Stephen Le Hunte. "An overview of semiconductor photocatalysis". In: *Journal of Photochemistry and Photobiology A: Chemistry* 108.1 (1997), pp. 1–35. [DOI](#)
- [36] P. Suppan. *Chemistry and light*. The Royal Society of Chemistry, 1994. [DOI](#)
- [37] A. Akyol, H. C. Yatmaz, and M. Bayramoglu. "Photocatalytic decolorization of Remazol Red RR in aqueous ZnO suspensions". In: *Applied Catalysis B: Environmental* 54.1 (2004), pp. 19–24. [DOI](#)
- [38] Krishnan Rajeshwar, Abegayl Thomas, and Csaba Janáky. "Photocatalytic activity of inorganic semiconductor surfaces: myths, hype, and reality". In: *Journal of Physical Chemistry Letters* 6.1 (2015), pp. 139–147. [DOI](#)
- [39] Jiefang Zhu, Dinko Chakarov, and Michael Zäch. "Nanostructured materials for photolytic hydrogen production". In: *Energy Efficiency and Renewable Energy Through Nanotechnology*. Ed. by Ling Zang. London: Springer London, 2011. [DOI](#)
- [40] Kazuhiko Maeda. "Photocatalytic water splitting using semiconductor particles: History and recent developments". In: *Journal of Photochemistry and Photobiology C: Photochemistry Reviews* 12.4 (2011), pp. 237–268. [DOI](#)
- [41] Peter C. K. Vesborg and Thomas F. Jaramillo. "Addressing the terawatt challenge: scalability in the supply of chemical elements for renewable energy". In: *RSC Advances* 2.21 (2012), pp. 7933–7947. [DOI](#)
- [42] A. von Eibner. "Über Lichtwirkungen auf Malerfarbstoffe. I." In: *Chemiker-Zeitung* 35.82 (1911), pp. 753–755.
- [43] Maria C. Markham and Keith J. Laidler. "A kinetic study of photo-oxidations on the surface of zinc oxide in aqueous suspensions". In: *The Journal of Physical Chemistry* 57.3 (1953), pp. 363–369. [DOI](#)
- [44] Sister Clare Markham. "Photocatalytic properties of oxides". In: *Journal of Chemical Education* 32.10 (1955), p. 540. [DOI](#)

## REFERENCES

- [45] Gerrit Boschloo, Tomas Edvinsson, and Anders Hagfeldt. "Dye-sensitized nanostructured ZnO electrodes for solar cell applications". In: *Nanostructured materials for solar energy conversion*. Ed. by Tetsuo Soga. Elsevier, 2006, pp. 227–254. [doi](#)
- [46] Jesper Tor Jacobsson and Tomas Edvinsson. "Photoelectrochemical determination of the absolute band edge positions as a function of particle size for ZnO quantum dots". In: *Journal of Physical Chemistry C* 116.29 (2012), pp. 15692–15701. [doi](#)
- [47] Pedro J. Aphalo. "The r4photobiology suite: spectral irradiance". In: *UV4Plants Bulletin* 2015.1 (1 2015), pp. 21–29. [doi](#)
- [48] Federico Montanarella and Maksym V. Kovalenko. "Three millennia of nanocrystals". In: *ACS Nano* 16.4 (2022), pp. 5085–5102. [doi](#)
- [49] H. D. Wolpert. "Optical filters in Nature". In: *Optics and Photonics News* 20.2 (2009), pp. 22–27.
- [50] Jamie Dunning et al. "How woodcocks produce the most brilliant white plumage patches among the birds". In: *Journal of The Royal Society Interface* 20.200 (2023), p. 20220920. [doi](#)
- [51] John Aitken. "On the number of dust particles in the atmosphere". In: *Nature* 37.957 (1888), pp. 428–430. [doi](#)
- [52] John Aitken. "On the number of dust particles in the atmosphere of certain places in Great Britain and on the continent, with remarks on the relation between the amount of dust and meteorological phenomena". In: *Proceedings of the Royal Society of Edinburgh* 17 (1891), pp. 193–254. [doi](#)
- [53] Joachim Schummer. "On the novelty of nanotechnology: a philosophical essay". In: *In pursuit of nanoethics*. Ed. by Mark Cutter and Bert Gordijn. Springer, 2008, pp. 1–11.
- [54] Stephanie L. Mitchell et al. "Chronic exposure to complex metal oxide nanoparticles elicits rapid resistance in *Shewanella oneidensis* MR-1". In: *Chemical Science* (2019). [doi](#)
- [55] Sung Eun Kim et al. "Ultrasmall nanoparticles induce ferroptosis in nutrient-deprived cancer cells and suppress tumour growth". In: *Nature Nanotechnology* 11.11 (2016), pp. 977–985. [doi](#)
- [56] Robert B. Reed et al. "Solubility of nano-zinc oxide in environmentally and biologically important matrices". In: *Environmental Toxicology and Chemistry* 31.1 (2012), pp. 93–99. [doi](#)
- [57] Andrew D. Maynard, David B. Warheit, and Martin A. Philbert. "The new toxicology of sophisticated materials: nanotoxicology and beyond". In: *Toxicological Sciences* 120 (SUPPL.1 2011), S109–S129. [doi](#)
- [58] Andrew D. Maynard. "Learning from the past". In: *Nature Nanotechnology* 10 (2015), pp. 482–483. [doi](#)

- [59] Emily S Bernhardt, Emma J Rosi, and Mark O Gessner. "Synthetic chemicals as agents of global change". In: *Frontiers in Ecology and the Environment* 15.2 (2017), pp. 84–90. [doi](#)
- [60] Naturvårdsverket. *Avancerad rening av avloppsvatten för avskiljning av läkemedelsrester och andra oönskade ämnen: behov, teknik och konsekvenser*. 6766. Stockholm: Naturvårdsverket, 2017, p. 86. [doi](#)
- [61] S. J. Limmer et al. "Electrophoretic growth of lead zirconate titanate nanorods". In: *Advanced Materials* 13.16 (2001), pp. 1269–1272. [doi](#)
- [62] S.J. Limmer et al. "Template-based growth of various oxide nanorods by sol-gel electrophoresis". In: *Advanced Functional Materials* 12.1 (2002), p. 59. [doi](#)
- [63] S.Z. Chu et al. "Fabrication and characteristics of nanostructures on glass by Al anodization and electrodeposition". In: *Electrochimica Acta* 48.20-22 (2003), pp. 3147–3153. [doi](#)
- [64] Song-Zhu Chu et al. "Fabrication and structural characteristics of ordered  $\text{TiO}_2$ -Ru(-RuO<sub>2</sub>) nanorods in porous anodic alumina films on ITO/glass substrate". In: *The Journal of Physical Chemistry B* 107.37 (2003), pp. 10180–10184. [doi](#)
- [65] Steven J Limmer, Timothy L Hubler, and Guozhong Cao. "Nanorods of various oxides and hierarchically structured mesoporous silica by sol-gel electrophoresis". In: *Journal of Sol-Gel Science and Technology* 26.1-3 (2003), pp. 577–581. [doi](#)
- [66] S. J. Limmer, T. P. Chou, and G. Z. Cao. "A study on the growth of  $\text{TiO}_2$  nanorods using sol electrophoresis". In: *Journal of Materials Science* 39.3 (2004), pp. 895–901. [doi](#)
- [67] S. Z. Chu et al. "Fabrication of  $\text{TiO}_2$ -Ru(O<sub>2</sub>)/ $\text{Al}_2\text{O}_3$  composite nanostructures on glass by Al anodization and electrodeposition". In: *Journal of The Electrochemical Society* 151.1 (2004), p. C38. [doi](#)
- [68] S J Limmer, T P Chou, and G Z Cao. "A study on the influences of processing parameters on the growth of oxide nanorod arrays by sol electrophoretic deposition". In: *Journal of Sol-Gel Science and Technology* 36.2 (2005), pp. 183–195. [doi](#)
- [69] Hongwei Yan et al. "Cathodic electrodeposition of ordered porous titania films by polystyrene colloidal crystal templating". In: *Chemistry Letters* 35.8 (2006), pp. 864–865. [doi](#)
- [70] C. Natarajan and G. Nogami. "Cathodic electrodeposition of nanocrystalline titanium dioxide thin films". In: *Journal of The Electrochemical Society* 143.5 (1996), p. 1547. [doi](#)
- [71] Subbian Karuppuchamy et al. "Cathodic electrodeposition of  $\text{TiO}_2$  thin films for dye-sensitized photoelectrochemical applications". In: *Chemistry Letters* 30.1 (2001), pp. 78–79. [doi](#)

## REFERENCES

- [72] C. R. Chenthamarakshan et al. "Immobilizing semiconductor particles by occlusion electrosynthesis in an oxide film matrix: the titania model case". In: *Electrochemistry Communications* 4.11 (2002), pp. 871–876. [doi](#)
- [73] S. Karuppuchamy et al. "Cathodic electrodeposition of oxide semiconductor thin films and their application to dye-sensitized solar cells". In: *Solid State Ionics* 151.1-4 (2002), pp. 19–27. [doi](#)
- [74] Norma R. de Tacconi et al. "Pulsed electrodeposition of  $\text{WO}_3\text{-TiO}_2$  composite films". In: *Electrochemistry Communications* 5.3 (2003), pp. 220–224. [doi](#)
- [75] Norma R. de Tacconi et al. "Composite  $\text{WO}_3\text{-TiO}_2$  films prepared by pulsed electrodeposition: Morphological aspects and electrochromic behavior". In: *Journal of Electroanalytical Chemistry* 566.2 (2004), pp. 249–256. [doi](#)
- [76] Norma R. de Tacconi et al. "Selenium-modified titanium dioxide photochemical diode/electrolyte junctions: photocatalytic and electrochemical preparation, characterization, and model simulations". In: *The Journal of Physical Chemistry B* 109.24 (2005), pp. 11953–11960. [doi](#)
- [77] S Karuppuchamy and J Jeong. "Super-hydrophilic amorphous titanium dioxide thin film deposited by cathodic electrodeposition". In: *Materials Chemistry and Physics* 93.2-3 (2005), pp. 251–254. [doi](#)
- [78] S Karuppuchamy, M Iwasaki, and H Minoura. "Electrochemical properties of electrosynthesized  $\text{TiO}_2$  thin films". In: *Applied Surface Science* 253 (2006), pp. 2924–2929. [doi](#)
- [79] S. Karuppuchamy et al. "Photoinduced hydrophilicity of titanium dioxide thin films prepared by cathodic electrodeposition". In: *Vacuum* 80.5 (2006), pp. 494–498. [doi](#)
- [80] Sashikala Somasundaram et al. "Composite  $\text{WO}_3\text{-TiO}_2$  films: Pulsed electrodeposition from a mixed bath versus sequential deposition from twin baths". In: *Electrochemistry Communications* 8.4 (2006), pp. 539–543. [doi](#)
- [81] S Karuppuchamy, M Iwasaki, and H Minoura. "Physico-chemical, photo-electrochemical and photocatalytic properties of electrodeposited nanocrystalline titanium dioxide thin films". In: *Vacuum* 81.5 (2007), pp. 708–712. [doi](#)
- [82] H. Chettah et al. "Electrosynthesis of  $\text{TiO}_2$  oxide film on ITO substrate and electrochemical comparative study of the oxide with its hydrated gel". In: *Ionics* 15.2 (2008), pp. 169–176. [doi](#)
- [83] Masaya Chigane et al. "Preparation of hollow titanium dioxide shell thin films by electrophoresis and electrolysis for dye-sensitized solar cells". In: *Electrochemical and Solid-State Letters* 12.5 (2009), E5–E8. [doi](#)

- [84] Zhixiong Zhou et al. "Electrochemical preparation of  $\text{TiO}_2/\text{SiO}_2$  composite film and its high activity toward the photoelectrocatalytic degradation of methyl orange". In: *Journal of Applied Electrochemistry* 39.10 (2009), pp. 1745–1753. [doi](#)
- [85] Ying Chen et al. "Templated electrochemical synthesis of titania nanopillars on conductive substrates". In: *Journal of The Electrochemical Society* 157.10 (2010), E155. [doi](#)
- [86] J. Elhajj et al. "Electrochemical fabrication of  $\text{TiO}_2$ -Au nanocomposites". In: *Journal of The Electrochemical Society* 157.1 (2010), p. D5. [doi](#)
- [87] Tomokazu Ohya et al. "Synthesis and characterization of halogen-free, transparent, aqueous colloidal titanate solutions from titanium alkoxide". In: *Chemistry of Materials* 14.7 (2002), pp. 3082–3089. [doi](#)
- [88] Seiichi Sawatani et al. "Electrodeposition of  $\text{TiO}_2$  thin film by anodic formation of titanate/benzoquinone hybrid". In: *Electrochemical and Solid-State Letters* 8.5 (2005), pp. C69–C71. [doi](#)
- [89] Katrin Wessels et al. "Highly porous  $\text{TiO}_2$  films from anodically deposited titanate hybrids and their photoelectrochemical and photocatalytic activity". In: *Microporous and Mesoporous Materials* 111.1-3 (2008), pp. 55–61. [doi](#)
- [90] Katrin Wessels et al. "Influence of calcination temperature on the photoelectrochemical and photocatalytic properties of porous  $\text{TiO}_2$  films electrodeposited from  $\text{Ti(IV)}$ -alkoxide solution". In: *The Journal of Physical Chemistry C* 112.39 (2008), pp. 15122–15128. [doi](#)
- [91] Robert Flood. "Determination of band edge energies for transparent nanocrystalline  $\text{TiO}_2$ -CdS sandwich electrodes prepared by electrodeposition". In: *Solar Energy Materials and Solar Cells* 39.1 (1995), pp. 83–98. [doi](#)
- [92] C. D. Lokhande et al. "Electrodeposition of  $\text{TiO}_2$  and  $\text{RuO}_2$  thin films for morphology-dependent applications". In: *Ultramicroscopy* 105.1-4 (2005), pp. 267–274. [doi](#)
- [93] Katrin Wessels et al. "Low-temperature preparation of crystalline nanoporous  $\text{TiO}_2$  films by surfactant-assisted anodic electrodeposition". In: *Electrochemical and Solid-State Letters* 9.6 (2006), pp. C93–C96. [doi](#)
- [94] Tsung-Yu Tsai and Shih-Yuan Lu. "A novel way of improving light harvesting in dye-sensitized solar cells – Electrodeposition of titania". In: *Electrochemistry Communications* 11.11 (2009), pp. 2180–2183. [doi](#)
- [95] Min Wu et al. "Improvement of dye-sensitized solar cell performance through electrodepositing a close-packed  $\text{TiO}_2$  film". In: *Journal of Solid State Electrochemistry* 14.5 (2009), pp. 857–863. [doi](#)
















## REFERENCES

- [96] Katrin Wessels, Michael Wark, and Torsten Oekermann. "Efficiency improvement of dye-sensitized solar cells based on electrodeposited TiO<sub>2</sub> films by low temperature post-treatment". In: *Electrochimica Acta* 55.22 (2010), pp. 6352–6357. [doi](#)
- [97] Mao-Sung Wu, Chen-Hsiu Tsai, and Tzu-Chien Wei. "Electrochemical formation of transparent nanostructured TiO<sub>2</sub> film as an effective bifunctional layer for dye-sensitized solar cells". In: *Chemical Communications* 47.10 (2011), p. 2871. [doi](#)
- [98] Sophie Peulon and Daniel Lincot. "Mechanistic study of cathodic electrodeposition of zinc oxide and zinc hydroxychloride films from oxygenated aqueous zinc chloride solutions". In: *Journal of The Electrochemical Society* 145.3 (1998), pp. 864–874. [doi](#)
- [99] Thierry Pauporté and I. Jirka. "A method for electrochemical growth of homogeneous nanocrystalline ZnO thin films at room temperature". In: *Electrochimica Acta* 54.28 (2009), pp. 7558–7564. [doi](#)
- [100] V. A. Karpina et al. "Zinc oxide - analogue of GaN with new perspective possibilities". In: *Crystal Research and Technology* 39.11 (2004), pp. 980–992. [doi](#)
- [101] Anderson Janotti and Chris G Van de Walle. "Fundamentals of zinc oxide as a semiconductor". In: *Reports on Progress in Physics* 72.12 (2009), p. 126501. [doi](#)
- [102] Hendrina Ellis, R. D. Harrison, and H. D. B. Jenkins, eds. *Book of Data*. Revised edition. Longman, 1984.
- [103] N. N. Greenwood and A. Earnshaw. *Chemistry of the elements*. 2nd ed. Butterworth–Heinemann, 1997.
- [104] Christian Ekberg and Paul L. Brown. *Hydrolysis of metal ions*. Wiley-VCH, 2016.
- [105] Walther Schwarzacher. "Electrodeposition: a technology for the future". In: *Interface* 250.6 (2006), pp. 32–35.
- [106] Morimasa Nagao and Saburo Watanabe. "Chemically deposited thick CdS films and their properties". In: *Japanese Journal of Applied Physics* 7.6 (1968), pp. 684–685. [doi](#)
- [107] M.T.S. Nair, P.K. Nair, and J. Campos. "Effect of bath temperature on the optoelectronic characteristics of chemically deposited CdS thin films". In: *Thin Solid Films* 161 (1988), pp. 21–34. [doi](#)
- [108] A. Mondal, T. Chaudhuri, and P. Pramanik. "Deposition of cadmium chalcogenide thin films by a solution growth technique using triethanolamine as a complexing agent". In: *Solar Energy Materials* 7.4 (1983), pp. 431–438. [doi](#)
- [109] Gary Hodes. *Chemical solution deposition of semiconductor films*. Food Science and Technology. New York: Marcel Dekker, Inc., 2003.



- [110] Youngjo Tak et al. "Solution-based synthesis of a CdS nanoparticle/ZnO nanowire heterostructure array". In: *Crystal Growth & Design* 9.6 (2009), pp. 2627–2632. [doi](#)
- [111] Raúl Ortega-Borges and Daniel Lincot. "Mechanism of chemical bath deposition of cadmium sulfide thin films in the ammonia-thiourea system: in situ kinetic study and modelization". In: *Journal of the Electrochemical Society* 140.12 (1993), p. 3464. [doi](#)
- [112] Isaiah O. Oladeji and Lee Chow. "Optimization of chemical bath deposited cadmium sulfide thin films". In: *Journal of The Electrochemical Society* 144.7 (1997), p. 2342. [doi](#)
- [113] Gary Hodes et al. "Three-dimensional quantum-size effect in chemically deposited cadmium selenide films". In: *Physical Review B* 36.8 (1987), pp. 4215–4221. [doi](#)
- [114] Inderjeet Kaur, D. K. Pandya, and K. L. Chopra. "Growth kinetics and polymorphism of chemically deposited CdS films". In: *Journal of The Electrochemical Society* 127.4 (1980), p. 943. [doi](#)
- [115] John H. Kennedy and Karl W. Frese. "Photooxidation of water at  $\alpha$ -Fe<sub>2</sub>O<sub>3</sub> electrodes". In: *Journal of The Electrochemical Society* 125.5 (1978), pp. 709–714. [doi](#)
- [116] Mattis Fondell. "Synthesis and characterisation of ultra thin film oxides for energy applications". PhD thesis. Uppsala: Uppsala university, 2014. [doi](#)
- [117] Mattis Fondell et al. "Optical quantum confinement in low dimensional hematite". In: *Journal of Materials Chemistry A* 2.10 (2014), p. 3352. [doi](#)
- [118] Lubomir Spanhel and Marc A. Anderson. "Semiconductor clusters in the sol-gel process: quantized aggregation, gelation, and crystal growth in concentrated zinc oxide colloids". In: *Journal of the American Chemical Society* 113.8 (1991), pp. 2826–2833. [doi](#)
- [119] P Hoyer, R Eichberger, and H Weller. "Spectroelectrochemical Investigations of Nanocrystalline ZnO Films". In: *Berichte der Bunsen-Gesellschaft fur physikalische Chemie* 97.4 (1993), pp. 630–635. [doi](#)
- [120] P Hoyer and H Weller. "Size-dependent redox potentials of quantized zinc oxide measured with an optically transparent thin layer electrode". In: *Chemical Physics Letters* 221.5-6 (1994), pp. 379–384. [doi](#)
- [121] Eric A. Meulenkaamp. "Synthesis and growth of ZnO nanoparticles". In: *Journal of Physical Chemistry B* 102.29 (1998), pp. 5566–5572. [doi](#)
- [122] John R. Rumble, ed. *CRC handbook of chemistry and physics*. 104th ed. Boca Raton: CRC Press, 2023. [doi](#)
- [123] Olaf Stenzel. *The physics of thin film optical spectra: an introduction*. Red. by G. Ertl, H. Lüth, D. L. Mills. Vol. 44. Springer Series in Surface Sciences. Berlin: Springer-Verlag, 2005.

## REFERENCES

- [124] O. S. Heavens. *Optical properties of thin solid films*. London: Butterworth scientific publications, 1955.
- [125] Sara Green. “Electrochromic nickel-tungsten oxides: optical, electrochemical and structural characterization of sputter-deposited thin films in the whole composition range”. PhD thesis. Uppsala university, 2012. 116 pp. 
- [126] Meysam Pazoki, Anders Hagfeldt, and Tomas Edvinsson, eds. *Characterization techniques for perovskite solar cell materials*. Micro and Nano Technologies. Elsevier, 2020. 
- [127] Paromita Kundu et al. “Nanoscale ZnO/CdS heterostructures with engineered interfaces for high photocatalytic activity under solar radiation”. In: *Journal of Materials Chemistry* 21.12 (2011), pp. 4209–4216. 
- [128] Mohammad Ziaur Rahman and Tomas Edvinsson. “X-ray diffraction and Raman spectroscopy for lead halide perovskites”. In: *Characterization techniques for perovskite solar cell materials*. Elsevier, 2020, pp. 23–47. 
- [129] R. Brian Dyer and William H. Woodruff. “Vibrational spectroscopy”. In: *Encyclopedia of inorganic chemistry*. Wiley, 2005. 
- [130] Adolf Smekal. “Zur Quantentheorie der Dispersion”. In: *Naturwissenschaften* 11.43 (1923), pp. 873–875. 
- [131] H. A. Kramers. “The quantum theory of dispersion”. In: *Nature* 114.2861 (2861 1924), pp. 310–311. 
- [132] H. A. Kramers. “The law of dispersion and Bohr’s theory of spectra”. In: *Nature* 113.2845 (2845 1924), pp. 673–674. 
- [133] H. A. Kramers and W. Heisenberg. “Über die Streuung von Strahlung durch Atome”. In: *Zeitschrift für Physik* 31.1 (1925), pp. 681–708. 
- [134] C. V. Raman. “On the molecular scattering of light in water and the colour of the sea”. In: *Proceedings of the Royal Society A: Mathematical, Physical and Engineering Sciences* 101.708 (1922), pp. 64–80. 
- [135] C. V. Raman and K. S. Krishnan. “A new type of secondary radiation”. In: *Nature* 121.3048 (3048 1928), pp. 501–502. 
- [136] C. V. Raman. “A change of wave-length in light scattering”. In: *Nature* 121.3051 (3051 1928), pp. 619–619. 
- [137] G. S. Landsberg and L. I. Mandelstam. “Eine neue Erscheinung bei der Lichtzerstreuung in Krystallen”. In: *Naturwissenschaften* 16.28 (1928), pp. 557–558. 
- [138] Gr. Landsberg and L. Mandelstam. “Über die Lichtzerstreuung in Kristallen”. In: *Zeitschrift für Physik* 50.11 (1928), pp. 769–780. 
- [139] M. Cardona. “Resonant Raman scattering in semiconductors”. In: *Elementary Excitations in Solids, Molecules, and Atom, Part B*. Boston, MA: Springer US, 1974, pp. 269–291. 

- [140] Robert S. Mulliken. "Report on notation for spectra of diatomic molecules". In: *Physical Review* 36.4 (1930), pp. 611–629. [doi](#)
- [141] Robert S. Mulliken. "Report on notation for the spectra of polyatomic molecules". In: *Journal of Chemical Physics* 23.11 (1955), p. 1997. [doi](#)
- [142] Robert S. Mulliken. "Erratum: Report on notation for the spectra of polyatomic molecules". In: *The Journal of Chemical Physics* 24.5 (1956), pp. 1118–1118. [doi](#)
- [143] Léon Brillouin. "Diffusion de la lumière et des rayons X par un corps transparent homogène: Influence de l'agitation thermique". In: *Annales de Physique* 9.17 (1922), pp. 88–122. [doi](#)
- [144] Jacques I. Pankove. *Optical processes in semiconductors*. New York: Dover Publications, Inc., 1975. 470 pp.
- [145] R. Loudon. "The Raman effect in crystals". In: *Advances in Physics* 13.52 (1964), pp. 423–482. [doi](#)
- [146] Ryosuke Senga et al. "Position and momentum mapping of vibrations in graphene nanostructures". In: *Nature* 573.7773 (7773 2019), pp. 247–250. [doi](#)
- [147] Zhen Qiu. "Transition metal-based electrocatalysts for alkaline water splitting and CO<sub>2</sub> reduction". PhD thesis. Uppsala university, 2019. [ORCID](#)
- [148] Michael A. Strosio and Mitra Dutta. *Phonons in nanostructures*. Cambridge University Press, 2005.
- [149] L. N. Ovander. "Resonance Raman scattering in crystals". In: *Soviet Physics Solid State* 4.6 (1962), p. 1081.
- [150] Manuel Cardona, ed. *Light scattering in solids I Introductory concepts*. 2nd ed. Vol. 8. Topics in Applied Physics. New York: Springer-Verlag, 1983. 357 pp.
- [151] P. L. Davies et al. "Residual-based localization and quantification of peaks in X-ray diffractograms". In: *The Annals of Applied Statistics* 2.3 (2008), pp. 861–886. [doi](#)
- [152] Edgar W. Woolard and G. M. Clemence. *Spherical astronomy*. Elsevier, 1966.
- [153] Min Peng et al. "Polymer-encapsulated halide perovskite color converters to overcome blue overshoot and cyan gap of white light-emitting diodes". In: *Advanced Functional Materials* 33.n/a (2023), p. 2300583. [doi](#)
- [154] Rajesh J. Tayade, Thillai Sivakumar Natarajan, and Hari C. Bajaj. "Photocatalytic degradation of methylene blue dye using ultraviolet light emitting diodes". In: *Industrial & Engineering Chemistry Research* 48.23 (2009), pp. 10262–10267. [doi](#)
- [155] Andrew Mills and Jishun Wang. "Photobleaching of methylene blue sensitised by TiO<sub>2</sub>: an ambiguous system?" In: *Journal of Photochemistry and Photobiology A: Chemistry* 127.1-3 (1999), pp. 123–134. [doi](#)

## REFERENCES

- [156] M. Knoll and E. Ruska. "Das Elektronenmikroskop". In: *Zeitschrift für Physik* 78.5 (1932), pp. 318–339. [doi](#)
- [157] M. Knoll and E. Ruska. "Beitrag zur geometrischen Elektronenoptik. I". In: *Annalen der Physik* 404.5 (1932), pp. 607–640. [doi](#)
- [158] M. Knoll and E. Ruska. "Beitrag zur geometrischen Elektronenoptik. II". In: *Annalen der Physik* 404.6 (1932), pp. 641–661. [doi](#)
- [159] David B. Williams and C. Barry Carter. *Transmission electron microscopy: a textbook for materials science*. Springer Science+Business Media, 1996.
- [160] Manfred von Ardenne. "Improvements in electron microscopes". British pat. 511204 (A). Manfred von Ardenne. 1939. [🔗](#)
- [161] Peter J. Goodhew, John Humphreys, and Richard Beanland. *Electron microscopy and analysis*. 3rd ed. London: Taylor & Francis, 2001. 251 pp.
- [162] Uwe Holzwarth and Neil Gibson. "The Scherrer equation versus the 'Debye-Scherrer equation'". In: *Nature Nanotechnology* 6.9 (2011), pp. 534–534. [doi](#)
- [163] Gregory J. McCarthy and Jean M. Welton. "X-ray diffraction data for SnO<sub>2</sub>. An illustration of the new powder data evaluation methods". In: *Powder Diffraction* 4 (1989), pp. 156–159.
- [164] Howard F. McMurdie et al. "Standard X-ray diffraction powder patterns from the JCPDS research associateship". In: *Powder Diffraction* 1.2 (1986), pp. 64–77.
- [165] A. Lessandro P. Avese, D. Avidé L. Evy, and Andreas H. Oser. "Cation distribution in synthetic zinc ferrite (Zn<sub>0.97</sub>Fe<sub>2.02</sub>O<sub>4</sub>) from in situ high-temperature neutron powder diffraction". In: *American Mineralogist* 85 (2000), pp. 1497–1502. [🔗](#)
- [166] Helmer Fjellvåg et al. "On the Crystallographic and Magnetic Structures of Nearly Stoichiometric Iron Monoxide". In: *Journal of Solid State Chemistry* 124.1 (1996), pp. 52–57. [doi](#)
- [167] H. E. Swanson et al. *Standard X-ray diffraction powder patterns: Section 5. Data for 80 substances*. National Bureau of Standards, 1967, p. 98. [🔗](#)
- [168] Marlene C. Morris et al. *Standard X-ray diffraction powder patterns: section 18 – data for 58 substances*. 1981, p. 114. [🔗](#)
- [169] U. Schwertmann and R. M. Cornell. *Iron oxides in the laboratory: preparation and characterization*. 2nd ed. Vol. 156. 5. Wiley-VCH, 2000. 369 pp.
- [170] R. M. Cornell and U. Schwertmann. *The iron oxides: Structure, properties, reactions, occurrences and uses*. 2nd ed. Wiley-VCH Verlag GmbH & Co., 2003. 3–527.
- [171] Albert Einstein. "Concerning an heuristic point of view toward the emission and transformation of light". In: *American Journal of Physics* 33.5 (1965), p. 367. [doi](#)

- [172] K. Siegbahn et al. “ESCA une spectroscopie d’électrons appliquée à l’étude de la structure des atomes, des molécules et des corps solides”. In: *Annales de Physique* 14.3 (3 1968), pp. 281–329. [doi](#)
- [173] Marcin Wojdyr. “Fityk: a general-purpose peak fitting program”. In: *Journal of Applied Crystallography* 43 (2010), pp. 1126–1128. [doi](#)
- [174] Freeman J. Dyson. *The Sun, the genome, and the Internet: tools of scientific revolution*. Oxford University Press, 2000.
- [175] Jay Hoffmann. *The web’s most important decision*. The history of the web. 2023. URL: <https://thehistoryoftheweb.com/postscript/the-webs-most-important-decision> (visited on 07/30/2023). [🔗](#)
- [176] Kungliga Biblioteket. *Proposal for National guidelines for open science*. 2023. URL: <https://www.kb.se/samverkan-och-utveckling/nationella-riktlinjer-for-oppen-vetenskap/forslag-till-riktlinjer.html> (visited on 10/03/2023). [🔗](#)
- [177] UNESCO. *Recommendation on open science*. CL/4381. Paris: United Nations Educational, Scientific and Cultural Organization, 2021. [🔗](#)
- [178] OECD. *OECD principles and guidelines for access to research data from public funding*. Paris: Organisation for economic co-operation and development, 2007. [doi](#)
- [179] Leah McEwen and Ian Bruno. “WorldFAIR Project (D3.1) Digital recommendations for Chemistry FAIR data policy and practice”. Version 1. In: (2023). In collab. with Fatima Mustafa et al. [doi](#)
- [180] Matthias Scheffler et al. “FAIR data enabling new horizons for materials research”. In: *Nature* 604.7907 (7907 2022), pp. 635–642. [doi](#)
- [181] Anna-Lena Lamprecht et al. “Towards FAIR principles for research software”. In: *Data Science* 3.1 (2020), pp. 37–59. [doi](#)
- [182] Kungliga Biblioteket. *Vetenskapliga publikationer och FAIR-principerna – Bedömningskriterier och metod för att kunna följa utvecklingen mot ett öppet vetenskapssystem*. 2019. URL: <https://openaccess.blogg.kb.se/2019/02/28/%e2%80%8bhur-blir-svensk-forskning-mer-tillganglig-och-ateranvandbar/> (visited on 03/28/2019). [🔗](#)
- [183] Mark D. Wilkinson et al. “The FAIR Guiding Principles for scientific data management and stewardship”. In: *Scientific Data* 3.1 (2016), p. 160018. [doi](#)
- [184] Christine L. Borgman and Philip E. Bourne. “Why it takes a village to manage and share data”. In: *Harvard Data Science Review* (2022). [doi](#)
- [185] Barend Mons. “Invest 5% of research funds in ensuring data are reusable”. In: *Nature* 578.7796 (7796 2020), pp. 491–491. [doi](#)
- [186] Michelle Barker et al. “Introducing the FAIR Principles for research software”. In: *Scientific Data* 9.1 (2022), p. 622. [doi](#)

## REFERENCES

- [187] Dylan G. E. Gomes et al. "Why don't we share data and code? Perceived barriers and benefits to public archiving practices". In: *Proceedings of the Royal Society B: Biological Sciences* 289.1987 (2022), p. 20221113. [doi](#)
- [188] *Code is science manifesto*. In collab. with Yo Yehudi et al. Version 1.0. 2019. [doi](#)
- [189] Jeffrey M. Perkel. "Five reasons why researchers should learn to love the command line". In: *Nature* 590.7844 (2021), pp. 173–174. [doi](#)
- [190] Robert Hanisch et al. "Stop squandering data: make units of measurement machine-readable". In: *Nature* 605.7909 (2022), pp. 222–224. [doi](#)
- [191] Jeremy Frey. "Digital representation of units of measure". In: *Chemistry International* 42.4 (2020), pp. 36–36. [doi](#)
- [192] CODATA task group on digital representation of units of measure et al. "Units of measure for humans and machines: making units clear for machine learning and beyond". In: (2020). [doi](#)
- [193] Hugh G. Gauch Jr. *Scientific method in practice*. New York: Cambridge University Press, 2003.
- [194] P. L. Davies et al. *R package "diffractometry"*. CRAN, 2010. [doi](#)
- [195] J. Tauc, R. Grigorovici, and A. Vancu. "Optical properties and electronic structure of amorphous germanium". In: *Physica Status Solidi* 15 (1966), pp. 627–637.
- [196] Brian D. Vezbickie et al. "Evaluation of the Tauc method for optical absorption edge determination: ZnO thin films as a model system". In: *physica status solidi (b)* 252.8 (2015), pp. 1700–1710. [doi](#)
- [197] María D. Hernández-Alonso et al. "Development of alternative photocatalysts to TiO<sub>2</sub>: Challenges and opportunities". In: *Energy & Environmental Science* 2.12 (2009), p. 1231. [doi](#)
- [198] Shelly Burnside et al. "Nanocrystalline mesoporous strontium titanate as photoelectrode material for photosensitized solar devices: increasing photovoltage through flatband potential engineering". In: *The Journal of Physical Chemistry B* 103.43 (1999), pp. 9328–9332. [doi](#)
- [199] Yasumichi Matsumoto. "Energy positions of oxide semiconductors and photocatalysis with iron complex oxides". In: *Journal of Solid State Chemistry* 126.2 (1996), pp. 227–234. [doi](#)
- [200] Nick Serpone. "Brief introductory remarks on heterogeneous photocatalysis". In: *Solar Energy Materials and Solar Cells* 38.1-4 (1995), pp. 369–379. [doi](#)
- [201] H. H. Kung et al. "Semiconducting oxide anodes in photoassisted electrolysis of water". In: *Journal of Applied Physics* 48.6 (1977), p. 2463. [doi](#)

- [202] Paul A. Kohl, Steven N. Frank, and Allen J. Bard. "Semiconductor electrodes XI. Behavior of n- and p-type single crystal semiconductors covered with thin n-TiO<sub>2</sub> films". In: *Journal of The Electrochemical Society* 124.2 (1977), p. 225. [doi](#)
- [203] Jeffrey M. Bolts and Mark S. Wrighton. "Correlation of photocurrent-voltage curves with flat-band potential for stable photoelectrodes for the photoelectrolysis of water". In: *The Journal of Physical Chemistry* 80.24 (1976), pp. 2641–2645. [doi](#)
- [204] W. H. Laflère, F. Cardon, and W. P. Gomes. "On the differential capacitance of the n- and p-type gallium arsenide electrode". In: *Surface Science* 44.2 (1974), pp. 541–552. [doi](#)
- [205] Akihiko Kudo and Yugo Miseki. "Heterogeneous photocatalyst materials for water splitting". In: *Chemical Society Reviews* 38.1 (2009), pp. 253–278. [doi](#)
- [206] Rufino M. Navarro Yerga et al. "Water splitting on semiconductor catalysts under visible-light irradiation". In: *ChemSusChem* 2.6 (2009), pp. 471–485. [doi](#)
- [207] Michael Grätzel. "Photoelectrochemical cells". In: *Nature* 414 (November 2001), pp. 338–344. [doi](#)
- [208] Amy L. Linsebigler, Guangquan Lu, and John T. Yates. "Photocatalysis on TiO<sub>2</sub> surfaces: principles, mechanisms, and selected results". In: *Chemical Reviews* 95.3 (1995), pp. 735–758. [doi](#)
- [209] Arthur J. Nozik. "Photoelectrochemistry: applications to solar energy conversion". In: *Annual Review of Physical Chemistry* 29.1 (1978), pp. 189–222. [doi](#)
- [210] M. Gleria and R. Memming. "Charge transfer processes at large band gap semiconductor electrodes: Reactions at SiC-electrodes". In: *Journal of Electroanalytical Chemistry* 65.1 (1975), pp. 163–175. [doi](#)
- [211] R. J. Dwayne Miller and Rüdiger Memming. "Fundamentals in photoelectrochemistry". In: *Nanostructured and Photoelectrochemical Systems for Solar Photon Conversion*. Ed. by Mary D. Archer and Arthur J. Nozik. Vol. 3. Series on Photoconversion of Solar Energy. Imperial College Press, 2008, pp. 39–145. [doi](#)
- [212] S. Roy Morrison. *Electrochemistry at semiconductor and oxidized metal electrodes*. 1st ed. Plenum press, 1980. 407 pp.
- [213] Norio Sato. *Electrochemistry at metal and semiconductor electrodes*. Elsevier, 1998.
- [214] Yong Xu and Martin A. A. Schoonen. "The absolute energy positions of conduction and valence bands of selected semiconducting minerals". In: *American Mineralogist* 85.3-4 (2000), pp. 543–556. [doi](#)

## REFERENCES

- [215] M. O. Krause and J. H. Oliver. “Natural widths of atomic K and L levels,  $K\alpha$  X-ray lines and several KLL Auger lines”. In: *Journal of Physical and Chemical Reference Data* 8.2 (1979), p. 329. [doi](#)
- [216] M. O. Krause. “Atomic radiative and radiationless yields for K and L shells”. In: *Journal of Physical and Chemical Reference Data* 8.2 (1979), pp. 307–327. [doi](#)
- [217] Tamás Lengyel, Allan M. Ure, and János Inczédy. *Compendium of analytical nomenclature: definitive rules 1997*. Ed. by Tamás Lengyel, Allan M. Ure, and János Inczédy. 3rd ed. Blackwell Science, 1998. 958 pp. [🔗](#)
- [218] H. G. J. Moseley. “XCIII. The high-frequency spectra of the elements”. In: *The London, Edinburgh, and Dublin Philosophical Magazine and Journal of Science* 26.156 (1913), pp. 1024–1034. [doi](#)
- [219] Russell G. Egddell and Elizabeth Bruton. “Henry Moseley, X-ray spectroscopy and the periodic table”. In: *Philosophical Transactions of the Royal Society A: Mathematical, Physical and Engineering Sciences* 378.2180 (2020), p. 20190302. [doi](#)
- [220] Hadley Alexander Wickham. *ggplot2: Elegant graphics for data analysis*. 2nd ed. Springer, 2016. [🔗](#)
- [221] Christophe Delerue and Michel Lannoo. *Nanostructures: theory and modeling*. Red. by Phaëdon Avouris et al. NanoScience and Technology. Berlin, Heidelberg: Springer Berlin Heidelberg, 2004. [doi](#)
- [222] H. Fröhlich. “Die spezifische wärme der elektronen kleiner metallteilchen bei tiefen temperaturen”. In: *Physica* 4.5 (1937), pp. 406–412. [doi](#)
- [223] Heiner Linke. *Quantum dots: seeds of nanoscience*. The Royal Swedish Academy of Sciences, 2023, p. 17. [🔗](#)
- [224] V. B. Sandomirskiĭ. “Dependence of the forbidden-band width of semiconducting films on their thickness and temperature”. In: *Soviet Journal of Experimental and Theoretical Physics* 16.6 (1963), p. 1630. [🔗](#)
- [225] L. E. Brus. “Electron–electron and electron-hole interactions in small semiconductor crystallites: The size dependence of the lowest excited electronic state”. In: *The Journal of Chemical Physics* 80.9 (1984), pp. 4403–4409. [doi](#)
- [226] Matt Law, Joshua Goldberger, and Peidong Yang. “Semiconductor nanowires and nanotubes”. In: *Annual Review of Materials Research* 34.1 (2004), pp. 83–122. [doi](#)
- [227] Juan Jimenez and Jens W. Tömm. *Spectroscopic analysis of optoelectronic semiconductors*. Vol. 202. Springer Series in Optical Sciences. Cham: Springer International Publishing, 2016. [doi](#)
- [228] Jaison Jeevanandam et al. “Review on nanoparticles and nanostructured materials: history, sources, toxicity and regulations”. In: *Beilstein Journal of Nanotechnology* 9 (2018), pp. 1050–1074. [doi](#)



- [229] Mohamed Ahmed Abdellah. “Ultrafast photoinduced processes in core and core-shell quantum dots for solar cell applications: Tiny crystals for big applications”. PhD thesis. Lund: Lund university, 2015.
- [230] T. Jesper Jacobsson and Tomas Edvinsson. “Absorption and fluorescence spectroscopy of growing ZnO quantum dots: size and band gap correlation and evidence of mobile trap states”. In: *Inorganic Chemistry* 50.19 (2011), pp. 9578–9586. [doi](#)
- [231] Yosuke Kayanuma. “Quantum-size effects of interacting electrons and holes in semiconductor microcrystals with spherical shape”. In: *Physical Review B* 38.14 (1988), pp. 9797–9805. [doi](#)
- [232] Sadao Adachi. *Optical properties of crystalline and amorphous semiconductors: materials and fundamental principles*. Boston, MA: Springer US, 1999. 271 pp. [doi](#)
- [233] María Quintana et al. “Comparison of dye-sensitized ZnO and TiO<sub>2</sub> solar cells: studies of charge transport and carrier lifetime”. In: *Journal of Physical Chemistry C* 111.2 (2007), pp. 1035–1041. [doi](#)
- [234] Ü. Özgür et al. “A comprehensive review of ZnO materials and devices”. In: *Journal of Applied Physics* 98.4 (2005), p. 041301. [doi](#)
- [235] Tahereh Jafari et al. “Photocatalytic water splitting—The untamed dream: a review of recent advances”. In: *Molecules* 21.7 (2016), p. 900. [doi](#)
- [236] Indrek Jõgi et al. “Phase formation behavior in ultrathin iron oxide”. In: *Langmuir* 31.45 (2015), pp. 12372–12381. [doi](#)
- [237] I. V. Chernyshova, M. F. Hochella Jr, and A. S. Madden. “Size-dependent structural transformations of hematite nanoparticles. 1. Phase transition”. In: *Physical Chemistry Chemical Physics* 9.14 (2007), p. 1736. [doi](#)
- [238] Jose L. Rendon and Carlos J. Serna. “IR spectra of powder hematite: effects of particle size and shape”. In: *Clay Minerals* 16.4 (1981), pp. 375–382. [doi](#)
- [239] Frank J. Owens and Joseph Orosz. “Effect of nanosizing on lattice and magnon modes of hematite”. In: *Solid State Communications* 138.2 (2006), pp. 95–98. [doi](#)
- [240] M. J. Massey et al. “Effects of pressure and isotopic substitution on the Raman spectrum of  $\alpha$ -Fe<sub>2</sub>O<sub>3</sub>: Identification of two-magnon scattering”. In: *Physical Review B* 41.11 (1990), pp. 7822–7827. [doi](#)
- [241] D. L. A. de Faria, S. Venâncio Silva, and M. T. de Oliveira. “Raman microspectroscopy of some iron oxides and oxyhydroxides”. In: *Journal of Raman Spectroscopy* 28.11 (1997), pp. 873–878. [doi](#)
- [242] Irina Chamritski and Gary Burns. “Infrared- and Raman-active phonons of magnetite, maghemite, and hematite: a computer simulation and spectroscopic study”. In: *The Journal of Physical Chemistry B* 109.11 (2005), pp. 4965–4968. [doi](#)

## REFERENCES

- [243] Ping Rong et al. "Photocatalytic degradation of methylene blue (MB) with Cu<sub>1</sub>-ZnO single atom catalysts on graphene-coated flexible substrates". In: *Journal of Materials Chemistry A* 10.11 (2022), pp. 6231–6241. [doi](#)
- [244] Surbhi Sharma, Dheeraj Kumar, and Neeraj Khare. "Hierarchical PANI/ZnO nanocomposite: synthesis and synergistic effect of shape-selective ZnO nanoflowers and polyaniline sensitization for efficient photocatalytic dye degradation and photoelectrochemical water splitting". In: *Nanotechnology* 31.46 (2020), p. 465402. [doi](#)
- [245] Sunandan Baruah et al. "Photoreactivity of ZnO nanoparticles in visible light: effect of surface states on electron transfer reaction". In: *Journal of Applied Physics* 105.7 (2009), p. 074308. [doi](#)
- [246] R. Saravanan et al. "ZnO/CdO composite nanorods for photocatalytic degradation of methylene blue under visible light". In: *Materials Chemistry and Physics* (2010), pp. 28–31. [doi](#)
- [247] T. Pauporte and J. Rathousky. "Electrodeposited mesoporous ZnO thin films as efficient photocatalysts for the degradation of dye pollutants". In: *Journal of Physical Chemistry C* 111.21 (2007), pp. 7639–7644. [doi](#)
- [248] K. Bergmann and C. T. O'Konski. "A spectroscopic study of methylene blue monomer, dimer, and complexes with montmorillonite". In: *Journal of Physical Chemistry* 67.10 (1963), pp. 2169–2177. [doi](#)
- [249] J. Cenens and R. A. Schoonheydt. "Visible spectroscopy of methylene blue on hectorite, Laponite B, and Barasym in aqueous suspension". In: *Clays and Clay Minerals* 36.3 (1988), pp. 214–224. [doi](#)
- [250] J. Ruprecht and H. Baumgärtel. "The influence of the electronic structure on the dimerization of phenthiazonium cations in aqueous solution". In: *Berichte der Bunsen-Gesellschaft für physikalische Chemie* 88.2 (1984), pp. 145–150. [doi](#)
- [251] Maxwell Schubert and Anne Levine. "A qualitative theory of metachromasy in solution". In: *Journal of the American Chemical Society* 77.16 (1955), pp. 4197–4201. [doi](#)
- [252] G S Singhal and Eugene Rabinowitch. "Changes in the absorption spectrum of methylene blue with pH". In: *The Journal of Physical Chemistry* 71.10 (1967), pp. 3347–3349. [doi](#)
- [253] Dominik Heger, Jaromír Jirkovský, and Petr Klán. "Aggregation of methylene blue in frozen aqueous solutions studied by absorption spectroscopy". In: *Journal of Physical Chemistry A* 109.30 (2005), pp. 6702–6709. [doi](#)
- [254] G. N. Lewis et al. "Dimeric and other forms of methylene blue: absorption and fluorescence of the pure monomer". In: *Journal of the American Chemical Society* 65.6 (1943), pp. 1150–1154. [doi](#)

- [255] Emory Braswell. "Evidence for trimerization in aqueous solutions of methylene blue". In: *Journal of Physical Chemistry* 72.7 (1968), pp. 2477–2483. [doi](#)
- [256] Sandro L. Fornili, Giuseppe Sgroi, and Vincenzo Izzo. "Solvent isotope effect in the monomer-dimer equilibrium of methylene blue". In: *Journal of the Chemical Society, Faraday Transactions 1: Physical Chemistry in Condensed Phases* 77.12 (1981), p. 3049. [doi](#)
- [257] Talat Mahmood et al. "Solvatochromic effect of methylene blue in different solvents with different polarity". In: *European Academic Research* 1.6 (2013), pp. 2286–4822.
- [258] M. J. Blandamer et al. "Solvation spectra. Part 17.—Water-induced dimerization of various dye and related paramagnetic ions studied by optical and electron spin resonance spectroscopy". In: *Trans. Faraday Soc.* 63.0 (1967), pp. 1850–1857. [doi](#)
- [259] W. West and Sandra Pearce. "The dimeric state of cyanine dyes". In: *The Journal of Physical Chemistry* 69.6 (1965), pp. 1894–1903. [doi](#)
- [260] Haiyuan Zhang et al. "Use of metal oxide nanoparticle band gap to develop a predictive paradigm for oxidative stress and acute pulmonary inflammation". In: *ACS Nano* 6.5 (2012), pp. 4349–4368. [doi](#)
- [261] Tingting Zhang et al. "Toxicity assessment of nano-ZnO exposure on the human intestinal microbiome, metabolic functions, and resistome using an in vitro colon simulator". In: *Environmental Science & Technology* 55.10 (2021), pp. 6884–6896. [doi](#)
- [262] Amir Moezzi, Andrew M. McDonagh, and Michael B. Cortie. "Zinc oxide particles: Synthesis, properties and applications". In: *Chemical Engineering Journal* 185–186 (2012), pp. 1–22. [doi](#)
- [263] Klaus Jacobs et al. "Melt growth of ZnO bulk crystals in Ir crucibles". In: *Solid State Sciences* 12.3 (2010), pp. 307–310. [doi](#)
- [264] Detlev Schulz et al. "Inductively heated Bridgman method for the growth of zinc oxide single crystals". In: *Journal of Crystal Growth* 310.7-9 (2008), pp. 1832–1835. [doi](#)
- [265] Sarmad Naim Katea et al. "Low cost, fast solution synthesis of 3D framework ZnO nanosponges". In: *Inorganic Chemistry* 56.24 (2017), pp. 15150–15158. [doi](#)
- [266] Jakob Thyr and Tomas Edvinsson. "Evading the illusions: identification of false peaks in micro-Raman spectroscopy and guidelines for scientific best practice". In: *Angewandte Chemie International Edition* 62.43 (2023), e202219047. [doi](#)
- [267] Jakob Thyr, Lars Österlund, and Tomas Edvinsson. "Polarized and non-polarized Raman spectroscopy of ZnO crystals: Method for determination of crystal growth and crystal plane orientation for nanomaterials". In: *Journal of Raman Spectroscopy* 52.8 (2021), pp. 1395–1405. [doi](#)

## REFERENCES

- [268] N. Ashkenov et al. “Infrared dielectric functions and phonon modes of high-quality ZnO films”. In: *Journal of Applied Physics* 93.1 (2003), p. 126. [doi](#)
- [269] Hsin Ming Cheng et al. “Size dependence of photoluminescence and resonant Raman scattering from ZnO quantum dots”. In: *Applied Physics Letters* 88.26 (2006), pp. 2004–2007. [doi](#)
- [270] Donghua Fan et al. “Size dependence of surface optical mode and electron–phonon coupling in ZnO nanocombs”. In: *Physica B: Condensed Matter* 407.17 (2012), pp. 3510–3514. [doi](#)
- [271] Ashish C. Gandhi et al. “New insights into the role of weak electron–phonon coupling in nanostructured ZnO thin films”. In: *Nanomaterials* 8.8 (2018), p. 632. [doi](#)
- [272] Animesh K. Ojha et al. “Influence of crystal size on the electron–phonon coupling in ZnO nanocrystals investigated by Raman spectroscopy”. In: *Vibrational Spectroscopy* 72 (2014), pp. 90–96. [doi](#)
- [273] S. S. Shinde et al. “Electron–phonon interaction and size effect study in catalyst based zinc oxide thin films”. In: *Journal of Molecular Structure* 984.1-3 (2010), pp. 186–193. [doi](#)
- [274] R. P. Wang, G. Xu, and P. Jin. “Size dependence of electron-phonon coupling in ZnO nanowires”. In: *Physical Review B* 69.11 (2004), p. 113303. [doi](#)
- [275] Wen-Feng Hsieh et al. “Size dependence of band gap variation and electron-phonon coupling in ZnO quantum dots”. In: *2005 Pacific Rim Conference on Lasers & Electro-Optics*. IEEE, 2005, pp. 466–468. [doi](#)
- [276] Joseph Wright. *siunitx – A comprehensive (SI) units package*. Version 3.2.0. 2023. [🔗](#)
- [277] Yihui Xie. *Dynamic documents with R and knitr*. 2nd ed. CRC Press, 2015. 294 pp.
- [278] Philip Kime, Moritz Wemheuer, and Philipp Lehman. *The biblatex package*. Version 3.19. CTAN, 2023. [🔗](#)
- [279] Philip Kime and François Charette. *biber: A backend bibliography processor for biblatex*. Version 2.18. 2022. [🔗](#)

# List of figures

1.1	The solar spectrum . . . . .	24
1.2	Chemical elements in photocatalytic compounds . . . . .	27
1.3	Band edges of semiconductor chalcogenides . . . . .	28
1.4	A nanoparticle is very small . . . . .	29
1.5	Word cloud of all titles in the bibliography . . . . .	33
2.1	Primary electrodeposition setup . . . . .	37
2.2	Secondary electrodeposition cell . . . . .	38
2.3	CdS CBD setup . . . . .	39
2.4	Sketch of the atomic-layer deposition process . . . . .	41
2.5	ZnO QD synthesis setup . . . . .	42
3.1	Rayleigh, Raman and IR scattering . . . . .	49
3.2	A Raman measurement . . . . .	51
3.3	Illustration of the air mass concept . . . . .	52
3.4	Representative emission spectra of common light sources . . . . .	53
3.5	Evolution of PC setups . . . . .	55
3.6	SEM scattering . . . . .	58
4.1	X-ray lines dataset examples . . . . .	70
6.1	Optical spectra of ZnO/CdS nanorod arrays . . . . .	79
6.2	Photoluminescence spectra of ZnO/CdS nanorod arrays . . . . .	79
6.3	Photodegradation of EBT with ZnO/CdS . . . . .	80
6.4	SEM micrographs ZnO/Fe <sub>2</sub> O <sub>3</sub> nanorods . . . . .	82
6.5	EDS map of zinc oxide/iron oxide nanorod array . . . . .	83
6.6	TEM line profile . . . . .	84
6.7	GI-XRD ZnO/Fe <sub>2</sub> O <sub>3</sub> . . . . .	84
6.8	XPS spectra of ZnO/Fe <sub>2</sub> O <sub>3</sub> nanorod arrays . . . . .	85
6.9	Raman spectra of ZnO/Fe <sub>2</sub> O <sub>3</sub> nanorod arrays . . . . .	86
6.10	Methylene blue in H <sub>2</sub> O and in H <sub>2</sub> O:EtOH solutions . . . . .	87
6.11	Photocatalytic degradation of MB with ZnO QDs . . . . .	89
6.12	Growing ZnO QDs tracked spectrophotometrically . . . . .	91
6.13	Fitted peak parameters of non-resonant Raman spectra . . . . .	94
6.14	Resonant Raman spectra . . . . .	95
6.15	Relative peak parameters vs. particle size for ZnO . . . . .	96
8.1	Det elektromagnetiska spektrat . . . . .	100
8.2	Nanopartiklars storlek . . . . .	101

# List of tables

- 1.1 Relative power density and relative flux of AM1.5G . . . . . 24
- 2.1 Molar masses, amounts and concentrations of the precursors. . 42
- 3.1 Constants related to solar spectral irradiance . . . . . 52
- 3.2 Structural properties of the phases . . . . . 61
- 4.1 Semiconductor properties: a subset of the band gaps dataset . . 69

# List of reactions

{1a}: Hydrogen evolution . . . . .	26
{1b}: Oxygen evolution . . . . .	26
{1}: Overall water splitting . . . . .	26
{2a}: Oxygen reduction in water . . . . .	37
{2b}: Zinc hydroxide to oxide . . . . .	37
{2}: Zinc oxide electrodeposition . . . . .	37
{3a}: Ammonium formation . . . . .	40
{3b}: Formation of cadmium complex . . . . .	40
{3c}: Formation of hydrogen sulfide . . . . .	40
{3d}: Release of sulfide ion . . . . .	40
{3e}: Cadmium sulfide ion by ion . . . . .	40
{3f}: Cadmium hydroxide precipitation . . . . .	40
{3g}: Cadmium hydroxide dissolution . . . . .	40
{3}: Deposition of cadmium sulfide . . . . .	40
{4a}: Photodegradation MB forming sulfoxide . . . . .	57
{4b}: Photodegradation MB forming sulfone . . . . .	57
{5}: Formation of leuco methylene blue . . . . .	57
{6a}: Photoexcited eh pair across interface . . . . .	81
{6b}: Formation of oxygen radical . . . . .	81
{6c}: Formation of hydroperoxyl radical . . . . .	81
{6d}: Formation of hydroxyl radical . . . . .	81
{6e}: Hydrogen peroxide decomposition to hydroxyl radicals . . . . .	81
{7a}: Photodegradation EBT via hydroxyl radical . . . . .	81
{7b}: Photodegradation EBT via hole . . . . .	81





# Colophon<sup>1</sup>

This thesis was typeset using the Lua $\text{\LaTeX}$  document processing system, together with substantial help from many  $\text{\LaTeX}$  extension packages, and some extra ad hoc  $\text{\LaTeX}$  programming effort.

It was written in the form of an Rnoweb document, which means it consists of regular text files that combine within them body text using  $\text{\LaTeX}$  syntax with program code in the R language.

In particular, I would like to highlight the following extension packages that were used to great benefit in the preparation of this thesis:


- `siunitx`, a  $\text{\LaTeX}$  package that typesets SI units consistently [276],
- `knitr` an R package that weaves together the  $\text{\LaTeX}$  and R code [277],
- `ggplot2` an R package for plotting using a *grammar of graphics* [220],
- `biblatex` powered by `biber` to manage the bibliography [278, 279].

The thesis source files are organised and tracked using `git`, a version control program, which was very helpful while drafting, rewriting, and editing, and later made it easy to share the source code.

To the extent possible, all ingestion, manipulation, and tabulating or plotting of data was done using code. In some cases the *result* of prior data analysis from papers or manuscripts was instead imported as R data objects.

This thesis was produced by the thesis production unit at the Uppsala University library, based on their official Xe $\text{\TeX}$  template, which this author adapted to work with Lua $\text{\LaTeX}$  (along with some other fixes).

Unless otherwise stated, all plots, illustrations, and photos are my own original work. Plots or illustrations that were created from code and where that code was not my own original work have attributions to the original authors in the source code of this thesis.

The full Rnw source code for this thesis will be made available as a git repository via <https://solarchemist.se/thesis> , and the Rnw and Lua $\text{\LaTeX}$  thesis templates will also be shared for those readers that may not want to inspect the full source code but just want to see how certain components were created or to base their own thesis off of it.

---

<sup>1</sup>A *colophon* is traditionally a brief statement at the end of a book containing information about the kind of paper, type, binding, and other technical details. I think of it as “production notes”.

# Acta Universitatis Upsaliensis

*Digital Comprehensive Summaries of Uppsala Dissertations from the Faculty of Science and Technology 2337*

Editor: The Dean of the Faculty of Science and Technology

A doctoral dissertation from the Faculty of Science and Technology, Uppsala University, is usually a summary of a number of papers. A few copies of the complete dissertation are kept at major Swedish research libraries, while the summary alone is distributed internationally through the series Digital Comprehensive Summaries of Uppsala Dissertations from the Faculty of Science and Technology. (Prior to January, 2005, the series was published under the title "Comprehensive Summaries of Uppsala Dissertations from the Faculty of Science and Technology".)

